TOPOLOGICAL SOLITONS AND THEIR DYNAMICS

A thesis submitted to the University of Kent
for the degree of Doctor of Philosophy
in the Faculty of Sciences

2017

Jennifer Ashcroft
School of Mathematics, Statistics and Actuarial Science

Contents

Abstract **14**

Declaration **15**

Acknowledgements **16**

1 Introduction **17**

1.1 Topology 18

1.2 Bogomolny bounds 19

1.3 Derrick's theorem 20

1.4 Kinks 22

1.5 Outline of the thesis 27

2 Kink collisions in the presence of false vacua **29**

2.1 The model 31

2.2 Scattering 36

2.2.1 AB scattering 36

2.2.2 BA scattering 41

2.2.3 $B\overline{A}$ scattering 42

2.2.4 $A\overline{B}$ scattering 47

2.3 Conclusions 51

3 Baby Skyrme models without a potential term **55**

3.1 The Baby Skyrme model 57

3.2 Baby Skyrme models without a potential 61

3.2.1 Derrick's scaling argument 61

3.2.2 Energy bounds 62
3.3 Numerical results 65
3.3.1 Axial baby Skyrme solutions 65
3.3.2 Baby Skyrme solutions in the $\alpha = 0.5$ model 68
3.3.3 Higher charge solutions 69
3.4 Conclusions 73

4 Multi-vortex scattering **76**
4.1 Vortices in the gauged Ginzburg-Landau model 78
4.2 Vortex dynamics 83
4.3 Multi-vortex scattering 87
4.4 Velocity of the escaping vortices 96
4.5 Conclusions 99

5 Vortices and impurities **102**
5.1 Vortices with magnetic impurities 103
5.1.1 Symmetric solutions 105
5.1.2 Impurity asymptotics 114
5.1.3 Static vortices and impurities 118
5.2 Vortex dynamics with magnetic impurities 122
5.3 Conclusions 129

6 Conclusions **132**

A Kinks: a point particle approximation **138**

B Baby Skyrmion linearisation **142**
B.1 Linearising as $r \to \infty$ 142
B.2 Linearising near $r = 0$ 144

Bibliography **145**

List of Tables

1.1 Some examples of topological solitons found in spatial dimensions $d \leq 3$, and the homotopy group, or set, that classifies them. 19

2.1 For each combination of kinks XY, we state whether the solitons repel or attract when they are well-separated and initially at rest. The first column specifies the type of kink on the left (i.e. X, the type of kink that is positioned at $x = -20$) and the first row gives the type of kink on the right (i.e. Y, the type of kink that is positioned at $x = +20$). The symbol "✗" is used whenever a particular combination of kinks is not allowed. 35

2.2 Summary of the different scattering behaviours observed for AB, BA, $B\overline{A}$ and $A\overline{B}$ kink collisions: repulsion, annhilation, formation of a true or false domain wall ("sticking") and reflecting off each other. Here, the symbol "✓" indicates that the respective behaviour is observed, whereas "✗" denotes that the respective behaviour is not exhibited. 51

3.1 Energy values obtained from full field simulations ($E^{(2D)}/4\pi B$) when compared to 1D gradient flow results ($E^{(1D)}/4\pi B$). The binding energy per soliton $\Delta E/4\pi B$ is calculated by (3.41) using the numerical 2D energy results. The two $B = 3$ configurations given are the axial solution (3.39) and the chain configuration of Fig. 3.8 which is denoted by 3*. 71

4.1 Outgoing velocity v_{out} of escaping pairs of vortices after the scattering of two $(N/2)$-vortex rings with initial velocity v_{in} and $N = 4, 6$. The given velocity is that of the first pair of vortices to escape during the simulation. . 97

5.1 Some different impurities and the corresponding values of q and m. 117

List of Figures

1.1 The ϕ^4 kink solution (1.16) and its energy density are plotted for parameter values $a = 0$, $m = 1$, and $\lambda = 1$. 24

1.2 Snapshots of the field configuration (in blue) and energy density (in red) during the scattering of (a)-(c): two kinks, and (d)-(f): a kink and an antikink, in the sine-Gordon model. 26

2.1 (a) Plot of the potential $V_\phi(\phi)$, (b) Plot of the potential $V_\psi(\psi)$. In both (a) and (b), local minima are indicated with red dots, and global minima with black dots. The parameters used are $a = 1$, $\alpha = 0.5$, $\beta = 1.0$, $\epsilon_\phi = 0.1$, $\epsilon_\psi = 0.5$. . . 32

2.2 (a), (b) Surface plots for two different viewing angles and (c) contour plot of the full scalar potential (2.2) for the parameter choice (2.6), but with γ set to 0.1 for illustrative purposes. Here, the true (T) vacua correspond to $\{\psi = -0.7593, \phi = 2k\}$, while false vacua (F) occur at $\{\psi = -0.7552, \phi = 2k + 1\}$. The white regions in the contour plot indicate the insurmountable energy barriers separating true and false vacua. The green and red arrows illustrate the kinks we call of type A and B, respectively. Note that the vacua at $\{\psi = 0.6396, \phi = 2k\}$ and $\{\psi = 0.6463,\ \phi = 2k + 1\}$ (see (b)) are all raised in energy and hence they are false vacua. We note that these plots appear courtesy of M. Haberichter and this figure is reproduced from Ref. [1]. . . 33

2.3 Examples of A and B kink configurations respectively. We plot the shepherd field ψ in red, and the sheep field ϕ in blue. Fig. (a) shows an A kink interpolating from $\phi = -1 \to \phi = 0$, and Fig. (b) a B kink interpolating from $\phi = 0 \to \phi = +1$. 34

2.4 For AB kink collisions, we display snapshots of the field configuration for two choices of initial velocity: (a)-(d) For $v = 0.7$, the A and B kinks form a false domain wall. (e)-(h) For $v = 0.8$, the A and B kinks escape to infinity after reflecting off each other with three bounces in the shepherd field. The corresponding contour plots are given in Fig. 2.7. 37

2.5 (a) The final velocity after an AB collision as a function of the initial velocity. When the outgoing velocity is plotted to be zero, a false domain wall is formed. (b) A closer view of the range $0.7 \leq v \leq 0.81$ which includes the window in which the kinks reflect off each other and escape to infinity. . . . 38

2.6 For an AB collision we display: (a) Number of bounces against initial velocity. Here, the bounce number measures the number of times the shepherd field ψ oscillates at the origin before the kinks separate. (b) Shepherd field $\psi(0, t)$ at the origin against time t for initial velocity $v = 0.75$. The three bounces in the shepherd field are clearly visible. For reasons of clarity, time is divided by 100. 39

2.7 For AB kink collisions with three different choices of initial velocity v, we display contour plots of the energy density of the sheep field ϕ. This illustrates the three different types of behaviour: (a) From rest, the AB pair repels and the trajectory is well described by a function of the form (2.7) (shown as a red dashed line). (b) For $v = 0.7$, the kinks capture each other and form a false domain wall. (c) For $v = 0.8$, the kinks reflect off each other, with three bounces in the shepherd field, and subsequently escape to infinity. For reasons of clarity, time is divided by 100. 40

2.8 For BA kink collisions, we display snapshots of the field configuration for the initial velocity $v = 0.8$. The A and B kinks form a "true" domain wall, that is the ϕ field interpolates between distinct true vacua. 41

2.9 For $B\overline{A}$ collisions, we display snapshots of the field configuration for the initial velocity $v = 0.8$. During their first collision, the kinks reflect off one another. Following this, they collide once more, forming an oscillon that will ultimately decay to the true vacuum. 42

2.10 The shepherd field $\psi(0,t)$ as a function of time t during $B\overline{A}$ scattering for four choices of initial velocity v. For reasons of clarity, time is divided by 100. (a) $v = 0$: from rest, the solitons move towards each other. An oscillon is formed after their first and only collision. This will ultimately decay to the true vacuum. (b) $v = 0.355$: the solitons reflect off each other once, then collide again and capture each other to form an oscillon. (c) $v = 0.606$: the solitons reflect off each other two times, before a final collision in which they form an oscillon. (d) $v = 0.808$: the solitons reflect off each other twice, with two bounces during the second collision. Finally they annihilate by forming an oscillon. 44

2.11 Number of bounces as a function of initial velocity v for $B\overline{A}$ interactions. Here the bounce number measures the number of times the shepherd field oscillates at the origin before the kinks separate. If no bounces are counted, then the solitons annihilate during their first collision, otherwise we colour in red the number of bounces during the first soliton collision, and in blue the number of bounces during the second collision of the solitons. 45

2.12 Contour plots of energy density for the sheep field ϕ during $B\overline{A}$ interactions with three different choices of initial velocity v. The locations of the soliton collisions are indicated on the plot, and for reasons of clarity, time is divided by 100. (a) $v = 0$: From rest the solitons attract and annihilate. Up to the first collision, the kink's trajectory is well described by a function of the form (2.7) (shown as a red dashed line). (b) $v = 0.355$: the solitons reflect off each other in their initial collision, then collide again and annihilate. (c) $v = 0.606$: the solitons reflect off each other twice, before a final collision in which they annihilate. 46

2.13 For $A\overline{B}$ collisions, we display snapshots of the field configuration for two choices of initial velocity v. (a)-(d) $v = 0.7$: the kinks collide and capture each other, forming an oscillon which ultimately decays to the false vacuum. (e)-(h) $v = 0.8$: the solitons reflect off each other. After three bounces in the shepherd field, they separate and escape to infinity. 48

2.14 (a) The final velocity v_{fin} after an $A\overline{B}$ collision as a function of the initial velocity v. When the final velocity v_{fin} is plotted to be zero, we observe the kinks capture each other, forming an oscillon that ultimately decays to the false vacuum. (b) A closer view of the range $[0.876, 0.88]$ to highlight two windows that are not visible in (a). 48

2.15 Number of bounces as a function of initial velocity v for $A\overline{B}$ collisions. Here the bounce number measures the number of times the shepherd field ψ oscillates at the origin before the solitons separate. If no bounces are counted, then the solitons do not separate, but annihilate to the false vacuum. 49

2.16 Contour plots of energy density for the sheep field ϕ during $A\overline{B}$ interactions with two different choices of initial velocity v. We indicate the locations of the collisions in the plots. For reasons of clarity, time is divided by 100. (a) $v = 0.7$: the solitons collide and form an oscillon which decays to the false vacuum. (b) $v = 0.8$: the solitons collide and reflect off each other. Once they have separated, the solitons travel apart and escape to infinity. 50

2.17 Example of an $A\bar{B}$ kink collision with coupling constants (2.8) chosen to bring our model closer to the sine-Gordon model. We display snapshots of the field configuration for the initial velocity $v = 0.8$: An oscillon in the shepherd field is formed preventing the sheep fields from annihilating or passing through each other. 53

3.1 Contour plots of energy density for solitons of topological charge $B = 1, 2, 3, 4$ in the baby Skyrme model (3.1) with (a) - (d): the old potential V_1, (e) - (h): the new potential V_2. 60

3.2 Energy as a function of model parameter α for axially symmetric configurations with topological charges $B = 1-3,\ 10$. (a) Total energy E. (b) Binding energy per soliton $\Delta E/4\pi B$. 66

3.3 $B = 1$ profile functions $f(r)$ for model parameter $0.5 < \alpha \leq 1$. 67

3.4 Energy density for charge one baby Skyrmions with model parameter $\alpha = 0.5$. (a) Surface plot of the energy density. (b) We compare slices through the energy density obtained when relaxing two different $B = 1$ initial conditions: a baby Skyrme configuration relaxed with $\alpha = 0.51$ (green line) and a rotationally symmetric configuration generated from an $\alpha = 0.5$ profile function. 69
3.5 Energy density for charge two baby Skyrmions with model parameter $\alpha = 0.5$. (a) Surface plot of the energy density. (b) We compare slices through the energy density obtained when relaxing two different $B = 2$ initial conditions: a baby Skyrme configuration relaxed with $\alpha = 0.51$ (green line) and a rotationally symmetric configuration generated from an $\alpha = 0.5$ profile function. 70
3.6 Total energy E for baby Skyrmions obtained with the axial ansatz (3.39) and for baby Skyrmions obtained with the 2D relaxation method. 72
3.7 Energy density contour plots for baby Skyrmions with model parameter $\alpha = 0.6,\ 0.7,\ 0.8,\ 0.9$ and charges $B = 1 - 3$. 73
3.8 Contour plots of the energy density for $B = 3$ chain configurations. The value of α for each configuration is indicated underneath its plot. 74

4.1 Profile functions for $\lambda = 1$ vortex solutions with (a) $N = 1$, (b) $N = 2$, and the associated (c) energy density $E(r)$, and (d) magnetic field $B(r)$. 81
4.2 Energy of vortex profile functions for different values of λ and N. 82
4.3 Contour plot of energy density for critically coupled vortex solutions with topological charge (a) $N = 1$, (b) $N = 2$. 82
4.4 Contour plot of the energy density of two 2-vortex rings boosted towards each other with initial velocity $v = 0.3$ at critical coupling. 85
4.5 Scattering of two vortices at critical coupling with initial velocity $v = 0.3$ and initial positions $(\pm 4, \pm b)$ for impact parameter $b = 0,\ 2,\ 4,\ 6,\ 8,\ 10$. . . 86
4.6 Snapshots of the energy density during the scattering of two 2-vortex rings at critical coupling with initial velocity $v = 0.3$. The rings collide, and one pair of vortices scatters at right angles to escape along the y-axis. The other vortex pair forms a bound state at the origin in which the vortices repeatedly scatter through each other at right angles. 88

4.7 Vortex positions during the scattering of two 2-vortex rings at critical coupling. We plot x- and y-coordinates of the vortex position against time for different initial velocity v. (a) x-coordinate with $v = 0.2$. (b) y-coordinate with $v = 0.2$. (c) x-coordinate with $v = 0.4$. (d) y-coordinate with $v = 0.4$. (e) x-coordinate with $v = 0.6$. (f) y-coordinate with $v = 0.6$. 89

4.8 Snapshots of the energy density during the scattering of two 2-vortex rings at critical coupling with initial velocity $v = 0.75$. The rings collide and one pair of vortices scatters at right angles. The two other vortices then scatter through each other and escape to infinity along the y-axis. 90

4.9 Vortex positions during the scattering of two 2-vortex rings at critical coupling. We plot x- and y-coordinates of the vortex position against time for different initial velocity v. (a) x-coordinate with $v = 0.64$. (b) y-coordinate with $v = 0.64$. (c) x-coordinate with $v = 0.65$. (d) y-coordinate with $v = 0.65$. (e) x-coordinate with $v = 0.75$. (f) y-coordinate with $v = 0.75$. . . 91

4.10 Number of collisions prior to the escape of the central two vortices during the scattering of two 2-vortex rings against initial velocity $v \in [0.6, 0.8]$. Where the vortices do not escape but instead form a bound state, we count zero collisions to make the distinction between windows of the different scattering behaviours clearer, though in fact they collide repeatedly and never escape. 92

4.11 Snapshots of the energy density during the scattering of two 3-vortex rings at critical coupling with initial velocity $v = 0.3$. The rings collide and one pair of vortices scatters at right angles and escapes along the y-axis. The remaining four vortices split into pairs and scatter at right angles. They emerge on the y-axis, where the outer two vortices separate to infinity and the inner pair form a bound state, repeatedly scattering through each other at right angles. 93

4.12 Snapshots of the energy density during the scattering of two 3-vortex rings at critical coupling with initial velocity $v = 0.7$. The rings collide and one pair of vortices scatters at right angles. The other four vortices then scatter through each other. Two of them escape to infinity along the y-axis and the other two escape along the x-axis. 94

4.13 Vortex positions during the scattering of two 3-vortex rings at critical coupling. We plot x- and y-coordinates of the vortex positions against time for different initial velocity v. (a) x-coordinate with $v = 0.3$. (b) y-coordinate with $v = 0.3$. (c) x-coordinate with $v = 0.6$. (d) y-coordinate with $v = 0.6$. (e) x-coordinate with $v = 0.71$. (f) y-coordinate with $v = 0.71$. 95

4.14 A comparison of our two energy approximations for (a) two 2-vortex rings, and (b) two 3-vortex rings, with the measured data from Table 4.1. Outgoing velocity v_{out} is plotted against incoming velocity v_{in} for the real data as black circles, for the classical approximation as red diamonds and for the relativistic approximation as blue squares. 98

5.1 Vacuum solutions obtained by solving equations (1.10) with $\lambda = 0.5$ (in blue), and $\lambda = 1.5$ (in red), in the presence of the impurities $\sigma(r) = 4e^{-r^2}$ (solid lines), $\sigma((r) = -4e^{-r^2}$ (dashed lines), and $\sigma(r) = -8e^{-2r^2}$ (dotted lines). In the subfigures we display (a) profile function $\phi(r)$, (b) profile function $a_\theta(r)$, (c) energy density $E(r)$, (d) magnetic field $B(r)$. 106

5.2 Vacuum solutions obtained by solving equations (1.10) with three different values of λ in the presence of the impurity $\sigma(r) = 4e^{-r^2}$. In each subfigure, we display (a) profile function $\phi(r)$, (b) profile function $a_\theta(r)$, (c) energy density $E(r)$, (d) magnetic field $B(r)$. 108

5.3 Vacuum profile functions $\phi(r)$, $a_\theta(r)$ for impurities $\sigma(r) = -4de^{-dr^2}$ and coupling constants (a) $\lambda = 0.5$, (b) $\lambda = 1.0$, (c) $\lambda = 1.5$. In each subfigure we plot an $N = 1$ vortex profile function for that coupling constant as a solid black line. Note that for a_θ the profile function is shifted down to enable comparison with the impurity vacuum solutions. 109

5.4 Energy E/π of profile function solutions obtained by solving equations (1.10). In each subfigure we display energy against c for impurities of the form $\sigma(r) = ce^{-r^2}$ with topological charge (a) $N = 0$, and (b) $N = 1$. 111

5.5 Energy difference $\left(E_{1,\sigma} - (E_{0,\sigma} + E_1)\right)/\pi$ as a function of c for impurities of the form $\sigma(r) = ce^{-r^2}$, and $\lambda = 0.5,\ 1.0,\ 1.5$. Where the energy difference is positive, the impurity will repel a vortex, and where it is negative the impurity and vortex will attract. 112

5.6 We plot the critical values of c at which the impurity changes from attracting to repelling a vortex against d for impurities of the form $\sigma(r) = ce^{-dr^2}$, and $\lambda = 0.5,\ 1.5$. The line $c = -4d$, where the impurities approach a delta function of strength $\alpha = 1$ as d increases, is shown as a dashed line for comparison. 114
5.7 The potential (1.25) for a vortex and impurity with $\lambda = 0.5,\ 1.0,\ 1.5$ and impurities (a) $\sigma(r) = 4e^{-r^2}$, (b) $\sigma(r) = -4e^{-r^2}$, and (c) $\sigma(r) = -16e^{-4r^2}$. . . 118
5.8 Plot of $|\phi(x, 0)|^2$ against x for one vortex at critical coupling placed at different positions, and two different impurities σ. 119
5.9 (a)-(c) Energy E/π as a function of the separation s between a single vortex and an impurity σ for $\lambda = 0.5$ (in blue) and $\lambda = 1.5$ (in red). (d)-(f) We zoom into the figures (a)-(c) for $s \geq 2$ and compare them with the corresponding interaction potential (1.25) shifted by the energy of a well-separated vortex and impurity (shown in black). 120
5.10 Diagram to illustrate the definition of the scattering angle Θ and impact parameter b in our simulations. 122
5.11 (a) Scattering angle Θ in radians against impact parameter b for the scattering of a single vortex at critical coupling with impurities $\sigma(r) = e^{-r^2}$ (in red), and $\sigma(r) = -e^{-r^2}$ (in blue). The initial vortex speed is $v = 0.3$. (b) We display the same data, but for $\sigma(r) = -e^{-r^2}$ we plot $-\Theta$ for easier comparison with the scattering angle for $\sigma(r) = e^{-r^2}$. 123
5.12 Vortex trajectories during the scattering of a single vortex at critical coupling with impurities (a) $\sigma(r) = e^{-r^2}$ and (b) $\sigma(r) = -e^{-r^2}$ for the impact parameter values $b = 0, 1, 2, 3, 4, 5, 6, 7$ and initial velocity $v = 0.3$. The location of the impurity is indicated with a black dot. 124
5.13 Snapshots of the energy density during the scattering of a single vortex at critical coupling with impurities (a)-(c): $\sigma(r) = e^{-r^2}$ and (d)-(f): $\sigma(r) = -e^{-r^2}$ for initial velocity $v = 0.3$. 125
5.14 Snapshots of the energy density during the scattering of a 2-vortex ring at critical coupling with impurities (a)-(c): $\sigma(r) = e^{-r^2}$ and (d)-(f): $\sigma(r) = -e^{-r^2}$ for initial velocity $v = 0.3$. 126

5.15 Scattering angle Θ in radians against impact parameter b for the scattering of two vortices at critical coupling in the presence of impurities $\sigma(r) = e^{-r^2}$ (in red) and $\sigma(r) = -e^{-r^2}$ (in blue). 127

5.16 Vortex trajectories during the scattering of two vortices at critical coupling in the presence of impurities (a) $\sigma(r) = e^{-r^2}$ and (b) $\sigma(r) = -e^{-r^2}$ for impact parameter values $b = 0, 1, 2, 3, 4$ and initial velocity $v = 0.3$. In (a), we also plot the trajectory for $b = 2.54$ (where the scattering angle changes sign) as a black dashed line. The location of the impurity is indicated with a black dot, and the vortices are initially located at $(\pm 4, \pm b)$. 127

5.17 Snapshots of the energy density during the scattering of two $N = 1$ vortices at critical coupling through impurities (a)-(c): $\sigma(r) = e^{-r^2}$ and (d)-(f): $\sigma(r) = -e^{-r^2}$ for initial velocity $v = 0.3$. 128

A.1 (a) The potential $V(r)$ used to mimic AB scattering. (b) Solutions $x_1(t)$ in red and $x_2(t)$ in blue for initial velocity $v_0 = 0$. (c) Solutions $x_1(t)$ and $x_2(t)$ for $v_0 = -1.5$. (d) Solutions $x_1(t)$ and $x_2(t)$ for $v_0 = -2$. 139

A.2 (a) The potential $V(r)$ used to mimic BA scattering. (b) Solutions $x_1(t)$ in red and $x_2(t)$ in blue for $v_0 = -1$. 139

A.3 (a) The potential $V(r)$ used to mimic $A\overline{B}$ scattering. (b) Solutions $x_1(t)$ in red and $x_2(t)$ in blue for $v_0 = 0$. (c) Solutions $x_1(t)$ and $x_2(t)$ for $v_0 = -1.5$. . 140

A.4 (a) The potential $V(r)$ used to mimic $B\overline{A}$ scattering. (b) Solutions $x_1(t)$ in red and $x_2(t)$ in blue for $v_0 = 0$. 141

B.1 Real solutions λ_+, λ_- of Eq. (B.2) as functions of α for $0 < \alpha < 1$ and $B = 1$. 143

Abstract

Topological solitons are particle-like solutions of nonlinear field equations with important applications in physics. This thesis presents four research projects concerning topological solitons and their dynamics. We investigate solitons in (1+1)- and (2+1)-dimensions, and develop numerical methods to obtain static solutions and simulate soliton scattering.

We first study kink collisions in a model with two scalar fields in the presence of false vacua. We find a variety of scattering outcomes depending on the initial velocity and vacuum structure. Kinks can either repel, form a true or false domain wall, annihilate, or collide and escape to infinity. These behaviours occur in alternating windows of initial velocity. When the kinks escape to infinity, there are a number of oscillations or "bounces" before the kinks escape, and this bounce number is conserved in each of the windows.

In the second project we design new baby Skyrme models that do not require a potential term to allow topological soliton solutions. We raise the Skyrme and sigma terms to fractional powers, which enables us to evade Derrick's theorem. We calculate topological energy bounds for our models and numerically obtain minimal energy solutions for solitons of charge 1, 2, and 3. For each charge, the minimal energy solution is a ring.

The last two projects concern vortices in the Ginzburg-Landau model. In the first of these, we numerically investigate the scattering of multi-vortex rings. When two 2-vortex rings collide, there are two distinct scattering outcomes. In both cases, one pair of vortices will scatter at right angles and escape along the y-axis. The remaining two vortices will either form a bound state or escape along an axis after colliding a number of times.

Finally, we study vortices scattering with magnetic impurities of the form $\sigma(r) = ce^{-dr^2}$. An impurity will attract or repel a vortex depending on the coupling constant λ and the parameters c and d. We scatter critically coupled vortices with two different impurities and explore the relationship between the scattering angle and impact parameter. We also find that a 2-vortex ring will break up in a head-on collision with an impurity.

Declaration

I declare that all of the work contained in this thesis is my own, except where explicitly stated otherwise.

Chapter 2 describes work published as [1], which was a collaboration with Minoru Eto, Mareike Haberichter, Muneto Nitta, and Manu Paranjape. The research work for this paper was carried out by Mareike Haberichter and myself, with the other authors providing advice. The idea for a point particle approximation was due to Minoru Eto. Mareike Haberichter carried out any static numerics needed to obtain initial conditions for our simulations, and I used her static solutions to construct boosted initial conditions, carried out the scattering simulations, and performed calculations for the point particle approximation. Mareike Haberichter and I wrote the paper together, with feedback from the other authors.

Chapter 3 discusses work published as [2] in collaboration with Mareike Haberichter and my supervisor Steffen Krusch. I carried out the numerical calculations and analytical work for this paper, and wrote it myself, with the co-authors providing advice on the project and feedback on the writing.

Acknowledgements

Firstly I would like to thank my supervisor Steffen Krusch for his advice and mentorship. Thank you for always making time for me, and for encouraging me to take part in competitions and grasp every opportunity that comes my way.

Thank you to Jing Ping Wang for being my second supervisor. I acknowledge the UK Engineering and Physical Sciences Research Council and the School of Mathematics, Statistics, and Actuarial Science at the University of Kent for a PhD studentship.

No SMSAS acknowledgements section can be complete without a huge thank you to Claire Carter. You do so much for every single one of us, and your support has made an incredible difference to my time here. Thank you!

Thank you to my office mates Ellen, Mingjie, Christoph and Mark for your kindness and friendship, and for making it a pleasure to come to work every day. Thank you to all of the members of Katherine's Crazy Quizzing Crew over the years, especially to our core members Acki, Katherine, Clelia, Christoph, Neil, Neal, John, Alfredo and Floris. Let me know if you ever decide on a permanent team name!

To my best friend Mareike, thank you for everything. For making me laugh with your crazy stories, for bringing a smile to my face with your postcards, for getting me involved in your elaborate Outreach schemes, and for emailing me promptly at 11pm each night to remind me that it is BED TIME. Without your curfew, I might have been too tired to ever write this thesis. Your friendship is one of the things I treasure most from my time at Kent, and I look forward to our adventures continuing for many morning coffees to come!!

Thank you to my godmother Lorraine who has been a constant source of encouragement throughout my life. Thank you to Lyndsey, Rachel, Dan and Pete, and to Frankie, Dylan, Darcey and Harper for keeping me entertained with your antics.

Finally, thank you to my parents for your love, patience and support. Your endless belief in me means more than you can ever know. I love you both.

Chapter 1

Introduction

Topological solitons are stable, finite energy solutions to nonlinear field equations that are found in a variety of physical systems [3]. They are minimal energy solutions in certain field theories, generally having a smooth energy density that is mostly localised in some finite region of space. In this way they behave like particles. Examples of solitons include vortices in superconductors [4], baby Skyrmions in condensed matter systems [5, 6], and Skyrmions in nuclear physics [7]. Often the soliton equations cannot be solved analytically and the use of numerical methods is required to obtain solutions.

The first soliton was discovered by John Scott Russell, a Scottish naval engineer, in 1834 on the Union Canal at Hermiston [8, 9]. He observed a boat being drawn along a narrow channel by a pair of horses. When the boat came to a sudden stop, a strange wave pushed forward, travelling ahead. This wave fascinated him, and he chased after it for one or two miles on horseback. The wave exhibited some unusual properties: it formed a localised, smooth mass of water and travelled along the channel without appearing to change shape or lose speed. He named it the "Wave of Translation", and conducted further experiments in his own back garden to better understand its properties. To modern scientists and mathematicians, this type of wave is known as a *solitary wave*, and its properties and applications are still being studied today.

This thesis discusses the results of four research projects and concentrates on three different types of soliton in (1+1)- and (2+1)-dimensions. Each chapter begins with an overview of the model considered and by motivating the project which it concerns. In this introductory chapter, we review some key concepts relating to the study of topological solitons. We conclude this chapter with an outline of the thesis.

1.1 Topology

Consider two manifolds X and Y without a boundary. If a based map $\Psi : X \to Y$ can be continuously deformed into another based map $\Phi : X \to Y$, then we say that Ψ is *homotopic* to Φ. This is an equivalence relation and so it has equivalence classes. We call them *homotopy classes*. Let X be the n-sphere S^n. Then we denote the set of homotopy classes by $\pi_n(Y)$. For $n \geq 1$ this forms a group, called the nth *homotopy group* of Y. If the manifold Y is also the n-sphere, then we have the result that $\pi_n(S^n) = \mathbb{Z}$ for $n \geq 1$. We can label such maps by an integer, which we call the *topological charge*. For topological solitons, this integer gives the net number of solitons in the field configuration.

If $\Psi : X \to Y$ is a differentiable map between two closed manifolds of the same dimension, then the topological charge is also the *topological degree* of the map. Suppose that X is connected, then the topological degree is given by

$$\deg \Psi = \int_X \Psi^*(\Omega), \tag{1.1}$$

where Ω is the normalised volume form on Y, and $\Psi^*(\Omega)$ denotes the pull-back of this volume form to X.

In a field theory, the *vacuum* is the constant field configuration which has the smallest energy of all field configurations. Topological solitons cannot be continuously deformed into the vacuum and so must belong to a different homotopy class than that of the vacuum. We note that the base point condition imposed previously is only important for having a homotopy group structure. It is not required if we only wish to know which maps can or can not be continuously deformed into each other, so long as the domain X is connected.

We are interested in topological solitons defined in flat space $\mathbb{R}^d$. First, we will consider solitons in a field theory where the target space is a linear space. We assume that the energy density approaches zero rapidly towards spatial infinity. The boundary conditions which arise from this consideration are essential for the topological structure of the solitons. Say the theory involves n scalar fields $\phi = (\phi_1, ..., \phi_n)$, and denote by $\mathcal{V}$ the vacuum manifold of the theory. The boundary condition to ensure zero energy density at spatial infinity is that ϕ takes vacuum values there. We denote by S^{d-1}_∞ the sphere at infinity in $\mathbb{R}^d$. For the topological classification, it is sufficient to consider the field as a map $\phi^\infty : S^{d-1}_\infty \to \mathcal{V}$. Then the fields are topologically classified by the homotopy class of ϕ^∞, which belongs to $\pi_{d-1}(\mathcal{V})$ [3]. Examples of such topological solitons are kinks, vortices, and monopoles.

For nonlinear fields $\phi : \mathbb{R}^d \to Y$, where Y is a closed manifold, the classification is a little different. We assume that the field has finite energy. Then $\phi^\infty : S^{d-1}_\infty \to Y$ should be a constant map. If there is a potential, then this constant should be a value that minimises the potential, otherwise the exact value is unimportant. This boundary condition allows a one-point compactification of space $\mathbb{R}^d \cup \{\infty\} \cong S^d$. The maps $\phi : S^d \to Y$ are topologically classified by elements of the homotopy group $\pi_d(Y)$. Examples of such topological solitons include nonlinear kinks, baby Skyrmions, and Skyrmions.

Table 1.1: Some examples of topological solitons found in spatial dimensions $d \leq 3$, and the homotopy group, or set, that classifies them.

Soliton	d	Homotopy group
Kink	1	$\pi_0(\mathcal{V}) \times \pi_0(\mathcal{V})$
Nonlinear kink	1	$\pi_1(Y)$
Vortex	2	$\pi_1(\mathcal{V})$
Baby Skyrmion	2	$\pi_2(Y)$
Monopole	3	$\pi_2(\mathcal{V})$
Skyrmion	3	$\pi_3(Y)$

In Table. 1.1 we give some examples of topological solitons arising in space dimensions one, two and three, and the homotopy group (or set in the case of kinks) used to classify them. Note that the topological structure of both types of kink will be discussed further in Section. 1.4. In this thesis, we will be concerned with kinks in Chapter 2, baby Skyrmions in Chapter 3, and vortices in Chapters 4 and 5.

1.2 Bogomolny bounds

Topological solitons are usually obtained by solving second order PDEs. In some special cases, these PDEs can be reduced to first order equations called *Bogomolny equations* [10]. The solutions of Bogomolny equations are static solitons and multi-solitons. Where it is possible to have a Bogomolny equation, there exists a lower bound on the energy in terms of the topological charge, and this bound is saturated for solutions of the Bogomolny equation. Bogomolny solutions minimise the energy and so they are stable. Furthermore, since all solutions of the Bogomolny equations for a given topological charge N have the same energy, N such solitons can be placed at any location without affecting the energy of the solution.

Bogomolny bounds for baby Skyrmions and vortices are discussed in Chapters 3, 4, and 5.

The solution space of the Bogomolny equation for a given topological charge N is a smooth manifold called the *N-soliton moduli space* $\mathcal{M}_N$. The *moduli* are the parameters of the solution, for example the soliton positions. At any given time, assume that the field configuration is a solution of the Bogomolny equation. The soliton dynamics can be approximated by the dynamics on a reduced Lagrangian consisting of the potential energy and the restriction of the kinetic energy to $\mathcal{M}_N$.

1.3 Derrick's theorem

In this thesis we are concerned with field theories in flat space. For such theories, there is a theorem due to Derrick [11] that can be used to rule out the existence of topological solitons. The idea of the theorem is that for a field configuration to be a stationary point of the energy, it should be stationary under any variation, and in particular it should be stationary under a spatial rescaling. Derrick noted that for many field theories the static energy functional does not have any stationary points under spatial rescaling except the vacuum. In such theories, there are no static solutions of the field equations with finite energy apart from the vacuum, and thus there are no topological solitons.

We illustrate the application of this theorem with an example. Consider the following energy functional for a theory with one scalar field ϕ in d dimensions

$$E = \int (\nabla\phi \cdot \nabla\phi + U(\phi))\ \mathrm{d}^d x = E_2 + E_0, \tag{1.2}$$

where we denote by E_2 and E_0 the components of the energy involving the derivatives of ϕ of order indicated by the subscript. Then if we apply the spatial rescaling $x \mapsto \mu x$ for $\mu > 0$, followed by a change of variables from x to μx, the energy as a function of μ is given by

$$e(\mu) = \int \left(\mu^2 \nabla\phi \cdot \nabla\phi + U(\phi)\right)\ \mu^{-d}\mathrm{d}^d x = \mu^{2-d}E_2 + \mu^{-d}E_0. \tag{1.3}$$

We can now apply Derrick's theorem to determine for which values of d this theory can have topological solitons. First take $d = 1$. Then (1.3) becomes

$$e(\mu) = \mu E_2 + \frac{1}{\mu}E_0. \tag{1.4}$$

This function has a stationary point at $\mu = \sqrt{E_0/E_2}$, and thus Derrick's theorem cannot rule out the existence of topological solitons in this theory in one dimension. However, if we

take $d > 1$, the function $e(\mu)$ is monotonically decreasing as μ increases and so there is no stationary point of $e(\mu)$ when $d > 1$. Therefore Derrick's theorem rules out the existence of topological solitons in this theory for $d > 1$, but finite energy topological solitons can exist in one dimension.

It is possible to evade Derrick's theorem for $d > 1$ if we make some changes to the energy (1.2). In two dimensions, one possibility is to remove the potential term E_0 entirely. Then $e(\mu) = E_2$ is independent of μ, and the theory is scale invariant. Solutions in this model are called *lumps*. It is also possible to allow finite energy solutions in higher dimensions if we include additional terms with higher powers of the derivatives of ϕ, or higher order derivatives of ϕ. For example, including an E_4 term in two or three dimensions leads to baby Skyrmions and Skyrmions respectively. The application of Derrick's theorem to these models is an important element of the project in Chapter 3.

Consider a general energy functional for a gauge theory with a scalar field given by

$$E = \int \left(|f|^2 + |D\phi|^2 + U(\phi)\right) \, \mathrm{d}^d x = E_4 + E_2 + E_0, \tag{1.5}$$

where f is the field strength and $D\phi$ is the covariant derivative. The gauge field $a(x)$ rescales as $a(x) \mapsto \mu a(\mu x)$ so that the covariant derivative will scale in the same way as the usual derivative. The field strength f includes derivatives of a, and it rescales as $f(x) \mapsto \mu^2 f(\mu x)$, providing the E_4 term in (1.5). Thus Derrick's theorem can be evaded in two and three spatial dimensions for such a theory. The corresponding topological solitons are gauged vortices in two dimensions and gauged monopoles in three dimensions. Gauged vortices are the subject of Chapters 4 and 5.

As a final comment on Derrick's theorem, we note that it can be used to find relations between the different components of the energy. Assume that we have a solution of the field equation for the theory. Then this should be the stationary point of $e(\mu)$ and so we should have $\frac{de}{d\mu}\Big|_{\mu=1} = 0$. This gives us a relation between the different terms of the energy. To illustrate this idea, we use our example theory (1.2) in one spatial dimension. Here we have

$$\frac{de}{d\mu} = E_2 - \frac{1}{\mu^2} E_0, \tag{1.6}$$

so for the derivative to vanish at $\mu = 1$, we must have $E_2 = E_0$. In other words, the contribution to the energy from the gradient term is equal to that from the potential term. This type of relation is called a *virial theorem*.

1.4 Kinks

In this section we will illustrate some of the key concepts related to topological solitons by using the simplest example of such a solution - the *kink*. Kinks are topological solitons that arise in theories of one spatial dimension. A Lagrangian admitting kink solutions is

$$L = \int_{-\infty}^{\infty} \left(\frac{1}{2} \partial_\mu \phi \partial^\mu \phi - U(\phi) \right) \, \mathrm{d}x, \tag{1.7}$$

where ϕ is a real scalar field and the potential $U(\phi)$ is a real function with $U(\phi) \geq 0$. The potential energy of this theory is essentially (1.2) with $d = 1$. Thus we have already seen that Derrick's theorem does not rule out the existence of topological solitons in this theory, and further that they satisfy a virial theorem stating that the contribution to the potential energy from the gradient term is equal to that from the potential term.

The Euler-Lagrange equation associated to (1.7) is

$$\partial_\mu \partial^\mu \phi + \frac{dU}{d\phi} = 0. \tag{1.8}$$

Kinks are finite energy solutions to the field equation that are topologically distinct from the vacuum. To have finite energy, a solution must approach the vacuum as $x \to \pm\infty$. For there to be topological solitons, there must be multiple vacua. It is clear that if a solution tends to the same vacuum value as $x \to \pm\infty$, then that solution can be continuously deformed to the constant vacuum solution. Kink solutions interpolate between distinct vacua and so cannot be continuously deformed to a vacuum solution. Note that $\pi_0(\mathcal{V})$ is the set of distinct connected components of $\mathcal{V}$ and for there to be multiple vacua this set must be non-trivial. The kinks are classified by elements of $\pi_0(\mathcal{V}) \times \pi_0(\mathcal{V})$, as we indicated in Table 1.1.

As a first choice of potential term we will consider the ϕ^4 model, which has the potential

$$U(\phi) = \lambda(m^2 - \phi^2)^2, \tag{1.9}$$

where λ and m are real constants. In this model, there are only two vacua: the constant fields $\phi = \pm m$. Static finite energy solutions are either the vacuum, or kinks interpolating between the two different vacua. The topological charge is given by the integral

$$N = \frac{1}{2m} \int_{-\infty}^{\infty} \phi' \, \mathrm{d}x, \tag{1.10}$$

though it can only take one of three values. If $N = 0$, then the solution can be continuously deformed to the constant vacuum solution. If $N = 1$, then the soliton is a kink interpolating

from $\phi = -m \to \phi = +m$, and if $N = -1$ then the solution is an antikink interpolating from $\phi = +m \to \phi = -m$. Note that the antikink can be obtained from the kink solution by taking $\phi \mapsto -\phi$ in the kink solution.

This is an example of a theory in which it is possible to obtain a Bogomolny bound on the energy of static solutions. We first complete the square inside the potential energy of (1.7) as

$$E = \int_{-\infty}^{\infty} \left(\left(\frac{1}{\sqrt{2}}\phi' \pm \sqrt{\lambda}(m^2 - \phi^2) \right)^2 \mp \sqrt{2\lambda}(m^2 - \phi^2)\phi' \right) \mathrm{d}x. \tag{1.11}$$

Using the inequality

$$\left(\frac{1}{\sqrt{2}}\phi' \pm \sqrt{\lambda}(m^2 - \phi^2) \right)^2 \geq 0, \tag{1.12}$$

we find that

$$E \geq \left| \int_{-\infty}^{\infty} \sqrt{2\lambda}(m^2 - \phi^2)\phi' \, \mathrm{d}x \right| = \left| \int_{\phi(-\infty)}^{\phi(\infty)} \sqrt{2\lambda}(m^2 - \phi^2) \, \mathrm{d}\phi \right|, \tag{1.13}$$

where in the last step we have changed variables from x to ϕ. When we evaluate this integral, we obtain the Bogomolny bound

$$E \geq \frac{4}{3} m^3 \sqrt{2\lambda} \, |N|. \tag{1.14}$$

This bound is saturated for solutions of the Bogomolny equations

$$\phi' = \mp \sqrt{2\lambda}(m^2 - \phi^2), \tag{1.15}$$

with the plus sign corresponding to the kink solution, and the minus sign to the antikink. Solving this equation for the kink solution, we find

$$\phi(x) = m \tanh\left(\sqrt{2\lambda} m (x - a) \right), \tag{1.16}$$

where a is a constant of integration. The kink solution (1.16) and its energy density are plotted in Fig. 1.1. The field ϕ interpolates between the two vacua of the theory, taking the value midway between them at $x = a$. This is also the point where its energy density is maximal and is interpreted as the position of the kink. The kink position a is the only free parameter in the solution (1.16). The one-soliton solution space of the Bogomolny equation is the moduli space $\mathcal{M}_1 = \mathbb{R}$.

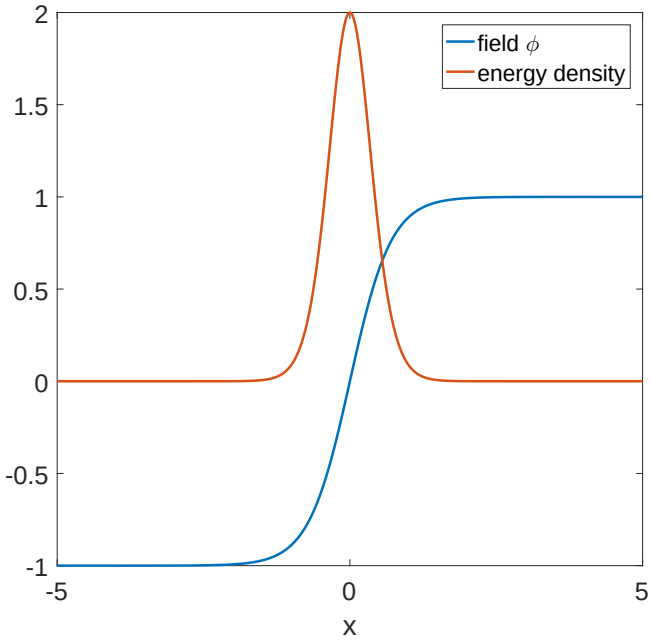

Figure 1.1: The ϕ^4 kink solution (1.16) and its energy density are plotted for parameter values $a = 0$, $m = 1$, and $\lambda = 1$.

We can easily obtain a moving kink solution from the static solution (1.16) by applying a Lorentz boost. This gives

$$\phi(t, x) = m \tanh\left(\sqrt{2\lambda} m\gamma(x - vt - a)\right), \tag{1.17}$$

where v is the velocity, and $\gamma = 1/(\sqrt{1 - v^2})$ is the Lorentz factor. Using an initial condition of a well-separated kink and antikink, we can study their dynamics by carrying out numerical simulations of the full field equation (1.8). Kink-antikink scattering in this model has an interesting dependence on the velocity. If kink and antikink move towards each other at low speed, then they will annihilate. However for higher velocities, "windows" of initial velocity are found in which different scattering behaviours are observed [12, 13].

We can apply the moduli space approximation to model the dynamics of kinks. Let us consider a single moving kink. Assume that the field ϕ at any given time is a solution of the Bogomolny equation and the kink position a varies slowly with time. Then we have the ansatz $\phi(x - a(t))$ for the moving kink. The potential energy is constant, so can be neglected, and the reduced kinetic energy is $T = \frac{1}{2}M\dot{a}^2$, where M is the kink mass. The equation of motion for this Lagrangian is $\ddot{a} = 0$, which has the solution $a(t) = vt + c$, where c and v are constants. This describes movement at a constant velocity v. We saw earlier that the exact

solution for a single moving kink is given by $\phi(\gamma(x - vt))$, so the moduli approximation is accurate for low velocities v, where γ is close to 1.

Another theory admitting kink solutions is the sine-Gordon model, with potential

$$U(\phi) = 1 - \cos\phi. \tag{1.18}$$

This model has infinitely many vacua, which are the constant fields $\phi = 2\pi n$ for $n \in \mathbb{Z}$. Kinks are solutions of the field equation interpolating between two distinct vacua. The topological charge is given by

$$N = \frac{1}{2\pi}\int_{-\infty}^{\infty} \phi' \mathrm{d}x, \tag{1.19}$$

which can take any integer value and counts the net number of kinks.

In the way that we have formulated the sine-Gordon model, the kinks are classified by elements of $\pi_0(\mathcal{V}) \times \pi_0(\mathcal{V})$. However it is also possible to consider them as nonlinear kinks if we set $\phi = (\sin\phi, \cos\phi)$ so that the target space is a circle S^1. Then ϕ must take the same value at $x = \pm\infty$, which is the vacuum value $\phi = (0, 1)$, and we can identify $x = +\infty$ with $x = -\infty$. There is a one-point compactification $\mathbb{R} \cup \{\infty\} \cong S^1$, and at a given time ϕ is a map $\phi : S^1 \to S^1$. It can be classified by elements of the homotopy group $\pi_1(S^1) = \mathbb{Z}$. In this formulation, the sine-Gordon model can be considered as a toy model for the Skyrme model [7] of nuclear physics, which has topological solitons called *Skyrmions*. This was originally proposed by Tony Skyrme due to the initial difficulty he found in studying the Skyrme model [14].

We can apply a similar completing the square argument to that used for the ϕ^4 kinks to obtain a Bogomolny bound in this case. We find

$$E \geq 8|N|, \tag{1.20}$$

which is saturated by solutions of the Bogomolny equations

$$\phi' = \pm 2\sin\frac{\phi}{2}. \tag{1.21}$$

Again, the plus sign corresponds to kink solutions, and the minus sign to antikinks. The corresponding kink solution can be written as

$$\phi(x) = 4\arctan e^{x-a}, \tag{1.22}$$

where a is an arbitrary integration constant. This solution describes a single kink with topological charge $N = 1$. It is positioned at $x = a$, which is the point where ϕ takes the value midway between the two vacua and its energy density is maximal. Since a single kink is the general solution of the Bogomolny equation, there are no multi-kink solutions to this equation. Indeed it can be shown that there is a repulsive force between two kinks, and there are no static multi-kink solutions in the sine-Gordon model [15].

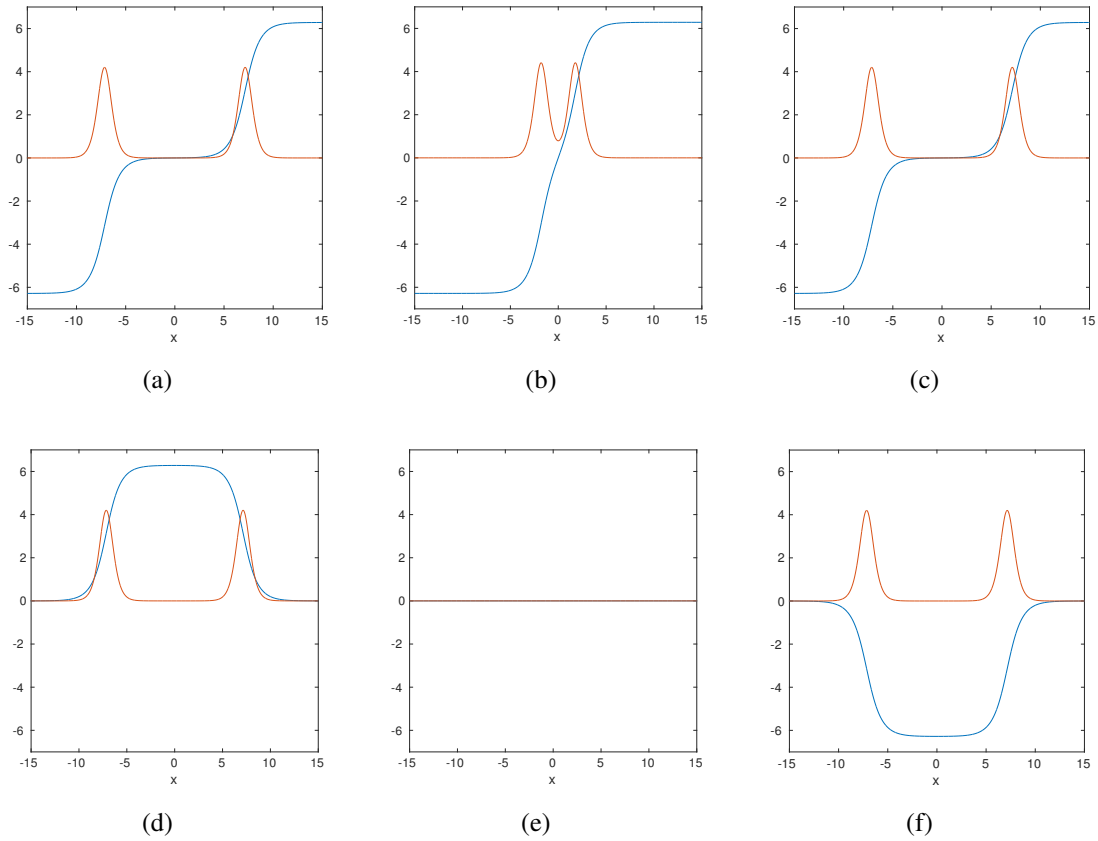

Figure 1.2: Snapshots of the field configuration (in blue) and energy density (in red) during the scattering of (a)-(c): two kinks, and (d)-(f): a kink and an antikink, in the sine-Gordon model.

However, there do exist exact formulae for time dependent multi-kink solutions in the sine-Gordon model. These can be used to study the scattering of kinks. As an example, in Fig. 1.2 we display snapshots of the field configuration and energy density during the scattering of (a)-(c): two kinks, (d)-(f): a kink and an antikink. In the two kink scattering, the kinks are initially well-separated but moving towards each other. They are closest at $t = 0$, after which they smoothly bounce off each other and separate to infinity. This has also been interpreted as the two kinks passing through each other. However, due to the repulsive

force between two kinks, at least at low velocities it makes more sense for them to bounce off each other. In the kink-antikink scattering the kink and antikink scatter elastically. There is a point, shown in Fig. 1.2(b), where the field configuration is a constant vacuum field and the kink and antikink appear to have annihilated, however they reappear afterwards with the same form and speed as they had initially.

1.5 Outline of the thesis

We will now give a brief overview of the thesis. The first project is a numerical study of kink scattering in a model of two scalar fields that has both true and false vacua. This is contained in Chapter 2, which presents work published as Ref. [1]. We explain the concept of true and false vacua in a field theory and introduce the particular field theory that we investigate along with its kink solutions. We study four different combinations of kinks in this model and devote a section to the results of numerical scattering simulations for each of them. We conclude with a discussion of the results observed in each section, and compare the observed scattering behaviours to those of kinks found in other models from the literature.

Chapter 3 concerns the design of new baby Skyrme models without a potential term. This work was published as Ref. [2]. We begin with a review of the baby Skyrme models that have been studied to date. We discuss the implications of Derrick's theorem for the structure of the baby Skyrme model and the Skyrme model. We also review the construction of a topological energy bound on solitons in the baby Skyrme model. Next, we present the construction of our new baby Skyrme models, discussing the application of Derrick's theorem, topological energy bounds, and one particular model in which there is a Bogomolny bound. Finally we present numerical simulations used to obtain static soliton solutions in this new family of baby Skyrme models, and we conclude with a discussion of the results.

In Chapter 4, we study the dynamics of gauged vortices in the Ginzburg-Landau theory of superconductivity. We first review the model and its static solutions before discussing how we generate initial conditions for scattering simulations, and implementing numerical methods for simulating vortex dynamics and tracking vortex positions. We investigate the scattering of multi-vortex solutions in this model, carrying out numerical simulations into the scattering of two 2-vortex rings and two 3-vortex rings for different initial velocities. There are two distinct scattering outcomes depending on the initial velocity. We conclude

by summarising our results and discussing further work to be carried out for this project.

Finally, in Chapter 5 we present the results of a project concerning the scattering of vortices in the presence of magnetic impurities. We first discuss the alterations made to the Ginzburg-Landau model to include such impurities, and obtain static vortex and impurity solutions for different values of the coupling constant λ. We discuss the different regimes in which an impurity will either attract or repel a vortex and how they depend upon the value of λ and the parameters of our impurity. We numerically simulate the scattering of one vortex and an impurity, and discuss the relationship between the impact parameter and scattering angle. We also consider the scattering of two vortices in the presence of an impurity and a head-on collision between a 2-vortex ring and an impurity. We end the chapter by reviewing our results and outlining future plans for this project.

We conclude the thesis with a discussion of the results from each chapter. We form connections between the different projects and consider opportunities for further work.

Chapter 2

Kink collisions in the presence of false vacua

In this chapter, we carry out numerical simulations to study kink scattering in a (1+1)-dimensional model of two scalar fields that was introduced in Ref. [16]. In a scalar field theory, a *vacuum* is any field configuration that is a local minimum of the potential energy density. We call the vacuum which has the lowest energy the *true vacuum*, and any local minima of higher energy are called *false vacua*. A key feature of the model in Ref. [16] is that it has a set of discrete vacua of different energies, meaning that it has both true and false vacua. We will find soliton solutions in this model that interpolate between true and false vacua and investigate their scattering phenomenology.

There has been considerable investigation into the dynamics of kinks in (1+1)-dimensional field theories, and a rich variety of scattering outcomes has been observed. For example, in ϕ^4 theories, the study of kink-antikink collisions reveals the existence of "windows" in which different scattering behaviours are seen [12, 13, 17, 18, 19]. This is also a feature of kink-antikink scattering in ϕ^6 models [20, 21]. By "window", we mean a range of values of the impact velocity for which the same scattering outcome is observed. One possible outcome is that the kink and antikink will collide and reflect a number of times, before separating to infinity. We will refer to the number of reflections in such a scattering behaviour as the *bounce number*, and use this to label the window. For instance, a velocity range in which kink and antikink collide, reflect, recede to a finite separation then collide and reflect once more before escaping to infinity is referred to as a *two-bounce window*. There are also windows of impact velocity for which the kink and antikink annihilate by forming a long-lived

oscillatory bound state, called an *oscillon*, which ultimately decays to the vacuum.

There has been a recent study into sine-Gordon kink collisions in the presence of true and false vacua [22]. Here the kinks connect true and false vacua in a system of three coupled long Josephson junctions. This is similar to our work, however the kinks in the article [22] are obtained as the solutions to a set of two coupled sine-Gordon equations, whilst our kinks are constructed differently.

Our model is taken from Ref. [16], in which the authors combine an asymmetric double-well potential with a perturbed sine-Gordon potential and a nonlinear interaction potential that is constructed so as to prevent the sine-Gordon solitons from passing through the double well solitons. We will discuss later in the chapter how this enables the existence of classically stable solitons which interpolate between distinct false vacua, though we note that other choices of potential term can be used to achieve the same effect [23]. In Ref. [16], the authors obtain *false domain wall* solutions in the model, that is domain walls which interpolate between distinct false vacua, with true vacuum in the core of the domain wall. They show that, whilst classically stable, the false domain walls are unstable to quantum tunnelling.

We construct kinks which interpolate between true and false vacua in this model, and numerically investigate their scattering phenomenology. The model in question may not be particularly realistic, but it does provide us with a simple (1+1)-dimensional setting in which to study the scattering of solitons in the presence of false vacua. We find a rich variety of scattering outcomes depending on the impact velocity and the location of the false vacuum: whether it lies outside or in between the two kinks.

In this chapter, we first review the model [16], including the locations of its true and false vacua, and present kink solutions which interpolate between true and false vacua. There are four combinations of these kinks that are interesting to use as initial conditions for the scattering simulations, and each provides a different set of outcomes due to the structure of true and false vacua. We present the results of numerical simulations into the scattering of kinks in each of these situations. Finally we discuss the results and how they relate to other kink scattering simulations in the literature.

2.1 The model

In this chapter, we consider a model first introduced in Ref. [16]. It has two real scalar fields, $\phi(t, x)$ and $\psi(t, x)$, and its Lagrangian is given by

$$L = \int \left(\frac{1}{2} \left(\partial_\mu \psi \partial^\mu \psi + \partial_\mu \phi \partial^\mu \phi \right) - V(\psi, \phi) \right) \, \mathrm{d}x \,, \tag{2.1}$$

where the potential $V(\psi, \phi)$ is given by

$$V(\psi, \phi) = V_\phi(\phi) + V_\psi(\psi) + V_{\psi\phi}(\psi, \phi) - V_0 \,, \tag{2.2}$$

with the individual potential terms

$$V_\phi(\phi) = \alpha \Big(\sin^2(\pi\phi) + \epsilon_\phi \sin^2(\pi\phi/2) \Big) \,, \tag{2.3}$$

$$V_\psi(\psi) = \beta(\psi + a)^2 \Big((\psi - a)^2 + \epsilon_\psi^2 \Big) \,, \tag{2.4}$$

and the interaction potential

$$V_{\psi\phi}(\psi, \phi) = \lambda \frac{(\psi - a)^2 \Big((\psi + a)^2 + \epsilon_\psi^2 \Big)}{\Big(V_\phi(\phi) - V_\phi(1/2) \Big)^2 + \gamma^2} \,. \tag{2.5}$$

The constant V_0 is chosen so that the global minimum of the potential is zero, and a, α, β, γ, λ, ϵ_ϕ, ϵ_ψ are real parameters with λ small compared to α, and γ small and positive. The model (2.1) admits solitons which we call *kinks*. The individual potential terms $V_\psi(\psi)$ and $V_\phi(\phi)$ are an asymmetric double well and a perturbed sine-Gordon potential respectively. Both potentials are known to have kink solutions. Indeed, if we set $\epsilon_\psi = \epsilon_\phi = 0$ and coupling constant $\lambda = 0$, then there are two different types of soliton: ψ is a kink connecting the two vacua of the asymmetric double well, and ϕ is a sine-Gordon kink. For nonzero values of ϵ_ψ and ϵ_ϕ, there is a set of discrete vacua of different energies. Fig. 2.1 displays the two individual potentials. The local minima are indicated with red dots, and the global minima with black dots. We see that $V_\phi(\phi)$ has local minima at $\phi = 2k + 1$ and global minima at $\phi = 2k$, for $k \in \mathbb{Z}$. The asymmetric double well $V_\psi(\psi)$ has a local minimum close to $\psi = +a$ and a global minimum at $\psi = -a$.

In Ref. [16], the authors studied domain walls interpolating between two distinct false vacua, with true vacuum in the core of the domain wall. They called such solutions *false domain walls* and chose the form of the interaction potential (2.5) so that the false domain walls are classically stable. The idea is that the solitons of the ϕ field, which we call the

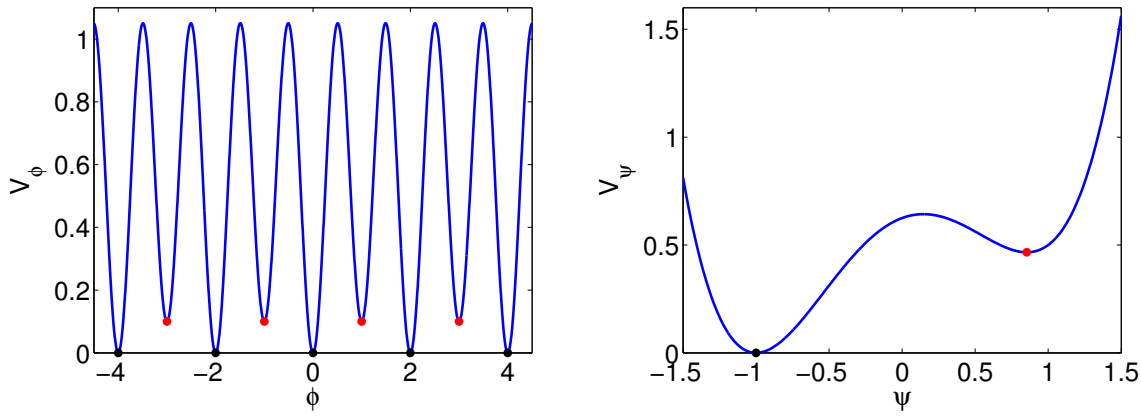

(a) $V_\phi(\phi)$ (b) $V_\psi(\psi)$

Figure 2.1: (a) Plot of the potential $V_\phi(\phi)$, (b) Plot of the potential $V_\psi(\psi)$. In both (a) and (b), local minima are indicated with red dots, and global minima with black dots. The parameters used are $a = 1$, $\alpha = 0.5$, $\beta = 1.0$, $\epsilon_\phi = 0.1$, $\epsilon_\psi = 0.5$.

sheep, are trapped within the solitons of the ψ field, which we call the *shepherd*. The sheep field ϕ is in its false vacuum outside of the domain wall, and its true vacuum within the core of the domain wall. Without the shepherd ψ, the sheep would spread out to infinity in order to extend the region of true vacuum. However, the shepherd field is in its true vacuum outside the domain wall, and its false vacuum within the domain wall. The sheep solitons are trapped within the shepherd soliton by the interaction potential, and the whole configuration is classically stable. This works because for nonzero λ, the interaction potential (2.5) provides an energy barrier which prevents ϕ solitons from passing through ψ solitons. The parameter γ in (2.5) is chosen to be small and nonzero, and so when the value of $V_\phi(\phi)$ is far from $V_\phi(1/2)$, the denominator of the interaction potential is very small. If ψ does not take a value close to one of its vacuum values here (so the numerator of the interaction potential is close to zero), then the energy contribution from the interaction potential becomes very large. For the ϕ solitons to pass through the ψ solitons, there would have to be a time at which $V_\phi(\phi) = V_\phi(1/2)$ and the ψ field is far from its vacuum values, which is energetically unfavourable. Thus the ϕ solitons are prevented from passing through the ψ solitons.

We will discuss the dynamics of kinks interpolating between true and false vacua in the model (2.1). Unless stated otherwise, we use the following set of parameters:

$$\alpha = 0.5\,, \quad \beta = 0.5\,, \quad \gamma = 0.01\,, \quad a = 1\,, \quad \epsilon_\psi = 1\,, \quad \epsilon_\phi = 0.01\,, \quad \lambda = 0.1\,. \tag{2.6}$$

Fig. 2.2 presents three different plots of the full potential (2.2) for the parameter choice outlined above, with the exception that we set $\gamma = 0.1$ for illustrative purposes. The first

plot, Fig. 2.2(a), is a surface plot of the potential. Fig. 2.2(b) presents the same surface plot from a different viewing angle, and with the locations of the true and false vacua indicated by T and F, respectively. The true vacua are found where ϕ takes even integer values, $\phi = 2k$ ($k \in \mathbb{Z}$), and ψ takes the vacuum value $\psi = -0.7593$. One set of false vacua is located at odd integers $\phi = 2k + 1$, and $\psi = -0.7552$. There are two further sets of false vacua occurring at $\{\phi = 2k,\ \psi = 0.6396\}$ and $\{\phi = 2k + 1,\ \psi = 0.6463\}$. Fig. 2.2(c) gives a contour plot of the same potential, again indicating true and false vacua by T and F, respectively. In this contour plot, the white regions indicate the energy barriers separating true and false vacua.

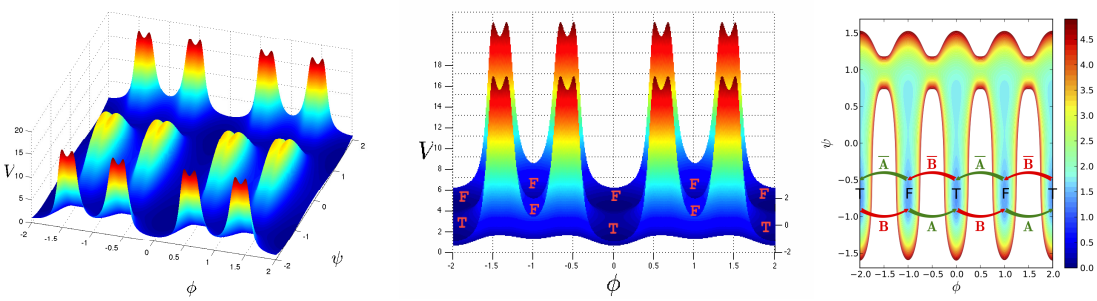

(a) (b) (c)

Figure 2.2: (a), (b) Surface plots for two different viewing angles and (c) contour plot of the full scalar potential (2.2) for the parameter choice (2.6), but with γ set to 0.1 for illustrative purposes. Here, the true (T) vacua correspond to $\{\psi = -0.7593, \phi = 2k\}$, while false vacua (F) occur at $\{\psi = -0.7552, \phi = 2k + 1\}$. The white regions in the contour plot indicate the insurmountable energy barriers separating true and false vacua. The green and red arrows illustrate the kinks we call of type A and B, respectively. Note that the vacua at $\{\psi = 0.6396, \phi = 2k\}$ and $\{\psi = 0.6463,\ \phi = 2k + 1\}$ (see (b)) are all raised in energy and hence they are false vacua. We note that these plots appear courtesy of M. Haberichter and this figure is reproduced from Ref. [1].

We will now explain some of the notation that we use to describe the kink solutions of the model (2.1). We will only be concerned with kinks interpolating between true vacua $\{\phi = 2k, \psi = -0.7593\}$ and the false vacua where $\{\phi = 2k + 1, \psi = -0.7552\}$, and so we will use the ϕ value to label the vacuum, e.g. we use $\phi = 0$ to denote the true vacuum at $(\phi = 0, \psi = -0.7593)$, and $\phi = 1$ to denote the false vacuum at $(\phi = 1, \psi = -0.7552)$. Kinks interpolating from a false vacuum to a true vacuum with ϕ increasing, e.g. $\phi = -1 \to \phi = 0$, as x goes from minus to plus infinity are called *A kinks*, and kinks interpolating from a true vacuum to a false vacuum with ϕ increasing, e.g. $\phi = 0 \to \phi = +1$, are called *B kinks*. Kinks interpolating in the same way with ϕ decreasing are called $\overline{A}$ and $\overline{B}$, respectively. An $\overline{A}$ *kink* interpolates from a false vacuum to a true vacuum with ϕ decreasing, e.g. $\phi = +1 \to \phi = 0$.

Similarly, a $\overline{B}$ *kink* interpolates from a true vacuum to a false vacuum with ϕ decreasing, e.g. $\phi = 0 \to \phi = -1$. Kinks of the type A and $\overline{A}$ connect false to true vacua, whilst B and $\overline{B}$ kinks connect true to false vacua. This is indicated in the contour plot of the potential (2.2) given in Fig. 2.2(c).

Fig. 2.3 presents examples of A and B kinks, with the ϕ field plotted in blue, and the ψ field in red. The particular kinks shown in the figure are (a) the A kink interpolating from $\phi = -1 \to \phi = 0$, and (b) the B kink interpolating from $\phi = 0 \to \phi = +1$. To obtain solutions such as those shown in Fig. 2.3, we first apply a numerical relaxation method to solve the field equations of the model (2.1), which are given explicitly in Ref. [16]. As initial conditions we use a straight line approximation for the sheep field ϕ, and an approximation in terms of hyperbolic tangents for the shepherd field ψ. Due to the imbalance in vacuum energies, the A or B kink will move away from the origin during the relaxation process in order to extend the region of true vacuum. We restore the kink's position to the centre by locating the maximum of the shepherd field ψ and shifting the kink so that this is located at the origin.

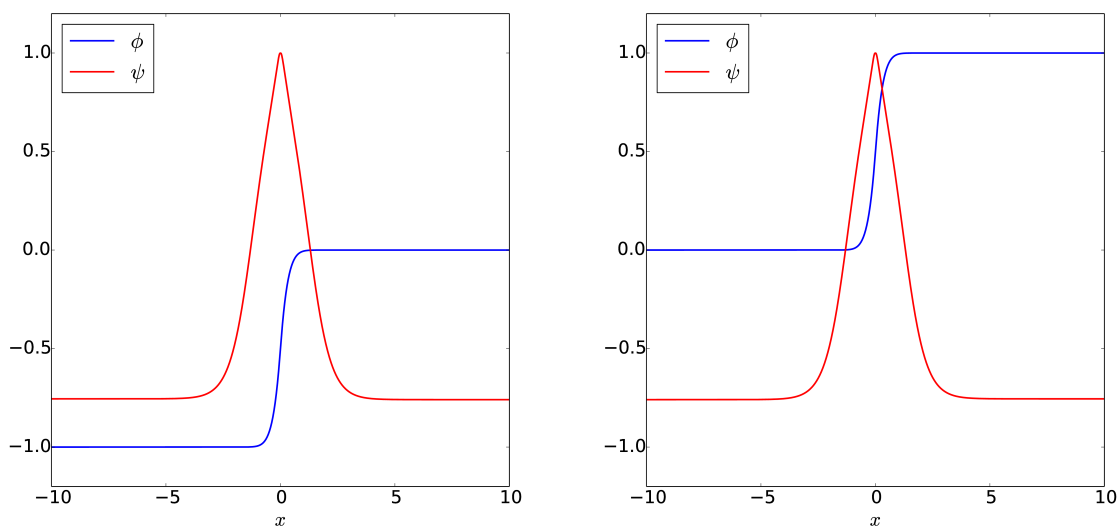

Figure 2.3: Examples of A and B kink configurations respectively. We plot the shepherd field ψ in red, and the sheep field ϕ in blue. Fig. (a) shows an A kink interpolating from $\phi = -1 \to \phi = 0$, and Fig. (b) a B kink interpolating from $\phi = 0 \to \phi = +1$.

Since these kinks have true vacuum on one side and false vacuum on the other, there are different asymptotic vacuum energy values as $x \to \pm\infty$. Therefore it is not immediately

obvious how to calculate the energy of an A or B kink. The approach that we take is the following. For A and B kinks on a spatial grid with 4001 points and spacing $\Delta x = 0.01$, we subtract the true vacuum energy on one side and the false vacuum energy on the other side using a Heaviside step function. This results in the kink mass 3.116. We checked that the kink mass is not significantly affected by different grid sizes and spacings.

We create the initial conditions for our scattering simulations by attaching a kink of one type which is positioned at $x = -20$, to another kink positioned at $x = +20$. We label these configurations by XY, where X denotes the type of kink located at $x = -20$, and Y denotes the type of kink located at $x = +20$. Due to the structure of true and false vacua, there are some combinations XY that do not work. For example, an A kink cannot be attached to an A or $\overline{A}$ kink to form an AA or $A\overline{A}$ configuration, because both interpolate from false to true vacua and so they cannot be smoothly joined together. Table 2.1 summarises the possible combinations of kinks, with the cross symbol "✗" used to indicate when a combination of kinks is not allowed. Where a combination of kinks is allowed, the table states whether that combination is "attractive" or "repulsive". The meaning of this terminology is explained below.

Table 2.1: For each combination of kinks XY, we state whether the solitons repel or attract when they are well-separated and initially at rest. The first column specifies the type of kink on the left (i.e. X, the type of kink that is positioned at $x = -20$) and the first row gives the type of kink on the right (i.e. Y, the type of kink that is positioned at $x = +20$). The symbol "✗" is used whenever a particular combination of kinks is not allowed.

Left \ Right	A	B	$\overline{B}$	$\overline{A}$
A	✗	repulsive	repulsive	✗
B	attractive	✗	✗	attractive
$\overline{B}$	attractive	✗	✗	attractive
$\overline{A}$	✗	repulsive	repulsive	✗

The structure of true and false vacua affects the behaviour of two well separated kinks that are initially at rest. For example, consider an AB configuration, which connects a kink interpolating from false to true vacuum, e.g. $\phi = -1 \to \phi = 0$, to one interpolating from true to false vacuum, e.g. $\phi = 0 \to \phi = +1$. These configurations have a region of true vacuum in between the two kinks, and false vacuum outside. When evolved from rest, the

kinks will accelerate away from one another as it is energetically favourable to extend the region of true vacuum in between them. In Table. 2.1 we describe such a configuration as "repulsive". As an example of the other possible behaviour, consider the BA configuration which connects a kink interpolating from true to false vacuum, e.g. $\phi = 0 \to \phi = +1$, to one interpolating from false to true vacuum, e.g. $\phi = +1 \to \phi = +2$. This has false vacuum in between the two kinks and true vacuum outside, and so the kinks will move towards each other. Such configurations are called "attractive" in Table. 2.1.

2.2 Scattering

In this section we present and discuss the results of our numerical simulations into the scattering behaviour of the solitons introduced above. We consider combinations of the type AB, BA, $B\overline{A}$, and $A\overline{B}$. Other combinations, e.g. $\overline{AB}$, are omitted from our discussions because their scattering behaviour is equivalent to those already in our list and so would not provide any new information. In Appendix A, we discuss a point-particle approximation which reproduces some of the scattering outcomes observed in this section.

Our numerical simulations use a finite difference leapfrog method. We choose the timestep $\Delta t = 0.002$ and the grid spacing $\Delta x = 0.01$ throughout, and typically work with grids of 20,001 or 40,001 points. Near the boundary, we apply a damping method in each timestep by updating $\dot{\phi}$ and $\dot{\psi}$ to approach zero exponentially. This reduces radiation and reflection from the boundary. Initial conditions are created by boosting two solitons towards each other by applying a Lorentz transformation.

2.2.1 AB scattering

We first discuss kink collisions with the AB structure in the model (2.1). This corresponds to the scattering of an A kink initially located at $x = -20$ with a B kink initially located at $x = +20$. In our numerical simulations, the A kink is one which interpolates from $\phi = -1 \to \phi = 0$, and the B kink from $\phi = 0 \to \phi = +1$. The kinks are initially well-separated and we boost them towards each other with an initial velocity v. See Fig. 2.4(a) for a snapshot of the field configuration before the collision takes place.

We carry out numerical simulations of the kink scattering for the range of initial velocities $0 \leq v \leq 0.9$. Fig. 2.5 shows final kink velocity as a function of initial kink velocity,

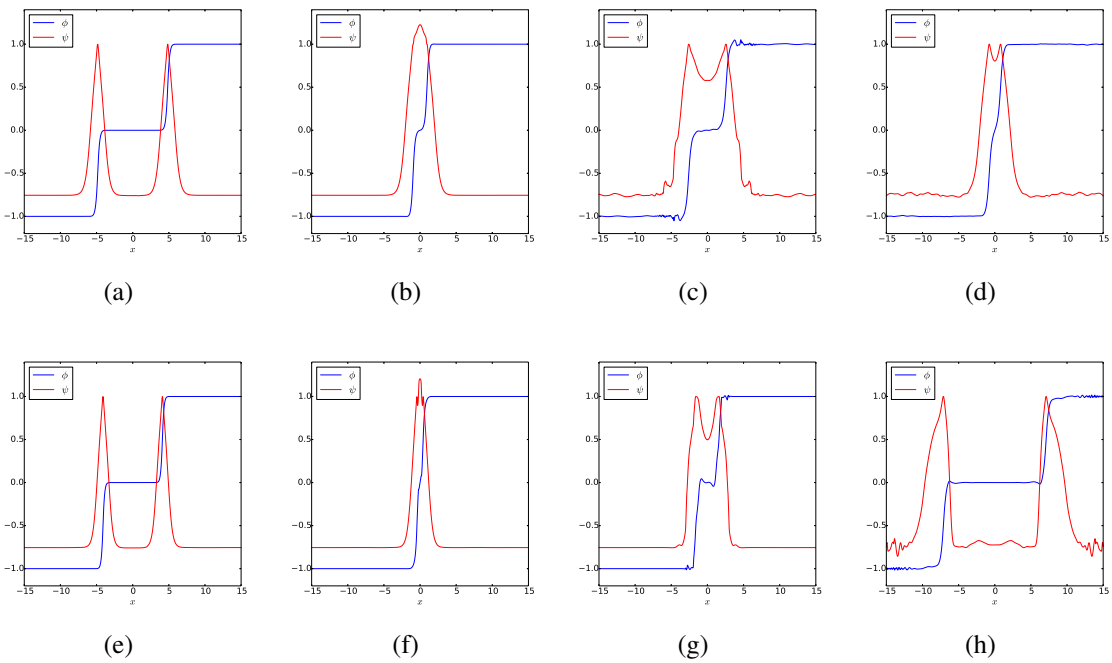

Figure 2.4: For AB kink collisions, we display snapshots of the field configuration for two choices of initial velocity: (a)-(d) For $v = 0.7$, the A and B kinks form a false domain wall. (e)-(h) For $v = 0.8$, the A and B kinks escape to infinity after reflecting off each other with three bounces in the shepherd field. The corresponding contour plots are given in Fig. 2.7.

where the final velocity is calculated as the kink in the positive x-axis passes the point $x = 50$. In our simulations, we observe three different scattering outcomes. Firstly, for initial velocities $v \leq 0.476$, we find that the A and B kinks cannot overcome the push outwards from the vacuum and will come to a halt then accelerate away from each other to extend the region of true vacuum. This can be seen in Fig. 2.5(a). For $0 \leq v \leq 0.476$, there is a velocity regime in which the final velocity is always significantly higher than the initial kink velocity. Within this regime, the final velocity increases with initial velocity.

For velocities greater than the critical velocity $v_{\text{crit}} = 0.476$, the kinks are able to overcome their repulsion and collide. The kink collision results in one of two behaviours: (i) formation of a false domain wall, or (ii) eventual escape to infinity. Case (i) is shown in the snapshots in Fig. 2.4(a)-(d), which are taken at four different times during the scattering process for $v = 0.7$. The AB pair becomes trapped and oscillates several times, radiating away its energy, before settling into a false domain wall [16]. In this final soliton state, the sheep field ϕ is in the false vacuum outside the domain wall, but passes through the true vacuum inside the domain wall. The sheep ϕ are trapped by the shepherd field ψ which is in its true vacuum outside the domain wall, but in its false vacuum inside the domain wall.

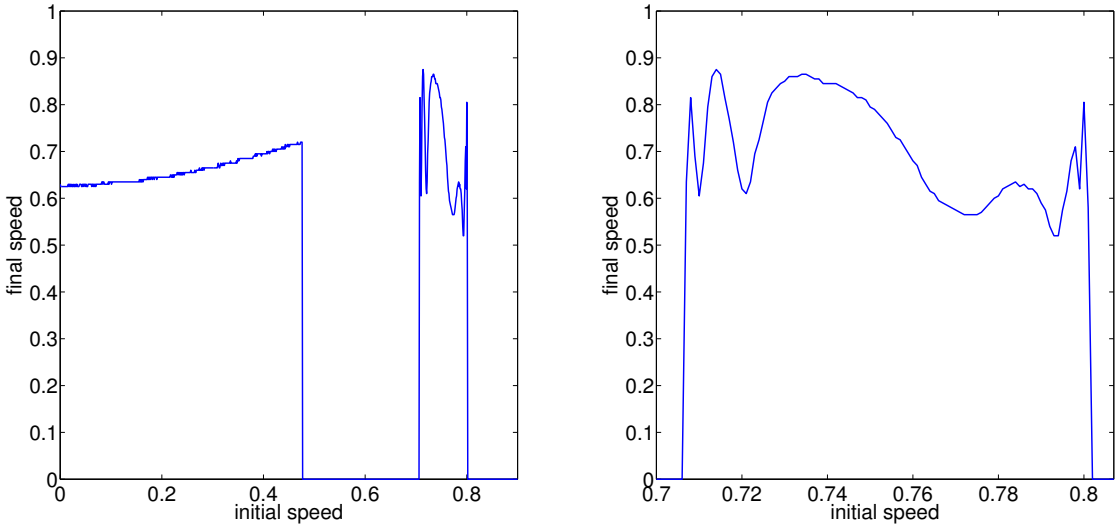

(a) (b)

Figure 2.5: (a) The final velocity after an AB collision as a function of the initial velocity. When the outgoing velocity is plotted to be zero, a false domain wall is formed. (b) A closer view of the range $0.7 \leq v \leq 0.81$ which includes the window in which the kinks reflect off each other and escape to infinity.

In Fig. 2.5(a), the outgoing velocity is plotted to be zero whenever a false domain wall is formed. Case (*ii*) is illustrated in the snapshots plotted in Fig. 2.4 (e)-(h), which are taken at four different times during an AB scattering process with initial velocity $v = 0.8$. In this case, the A and B kinks bounce off each other three times, separate, and then escape to infinity. The three-bounce collision is clearly visible when plotting the shepherd field $\psi(0,t)$ at the origin against time t. We give such a plot for initial velocity $v = 0.75$ in Fig. 2.6(b). What we call the three "bounces" are seen as three large spikes in the shepherd field after which the kinks reflect, recede and then return to bounce off each other again. After the third bounce, the kinks separate and escape to infinity.

Note that the two different behaviours observed for $v > v_{\text{crit}} = 0.476$ occur in alternating windows of initial velocity. This is clearly seen in Fig. 2.5(a), which plots the number of bounces in the shepherd field $\psi(0,t)$ as a function of initial velocity. Here, the number of bounces is the number of times that the shepherd field ψ oscillates at the origin before the kinks separate and escape to infinity (compare with Fig. 2.5(b)). We count three bounces for all AB collisions with initial velocities $v \in [0.707, 0.801]$. This window is measured with three significant figures of accuracy. For the velocity ranges $[0.477, 0.706]$ and $[0.802, 0.9]$ which surround this 3-bounce window, we count zero bounces as the kinks did not reflect

off each other and separate, but formed a false domain wall.

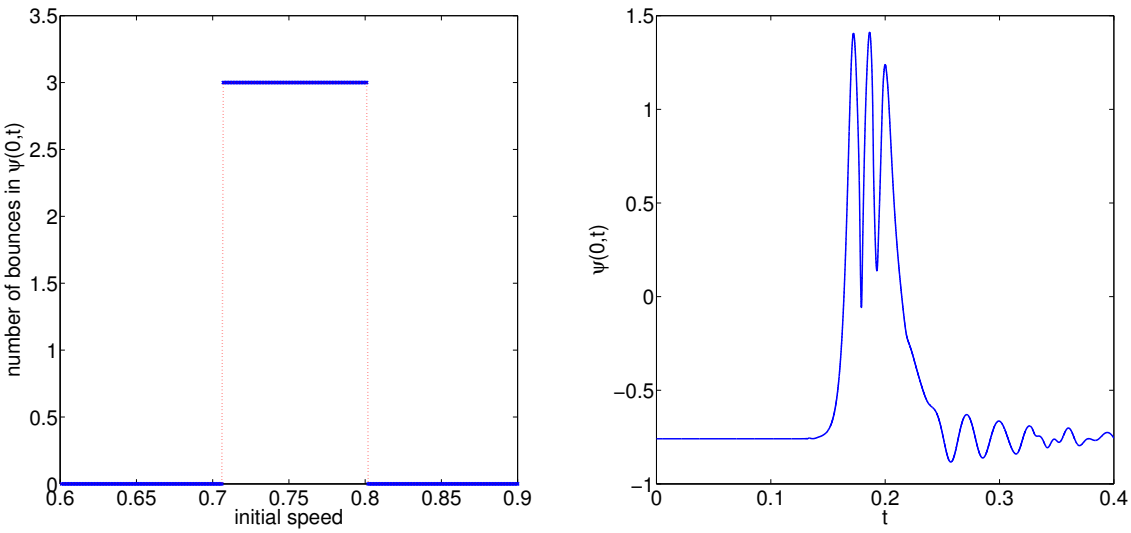

(a) (b)

Figure 2.6: For an AB collision we display: (a) Number of bounces against initial velocity. Here, the bounce number measures the number of times the shepherd field ψ oscillates at the origin before the kinks separate. (b) Shepherd field $\psi(0,t)$ at the origin against time t for initial velocity $v = 0.75$. The three bounces in the shepherd field are clearly visible. For reasons of clarity, time is divided by 100.

The positions of the solitons during the scattering process can be understood from the maxima of the energy density of the sheep field ϕ. In Fig. 2.7, we give contour plots of the energy density of the sheep field ϕ for three choices of initial velocity. Fig. 2.7(a) corresponds to initial velocity $v = 0$. This is an example of the repulsion behaviour seen for $v < v_{\text{crit}} = 0.476$, in which the kinks cannot overcome their repulsion and never collide. Here, the kink's trajectory can be well approximated by a function of the form

$$x(t) = \frac{c_1}{2}t^2 + c_2 t + c_3 + c_4 \exp(-c_5 t) \ , \tag{2.7}$$

where c_1, c_2, c_3, c_4, c_5 are taken to be fitting parameters. In Fig. 2.7(a) we compare the kink's trajectory as obtained from full field simulations with the function (2.7) with the best fit parameter values $c_1 = -0.001$, $c_2 = 1.346$, $c_3 = -122.821$, $c_4 = 142.979$ and $c_5 = 0.0096$. The fit is plotted in a dashed red line. For small t and short distances, the forces between kinks fall off exponentially fast with the potential being of the form $\exp(-mL)$, where m is a mass parameter and L denotes the separation between kinks. For larger t, and hence larger kink separations, the dominating force between kinks is due to the imbalance in vacuum energies. The A and B kinks are pushed apart from each other by the pressure of the true

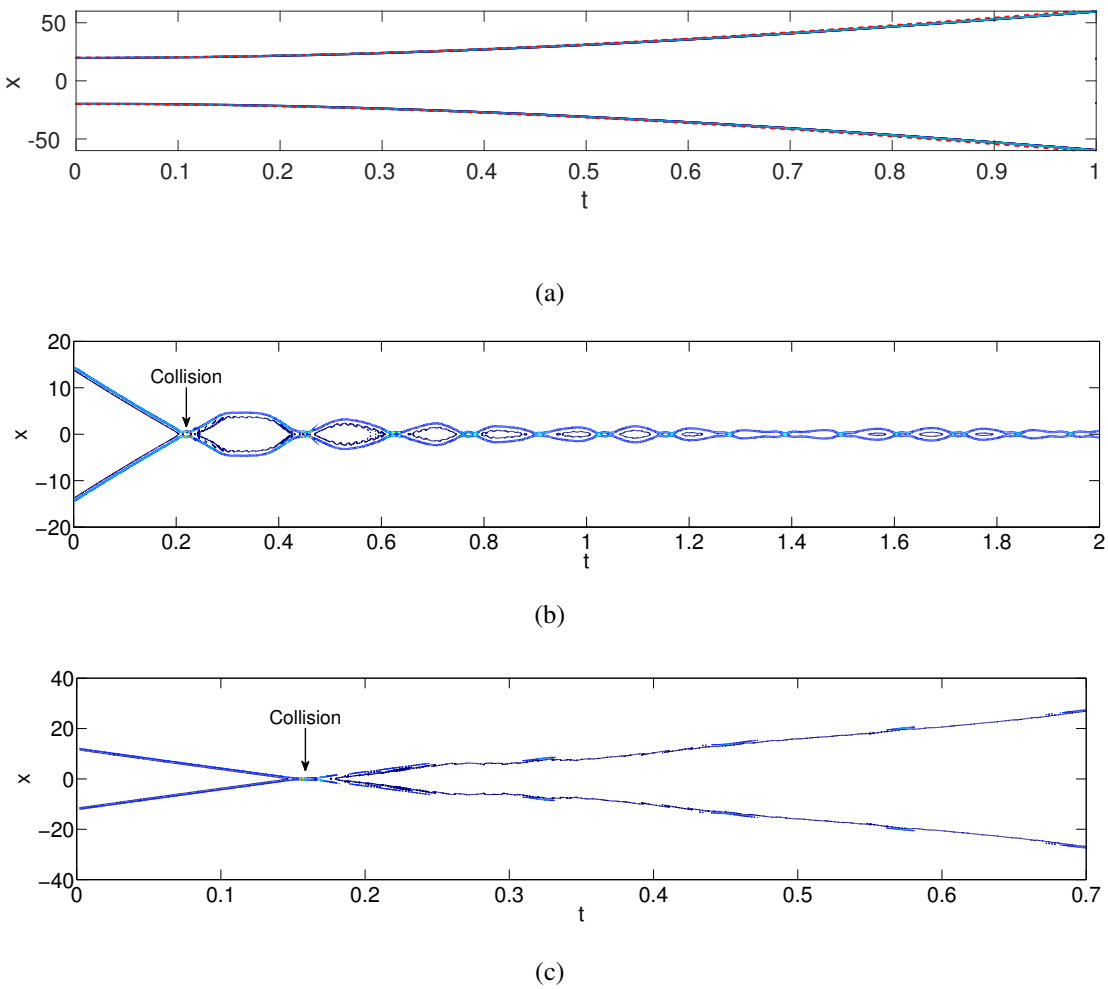

Figure 2.7: For AB kink collisions with three different choices of initial velocity v, we display contour plots of the energy density of the sheep field ϕ. This illustrates the three different types of behaviour: (a) From rest, the AB pair repels and the trajectory is well described by a function of the form (2.7) (shown as a red dashed line). (b) For $v = 0.7$, the kinks capture each other and form a false domain wall. (c) For $v = 0.8$, the kinks reflect off each other, with three bounces in the shepherd field, and subsequently escape to infinity. For reasons of clarity, time is divided by 100.

vacuum in between them. The force is constant which gives rise to orbits parabolic in time. For velocities $v \in [0.477, 0.706]$ and $v \in [0.802, 0.9]$, the A and B kinks capture each other and form a false domain wall. In the following, we call this type of behaviour "sticking". In Fig. 2.7(b), we display the contour plot of such a scattering process with the initial velocity $v = 0.7$. With this initial velocity, the kinks form an excited false domain wall at time $t = 20$ (for reasons of clarity, in the figures time is divided by 100). During each oscillation, energy is radiated away so that after a few oscillations the kink pair settles into a false domain wall. In Fig. 2.7(c), we show the contour plot for $v = 0.8$. Here, the kinks reflect off each other, with three bounces in the shepherd field, before separating to infinity. For this initial

velocity, the bounces occur at times $t = 14.6, 15.8, 17.1$. Recall that this type of scattering process is observed for all initial velocities $v \in [0.707, 0.801]$.

Note that the appearance of alternating windows of behaviour for kink-antikink collisions with the double well potential and in similar models, has been explained in the literature [13, 20] by an energy transfer between the translational and vibrational modes of the individual solitons. In the first collision energy is transferred to the vibrational modes, so that below a certain velocity the solitons do not have enough kinetic energy to escape their mutual attraction. Hence, they attract again and collide another time. After two or three or more kink-antikink collisions enough energy could be transferred back from the vibrational modes to the translational modes, allowing the solitons to escape back to infinity.

2.2.2 *BA* scattering

The next scattering process that we investigate is the collision of a B kink, initially located at $x = -20$, with an A kink which is initially located at $x = +20$. We call this a BA configuration, and a snapshot of such a configuration prior to the kink collision can be found in Fig. 2.8(a). For our simulations, we attach a B kink interpolating from $\phi = 0 \to \phi = +1$ to an A kink interpolating from $\phi = +1 \to \phi = +2$. Recall that a BA configuration has

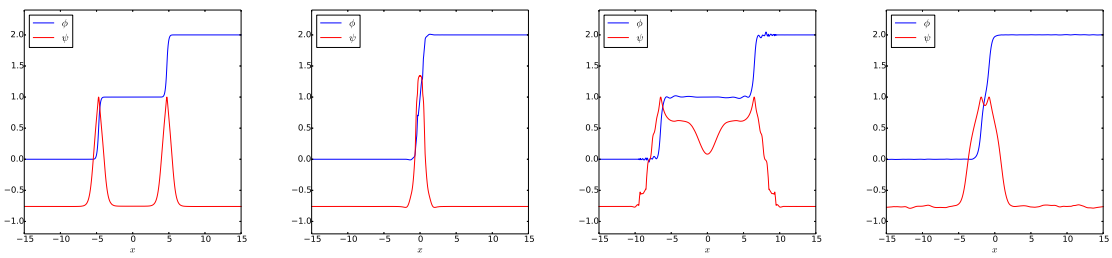

(a) (b) (c) (d)

Figure 2.8: For BA kink collisions, we display snapshots of the field configuration for the initial velocity $v = 0.8$. The A and B kinks form a "true" domain wall, that is the ϕ field interpolates between distinct true vacua.

true vacua outside the kinks, and false vacuum in between them. From rest the kinks will move towards each other to extend the regions of true vacuum. For all initial kink velocities $0 \leq v \leq 0.9$ we find the same scattering outcome, that is the creation of a true domain wall interpolating between the two distinct true vacua $\phi = 0$ and $\phi = +2$.

In Fig. 2.8(a)-(d), we give snapshots of the field configuration for initial velocity $v = 0.8$.

The kinks accelerate towards each other, converting false vacuum to true vacuum. They form an excited bound state which settles into a true domain wall after a few oscillations.

2.2.3 $B\overline{A}$ scattering

Recall that in our notation, $B\overline{A}$ is the combination of a kink interpolating from true vacuum to false vacuum with ϕ increasing, with one interpolating from false vacuum to true vacuum with ϕ decreasing. In our simulations, the B kink interpolates from $\phi = 0 \to \phi = +1$ and the $\overline{A}$ kink interpolates from $\phi = +1 \to \phi = 0$. The initial $B\overline{A}$ field configuration is displayed in Fig. 2.9(a).

$B\overline{A}$ configurations, like the BA configurations discussed in the previous section, have true vacua outside the kinks and false vacuum in between them. Thus the solitons will move towards one another from rest. Due to the attraction between the solitons and the kink-antikink structure of the configuration, the final result of any $B\overline{A}$ scattering is the formation of an oscillon that slowly radiates away energy and ultimately annihilates to the true vacuum. However, we observe that depending on the initial velocity v given to the solitons, this may be achieved in different ways. In some cases, the solitons first reflect off one another and travel apart, before they are drawn back together and collide again. This second collision may result in either the creation of an oscillon, or a repetition of the reflection behaviour. Note that kink-antikink collisions in which oscillons are formed have been observed before in a wide range of scalar field theories, see e.g. Refs. [18, 19, 24, 25]. During each oscillation, some of an oscillon's energy is radiated away, so it will eventually decay. However, the oscillon will persist for a very long time before this occurs.

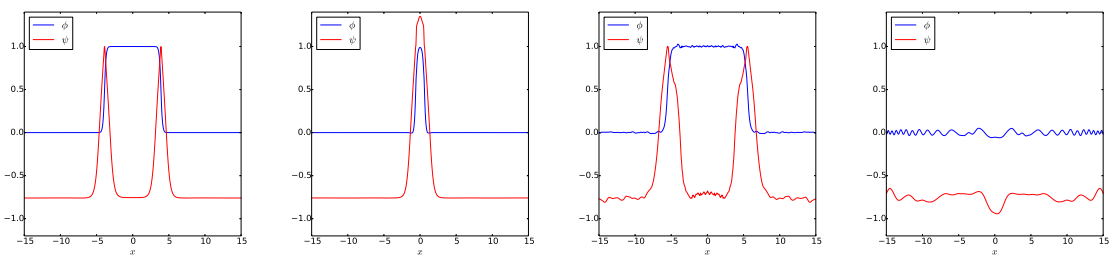

(a) (b) (c) (d)

Figure 2.9: For $B\overline{A}$ collisions, we display snapshots of the field configuration for the initial velocity $v = 0.8$. During their first collision, the kinks reflect off one another. Following this, they collide once more, forming an oscillon that will ultimately decay to the true vacuum.

Snapshots of the field configuration during a $B\overline{A}$ scattering with initial velocity $v = 0.8$ are shown in Fig. 2.9. The sheep field ϕ is displayed in blue, and the shepherd field ψ is shown in red. This choice of initial velocity results in two kink collisions. The first collision is seen in Fig. 2.9(b). During this collision there are three bounces in the shepherd field $\psi(0, t)$ before the solitons separate and travel apart. Fig. 2.9(c) shows the solitons excited by their collision and well separated by a region of false vacuum. Then the solitons come together and collide once more. An oscillon is formed which will ultimately annihilate to the true vacuum. This can be seen in Fig. 2.9(d).

The kink collisions and oscillon are most clearly seen in the shepherd field $\psi(0, t)$. In Fig. 2.10, we plot the shepherd field $\psi(0, t)$ at the origin as a function of t for three different choices of initial velocity where the solitons collide once, twice and three times respectively. The simplest case is illustrated in Fig. 2.10(a). Here the solitons capture each other during their first and only collision at $t = 65$ (for reasons of clarity, time is divided by 100 in the figure). They form an oscillon, which is seen for $t > 105$ as a long-lived series of oscillations in the ψ field. Fig. 2.10(b) corresponds to initial velocity $v = 0.355$. During the first collision of the solitons, near $t = 40$, there are four bounces in the shepherd field, before it returns to its false vacuum value. The solitons collide again at $t = 57$, and this results in the formation of an oscillon at around $t = 90$. In Fig. 2.10(c), the initial velocity is $v = 0.606$. The solitons first collide at $t = 22$, with the shepherd field bouncing three times before returning to its false vacuum value. The solitons remain separated for some time, before they collide again near $t = 165$. During this second collision there are four bounces in the shepherd field. The final soliton collision takes place at $t = 187$, and an oscillon is seen for $t > 220$. Another two reflection collision is seen in Fig. 2.10(d), corresponding to initial velocity $v = 0.808$. The solitons collide for the first time at $t = 13$, during which we count three bounces. Their second collision occurs at $t = 212$. This collision is unusual, as it features only two bounces and the false vacuum is attained in between bounces. Previously we had only observed windows of three bounces or more, and the false vacuum was only attained after the period of bouncing was complete.

Fig. 2.11 summarises the different scattering behaviours that we have observed for initial velocities in the range $0 \leq v \leq 0.9$. It displays the number of bounces in the shepherd field $\psi(0, t)$ at the origin as a function of initial velocity v. Where no bounces have been counted, the solitons immediately annihilated, without reflecting away from one another. In all other

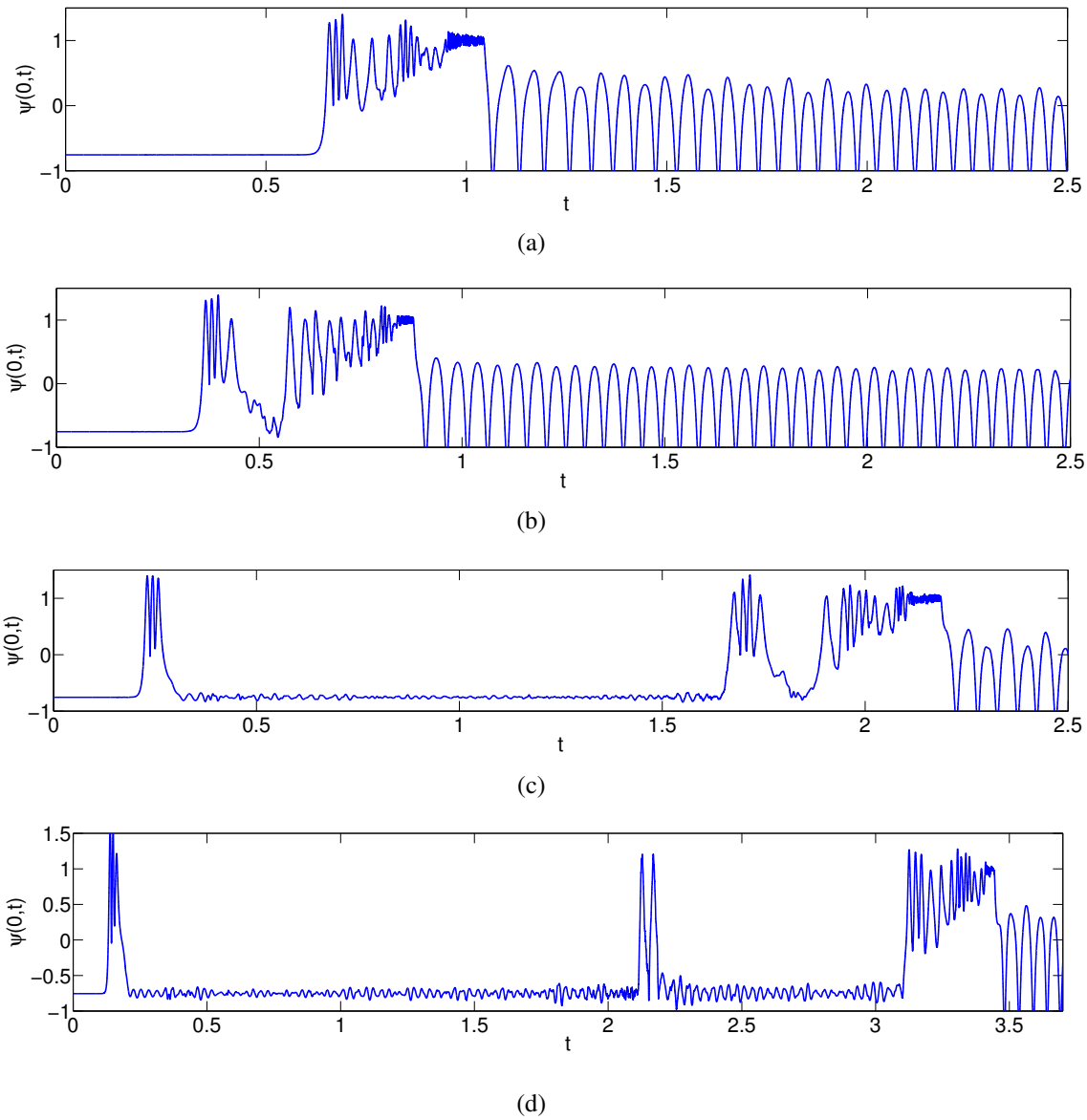

Figure 2.10: The shepherd field $\psi(0,t)$ as a function of time t during $B\overline{A}$ scattering for four choices of initial velocity v. For reasons of clarity, time is divided by 100. (a) $v = 0$: from rest, the solitons move towards each other. An oscillon is formed after their first and only collision. This will ultimately decay to the true vacuum. (b) $v = 0.355$: the solitons reflect off each other once, then collide again and capture each other to form an oscillon. (c) $v = 0.606$: the solitons reflect off each other two times, before a final collision in which they form an oscillon. (d) $v = 0.808$: the solitons reflect off each other twice, with two bounces during the second collision. Finally they annihilate by forming an oscillon.

cases, we find that the solitons reflect away from each other either one or two times before a final collision in which they annihilate by forming an oscillon which decays to the true vacuum. Prior to the formation of the oscillon, we consider the solitons to have reflected off one another if the shepherd field $\psi(0,t)$ takes its false vacuum value after a period of oscillations. We count the number of bounces during the reflections in the same way as we

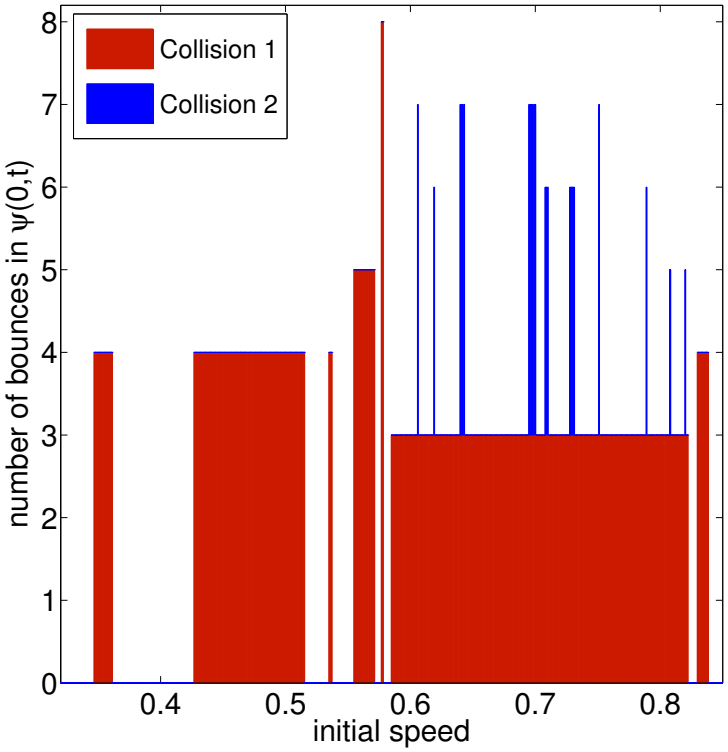

Figure 2.11: Number of bounces as a function of initial velocity v for $B\overline{A}$ interactions. Here the bounce number measures the number of times the shepherd field oscillates at the origin before the kinks separate. If no bounces are counted, then the solitons annihilate during their first collision, otherwise we colour in red the number of bounces during the first soliton collision, and in blue the number of bounces during the second collision of the solitons.

did for those AB collisions in which bouncing occurred. The number of bounces during the first reflection is shown in red, and if there was a second reflection, then the number of bounces during the second reflection is shown in blue. For the first reflection, we find windows of three, four, five or eight bounces. Of these windows, we only observe a second reflection for particular initial velocities within the three bounce window $v \in [0.585, 0.822]$. During the second collision, there are two unusual two bounce reflections for $v = 0.808$ and $v = 0.820$. The windows for the other values exhibit the more familiar three or four bounce signatures. There is a fractal structure in which windows of the reflection behaviour are separated by regions in which the solitons annihilate. Note that our initial velocity windows are only accurate to three significant figures and we expect that were we to investigate with greater resolution other windows with two or more reflections could be found.

In Fig. 2.12 we display contour plots of the sheep energy density for three choices of

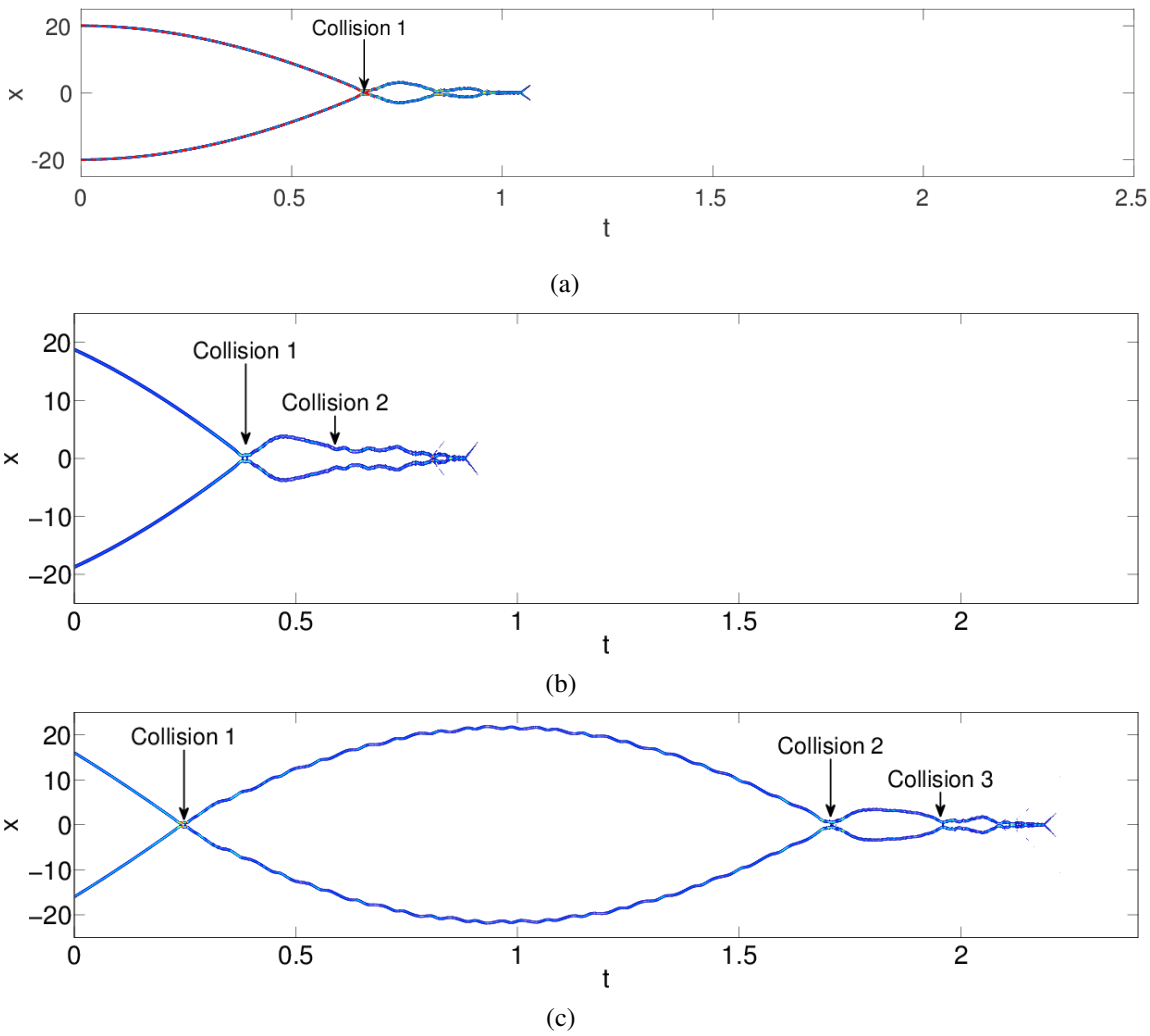

Figure 2.12: Contour plots of energy density for the sheep field ϕ during $B\overline{A}$ interactions with three different choices of initial velocity v. The locations of the soliton collisions are indicated on the plot, and for reasons of clarity, time is divided by 100. (a) $v = 0$: From rest the solitons attract and annihilate. Up to the first collision, the kink's trajectory is well described by a function of the form (2.7) (shown as a red dashed line). (b) $v = 0.355$: the solitons reflect off each other in their initial collision, then collide again and annihilate. (c) $v = 0.606$: the solitons reflect off each other twice, before a final collision in which they annihilate.

initial velocity: (a) $v = 0$, (b) $v = 0.355$, and (c) $v = 0.606$, with the locations of the soliton collisions indicated in the figures. In Fig. 2.12(a), we see the solitons move towards one another from rest and collide once, resulting in the formation of an oscillon which ultimately decays to the true vacuum. The oscillon is more clearly seen in Fig. 2.10(a), but the contour plot allows us to track the positions of the solitons away from the origin throughout the process. Up to the first collision, the parabolic kink trajectory in Fig. 2.12(a) is well described by Eq. (2.7) with the best fit parameter values $c_1 = -0.008$, $c_2 = -0.017$,

$c_3 = 20.106$ (and c_4 and c_5 set to zero).

Fig. 2.12(b) shows an interaction in which there are two collisions. During the first collision, the solitons reflect off each other. However, they do not travel far before they return for a second collision, which creates an oscillon. The first collision takes place near $t = 40$, and the second is at $t = 57$ (for clarity, time is divided by 100). This can be compared with Fig. 2.10(b), which uses the same initial velocity. Finally, Fig. 2.12(c) presents an interaction in which the solitons collide and reflect off one another twice before a final collision in which they form an oscillon that decays to the true vacuum. After the first collision the solitons travel quite far apart before they return for a second collision. The final collision takes place near $t = 180$, ultimately resulting in the annihilation of the solitons. This figure can be compared with Fig. 2.10(c), which uses the same choice of initial velocity, to see how the locations of the collisions correspond to the bounces in the shepherd field.

2.2.4 $A\overline{B}$ scattering

Finally we consider scattering processes of $A\overline{B}$ configurations, where we attach a kink interpolating from false vacuum to true vacuum with ϕ increasing to one interpolating from true vacuum to false vacuum with ϕ decreasing. In our simulations, we attach an A kink interpolating from $\phi = -1 \to \phi = 0$ to a $\overline{B}$ kink which interpolates from $\phi = 0 \to \phi = -1$. The initial configuration prior to any kink collisions is shown in Fig. 2.13(a).

Recall that $A\overline{B}$ configurations, like AB configurations, have the region of true vacuum in between the kinks, with false vacuum outside them. Therefore the kinks will move apart when evolved from rest. To overcome this effect and create soliton collisions, we boost the kinks towards each other with an initial velocity v. We carry out simulations over the range of initial velocities $0 \leq v \leq 0.9$. Fig. 2.14 displays the final kink velocity as a function of the initial velocity, where final velocity is measured as the kink in the positive x-axis passes $x = 50$. Similarly to the AB collisions discussed previously, we observe three different scattering outcomes. Firstly, for velocities $0 \leq v \leq 0.476$, the kinks cannot overcome the push outwards from the vacuum, and will escape to infinity without ever colliding. Fig. 2.14(a) shows that the final velocity is always significantly higher than the corresponding initial velocity in this regime.

For velocities greater than the critical velocity $v_{\text{crit}} = 0.476$, there are two possible outcomes: (i) the solitons capture each other and form an oscillon which ultimately decays

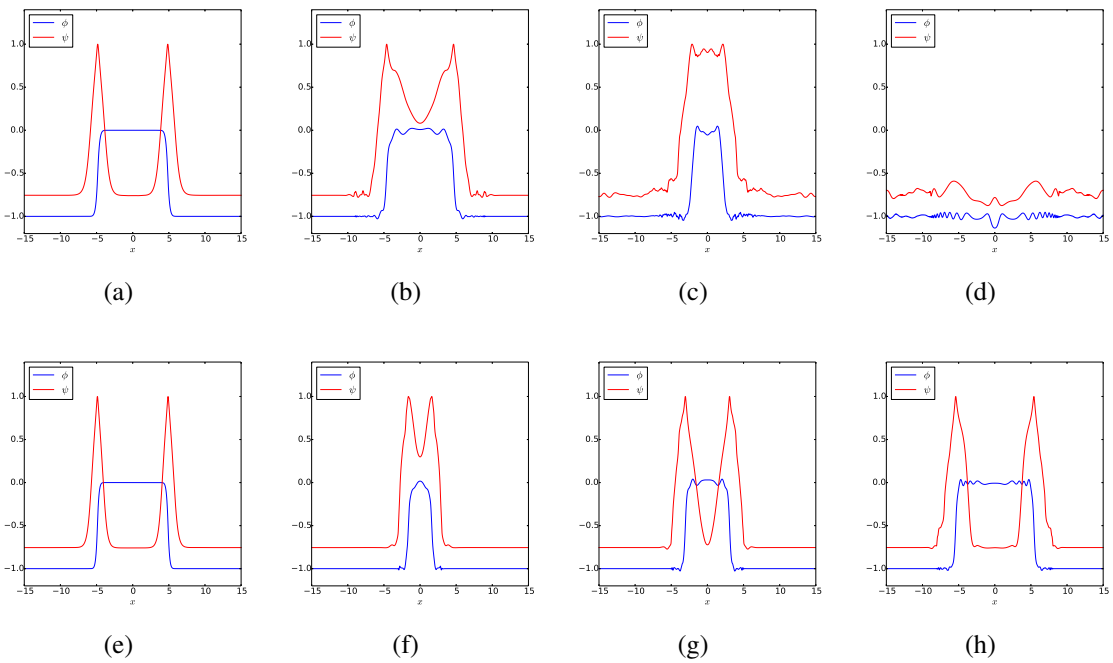

Figure 2.13: For $A\overline{B}$ collisions, we display snapshots of the field configuration for two choices of initial velocity v. (a)-(d) $v = 0.7$: the kinks collide and capture each other, forming an oscillon which ultimately decays to the false vacuum. (e)-(h) $v = 0.8$: the solitons reflect off each other. After three bounces in the shepherd field, they separate and escape to infinity.

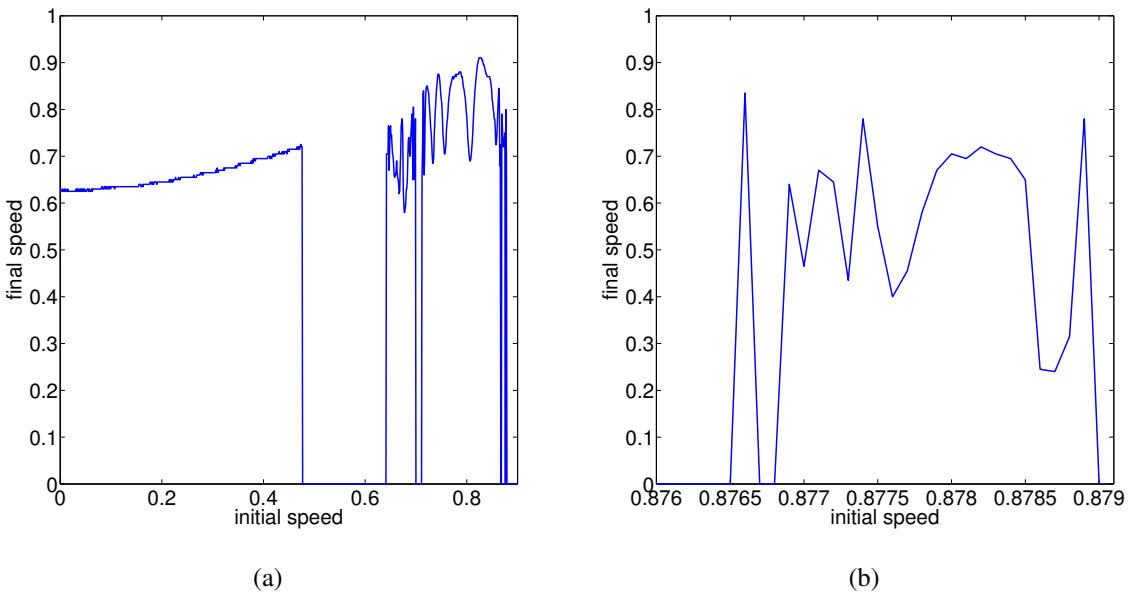

Figure 2.14: (a) The final velocity v_{fin} after an $A\overline{B}$ collision as a function of the initial velocity v. When the final velocity v_{fin} is plotted to be zero, we observe the kinks capture each other, forming an oscillon that ultimately decays to the false vacuum. (b) A closer view of the range $[0.876, 0.88]$ to highlight two windows that are not visible in (a).

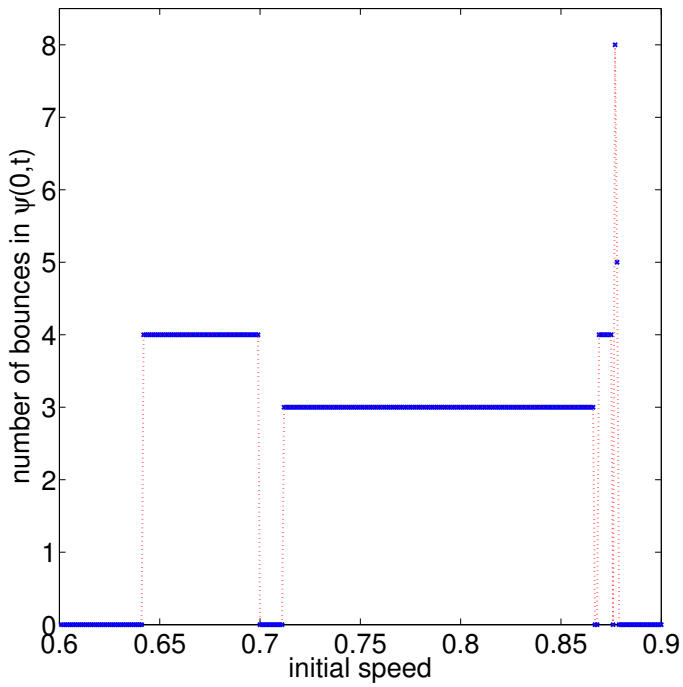

Figure 2.15: Number of bounces as a function of initial velocity v for $A\overline{B}$ collisions. Here the bounce number measures the number of times the shepherd field ψ oscillates at the origin before the solitons separate. If no bounces are counted, then the solitons do not separate, but annihilate to the false vacuum.

to the false vacuum, or (ii) the solitons reflect and separate from each other, escaping to infinity. Case (i), henceforth referred to as *annihilation*, is illustrated by the snapshots in Fig. 2.13(a)-(d), which correspond to the initial velocity $v = 0.7$. The $A\overline{B}$ pair collide and trap each other, as seen in (b) and (c). Ultimately the configuration annihilates to the false vacuum, shown in (d). In Fig. 2.14, the final velocity is plotted to be zero whenever the kinks annihilate. Case (ii), which we will refer to as the *escape* behaviour, is shown by the snapshots in Fig. 2.13(e)-(h), where the initial velocity is $v = 0.8$. The kinks collide and separate, seen in (f) and (g). After three bounces in the shepherd field, the excited solitons travel apart to infinity, which is shown in (h).

In the region $v > 0.476$, Fig 2.14(a) shows that a fractal structure emerges in which there are several distinct windows of the escape behaviour separated by regions of annihilation. This is similar to the kind of fractal structure observed in other soliton models, e.g. see Refs. [13, 26, 18, 27, 28]. In Fig. 2.14(a), we increment the initial velocity by 10^{-3}, and we expect that with greater resolution, more windows would be observed. Fig. 2.14(b) provides

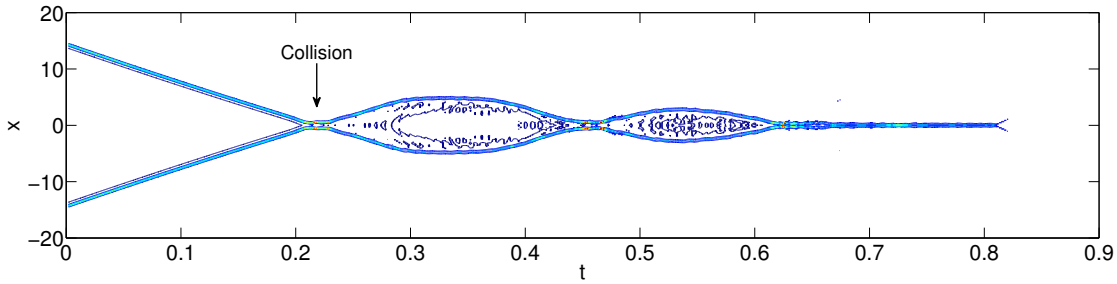

(a)

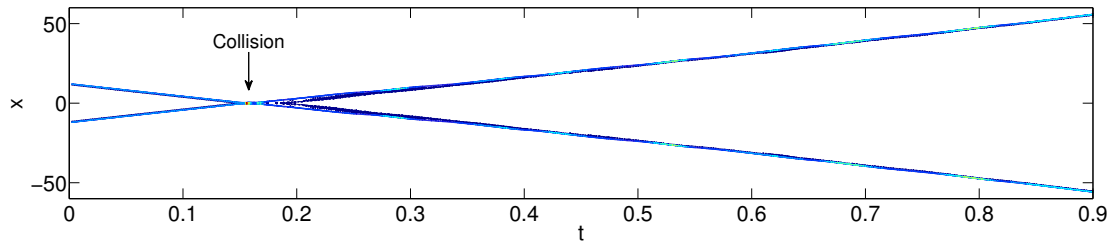

(b)

Figure 2.16: Contour plots of energy density for the sheep field ϕ during $A\overline{B}$ interactions with two different choices of initial velocity v. We indicate the locations of the collisions in the plots. For reasons of clarity, time is divided by 100. (a) $v = 0.7$: the solitons collide and form an oscillon which decays to the false vacuum. (b) $v = 0.8$: the solitons collide and reflect off each other. Once they have separated, the solitons travel apart and escape to infinity.

a closer view of the interval $v \in [0.876, 0.88]$, with initial velocity incremented by 10^{-4}. This shows that there are at least two windows in this interval, though in Fig. 2.14(a) there appeared to be only one.

The windows of escape behaviour can be classified by the number of bounces in the shepherd field ψ at the origin before the solitons separate and escape to infinity. Fig. 2.15 shows the number of bounces in $\psi(0, t)$ as a function of the initial velocity over the interval where these windows appear. We have observed only windows of three bounces or more, with the three bounce window being by far the longest. For $v > 0.866$, the windows are of a much shorter length. In this region, we expect to see more windows emerge if data is taken with a greater resolution. The shortest window is that with 8 bounces, which is the largest number of bounces that we have seen. It is structured as a group of six bounces, with two further bounces occurring after some time. This is unusual compared to the other scattering events, in which all of the bounces in the shepherd field happened close together.

To compare the paths taken by the solitons during $A\overline{B}$ scattering events resulting in annihilation or escape, contour plots of the energy density for the sheep field ϕ with two

choices of initial velocity are contrasted in Fig. 2.16. In Fig. 2.16(a), where $v = 0.7$, the collision of the solitons results in the formation of an oscillon at $t = 80$ (for clarity, time is divided by 100 in the figure). This gradually loses energy, and ultimately annihilates to the false vacuum. The escape behaviour is seen in Fig. 2.16(b), where $v = 0.8$. Here the solitons reflect off each other, and once separated they travel apart and escape to infinity.

2.3 Conclusions

In this chapter, we have numerically investigated kink collisions in a model, first introduced in Ref. [16], which has both true and false vacua. We considered kink solitons in this model interpolating between true and false vacua, and considered the possible combinations of these kinks depending on the vacuum structure. We observed a rich variety of scattering outcomes depending on the choice of initial configuration. We summarise these behaviours in Table 2.2, which indicates whether a specific behaviour was observed for configurations AB, BA, $B\overline{A}$ and $A\overline{B}$ by using a black tick if the behaviour was observed, and a red cross if it was not. The labels used for the different behaviours are: "repulsion" if the kinks escape to infinity without ever colliding, "annihilation" if the kinks form an oscillon that decays to the true or false vacuum, "sticking" if the kinks form a true or false domain wall, and "reflection" if the kinks reflect off each other.

Table 2.2: Summary of the different scattering behaviours observed for AB, BA, $B\overline{A}$ and $A\overline{B}$ kink collisions: repulsion, annhilation, formation of a true or false domain wall ("sticking") and reflecting off each other. Here, the symbol "✓" indicates that the respective behaviour is observed, whereas "✗" denotes that the respective behaviour is not exhibited.

	Repel	Annihilate	Stick	Reflection
AB	✓	✗	✓	✓
BA	✗	✗	✓	✗
$B\overline{A}$	✗	✓	✗	✓
$A\overline{B}$	✓	✓	✗	✓

The vacuum structure of the configuration being studied plays a significant role in determining which scattering behaviours are observed. For AB and $A\overline{B}$ configurations, there are false vacua outside the kinks and true vacuum in between. When evolved from rest,

the kinks will move away from one another to extend the region of true vacuum in between them. For our choice of parameters and initial kink separation, we find that there is a critical value of the initial velocity, $v_{\text{crit}} = 0.476$, below which the kinks cannot overcome the push outwards from the true vacuum, and will escape to infinity without ever colliding. By contrast, for the BA and $B\overline{A}$ configurations, where there is a region of false vacuum in between the kinks and true vacua outside them, the kinks will move towards each other from rest. In these configurations the kinks will always collide.

For AB collisions with initial velocity greater than the critical value, we observe two different types of behaviour: "sticking" (in which a false domain wall is formed) and reflection. There are two windows in which the "sticking" behaviour is found, and in between them is a window of initial velocity in which the kinks reflect off each other and separate to infinity. In the reflection window, we count the number of "bounces" as the number of oscillations in the shepherd field $\psi(0, t)$ at the origin before the kinks separate. Throughout the entire reflection window, three bounces are counted, so we call this a 3-bounce window. The appearance of these types of reflection windows in which the two kinks ultimately escape to infinity has been related in similar kink models to an energy exchange between translational and vibrational modes [13, 20].

In our simulations of BA collisions, we find the same scattering outcome for all initial velocities: the formation of a true domain wall. This is a domain wall interpolating between distinct true vacua, with false vacuum in the core of the domain wall. In such a solution, the sheep field ϕ would be classically stable even without the inclusion of the shepherd field ψ.

The final scattering outcome of any $B\overline{A}$ interaction is the formation of an oscillon that radiates away energy and ultimately annihilates to the true vacuum. There are different ways in which this can happen. Either the kinks capture each other in their first collision and form an oscillon, or they first reflect off one another and travel apart, before being drawn back together and colliding again. Depending on the initial velocity, the second collision results in either annihilation of the kink pair through the formation of an oscillon, or in a number of bounces in the shepherd field. In the latter case, the kinks move apart then return to collide for a third time. In our simulations, we find that any initial velocity resulting in three collisions will see the kinks annihilate by forming an oscillon in the third collision. When refining the resolution of the initial velocity used in our simulations, we expect to find other windows with two or more reflections.

Finally, for $A\overline{B}$ interactions, we find three different types of behaviour: repulsion at low initial velocities, annihilation, and reflecting off each other to escape to infinity. In the annihilation case, the kinks do not annihilate immediately. The $A\overline{B}$ pair forms an oscillon which eventually decays to the true vacuum. Above the critical velocity $v_{\text{crit}} = 0.476$, we find alternating windows of initial velocity in which the reflection and annihilation behaviours occur. These windows form a fractal structure, similar to those observed in other kink models, e.g. see Ref. [18]. When we zoom into the initial kink velocity near to an interface between, for example, a 3-bounce window and an annihilation window, we observe the appearance of more 4-bounce and annihilation windows.

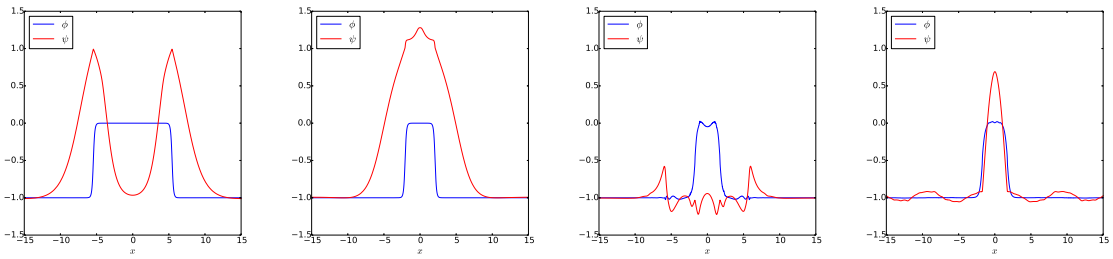

(a) (b) (c) (d)

Figure 2.17: Example of an $A\bar{B}$ kink collision with coupling constants (2.8) chosen to bring our model closer to the sine-Gordon model. We display snapshots of the field configuration for the initial velocity $v = 0.8$: An oscillon in the shepherd field is formed preventing the sheep fields from annihilating or passing through each other.

It is well-known that in the sine-Gordon model, scattering a kink with an antikink can result in the kink and antikink passing through each other. This behaviour was illustrated in the introduction of this thesis in Fig. 1.2(d)-(f). For the parameter choice (2.6) that we have explored in this chapter, we never observe kinks passing through each other. To try and observe this different behaviour within the model [16], we choose the coupling constants so that it approaches the sine-Gordon model. However, we still do not observe the kinks passing through each other. For example, we scatter A and $\bar{B}$ kinks in the model (2.1) with parameters

$$\alpha = 1\,, \quad \beta = 0.05\,, \quad \gamma = 0.01\,, \quad a = 1\,, \quad \epsilon_\psi = 0.1\,, \quad \epsilon_\phi = 0\,, \quad \lambda = 0.01\,. \tag{2.8}$$

This results in an oscillon being formed in the shepherd field ψ which prevents the sheep solitons from passing through each other, see Fig. 2.17. Indeed, the sheep grind to a halt just before passing through each other and remain there for the duration of the simulation.

There are still opportunities for further work on this subject. For instance, one could consider the effect of varying one of the model parameters on the scattering behaviours observed. How would this affect the locations of the critical velocity and alternating windows of behaviour? Would it allow any new types of scattering behaviour? It would also be interesting to study multi-kink solutions and their scattering behaviour. For solutions with an odd number of kinks, this would provide an additional challenge in dealing with the imbalance of having true vacuum at one end of the solution, and false vacuum at the other.

Chapter 3

Baby Skyrme models without a potential term

The baby Skyrme model [5, 6] is a nonlinear field theory admitting topological solitons known as baby Skyrmions. It is often studied as a (2+1)-dimensional analogue of the Skyrme model [7] for nuclear physics though is itself an interesting physical model with applications in condensed matter physics [29, 30, 31]. In the (3+1)-dimensional Skyrme model, the topological solitons are called Skyrmions and can be used to model atomic nuclei with their topological charge, an integer B, giving the baryon number. As a lower-dimensional version of this model, the baby Skyrme model has been used to investigate a variety of difficult problems in the Skyrme theory including Skyrmion scattering [32, 6, 33, 34] and the effect of isorotation on Skyrmion solutions [35, 36, 37].

A key difference between the Skyrme model and the baby Skyrme model arises when we consider their necessary components. The baby Skyrme model is an $O(3)$-sigma model extended by the addition of a term quartic in derivatives called the Skyrme term and a symmetry breaking potential term. The combination of Skyrme term and potential gives a scale to the model and enables it to evade Derrick's theorem [11] for scalar field theories in two space dimensions. By contrast, in the full Skyrme model the combination of the Skyrme and sigma terms is sufficient to evade Derrick's theorem. We design a static baby Skyrme model that does not require a potential term to have topological solitons. One approach is to apply a noncommutative deformation to the baby Skyrme model instead of including a potential term [38, 39]. We apply a very different method.

Before discussing our approach in detail, we briefly review different variants of the baby

Skyrme model. One way to create new models has been through the use of different potentials [40, 41, 42, 43], and it has been found that the choice of potential has a dramatic effect on the solitons of the model. In particular, the appearance and structure of multisolitons depends strongly on the potential term. For some potentials, higher-charge solitons form chains [44], for some rings [43] and for others [45, 46] stable multisolitons may not exist at all. Models have also been designed in which the $O(3)$ symmetry is broken to the dihedral group D_N, and here multi-Skyrmions have been observed with crystalline or broken structures [47, 48, 49].

In addition to choosing a different potential term, it is possible to develop new baby Skyrme models by removing the sigma term. Models consisting of only the Skyrme term and a potential are sometimes called restricted or BPS baby Skyrme models [50, 51, 52]. Deformations of BPS models [53] have also been investigated, for which a physical motivation is found in the (3+1)-dimensional Skyrme theory. One significant problem in applying the Skyrme model to nuclear physics is that the binding energies of Skyrmions are considerably larger than the experimental values. The BPS Skyrme model [54, 55, 56] consists only of a sextic term and a potential term, and has been developed, along with its generalisations, as an attempt to obtain more realistic binding energies. Different approaches to obtain Skyrme models with low binding energies are by coupling vector mesons to the $O(3)$-sigma model term and removing the Skyrme term [57, 58] or by studying Skyrme solitons on curved backgrounds [59].

Another attempt to address the problem of obtaining realistic classical binding energies in the Skyrme theory has been to create new Skyrme models through a novel choice of potential term [60, 61]. A family of models is obtained by a one-parameter family of potential functions interpolating between the standard Skyrme model and a model in which a topological energy bound can be saturated for $|B| = 1$. An equivalent idea has been explored in the baby Skyrme model to obtain so-called "aloof" baby Skyrmions [62]. We have also been motivated by recent interest in topological energy bounds [63, 60]. When designing our models, we require that they satisfy a particular topological energy bound. We find that this has several useful consequences for our models.

Our approach to designing new baby Skyrme models is entirely different from those outlined above. As we wish to design models which do not require a potential term to have topological solitons, we remove the potential and raise the sigma and Skyrme terms to some

powers. Considering Derrick's scaling argument and requiring that our models satisfy a topological energy bound results in a one-parameter family of baby Skyrme models. We find that the required powers of the Skyrme and sigma terms are fractional. This draws a natural comparison between our models and the Nicole [64] and AFZ [65, 66] models, which were investigated numerically in Refs. [67, 68] along with a set of conformally invariant Skyrme-Faddeev models obtained by taking linear combinations of the two.

The outline of the chapter is as follows. We open in Sec. 3.1 with a brief overview of the static baby Skyrme model, focusing on its well-known energy bound and the application of the Derrick scaling argument to this theory. In Sec. 3.2 we present our new models, beginning with a general form for the static energy and then illustrating how the application of Derrick's theorem and the requirement that our solitons satisfy a topological energy bound reduces the number of parameters to one.

In the remainder of the chapter we investigate the solitons of our one-parameter family of models. In Sec. 3.3 we present our numerical results, first considering axially symmetric solutions and then progressing to simulations of the full field theory. We discuss the effect of the model parameter on the solitons and compare them to those found in existing models. We end by summarising our results and reflecting upon open questions and opportunities for further investigation.

3.1 The Baby Skyrme model

The static energy functional of the baby Skyrme model is given by

$$E_{BS} = \int_{\mathbb{R}^2} \left(\frac{1}{2}\partial_i\phi \cdot \partial_i\phi + \frac{1}{4}|\partial_i\phi \times \partial_j\phi|^2 + V(\phi) \right) \mathrm{d}^2x, \tag{3.1}$$

where the field $\phi : \mathbb{R}^2 \to S^2$ is a three-component vector $\phi = (\phi_1, \phi_2, \phi_3)$ of unit length. The first term in (3.1) is the $O(3)$-sigma model term and is extended by the addition of a term quartic in derivatives, called the Skyrme term, and a potential term $V(\phi)$ to allow the existence of stable topological soliton solutions.

To ensure that solutions have finite energy, the boundary condition

$$\lim_{|x|\to\infty} \phi = (0, 0, 1), \tag{3.2}$$

is imposed, assuming that $(0, 0, 1)$ is a minimum of the potential V. This enables a one-point compactification $\mathbb{R}^2 \cup \{\infty\} \cong S^2$, and thus we can consider ϕ as a map $\phi : S^2 \to S^2$. We can

label the maps ϕ by an integer $B \in \pi_2(S^2) = \mathbb{Z}$, called the topological charge. This is the winding number of the map, given by

$$B = -\frac{1}{4\pi}\int_{\mathbb{R}^2} \phi \cdot (\partial_1\phi \times \partial_2\phi)\, \mathrm{d}^2x, \tag{3.3}$$

and is sometimes called the baryon number for comparison with the Skyrme model. The topological solitons of this theory are field configurations which minimise the energy (3.1) in a given topological sector B. They are called baby Skyrmions.

A lower bound on the energy of a solution with charge B in the baby Skyrme model is given by

$$E_{BS} \geq 4\pi|B|. \tag{3.4}$$

This is a bound on the sigma term alone, obtained by a completing the square argument, and is never saturated by baby Skyrmions.

When deriving energy bounds, it will be convenient for us to rewrite the static energy (3.1) using its geometrical interpretation [69]. Define the symmetric, positive definite 2×2 matrix D by

$$D_{ij} = \partial_i\phi \cdot \partial_j\phi, \tag{3.5}$$

and let λ_i^2 denote the eigenvalues of the strain tensor D, where $i = 1, 2$. Then we can express the baby Skyrme energy functional (3.1) in terms of the non-negative eigenvalues of D as

$$E_{BS} = \int_{\mathbb{R}^2} \left(\frac{1}{2}(\lambda_1^2 + \lambda_2^2) + \frac{1}{2}\lambda_1^2\lambda_2^2 + V(\phi)\right)\mathrm{d}^2x, \tag{3.6}$$

and the topological charge can be expressed as

$$B = -\frac{1}{4\pi}\int_{\mathbb{R}^2} \lambda_1\lambda_2\, \mathrm{d}^2x. \tag{3.7}$$

Using the energy (3.6), we can obtain the well-known lower energy bound (3.4) on the sigma term by completing the square as

$$\begin{aligned}\frac{1}{2}\int_{\mathbb{R}^2}(\lambda_1^2 + \lambda_2^2)\, \mathrm{d}^2x &= \frac{1}{2}\Big(\int_{\mathbb{R}^2}(\lambda_1 \mp \lambda_2)^2\, \mathrm{d}^2x \pm 2\int_{\mathbb{R}^2}\lambda_1\lambda_2\, \mathrm{d}^2x\Big),\\ &\geq \Big|\int_{\mathbb{R}^2}\lambda_1\lambda_2\, \mathrm{d}^2x\Big| = 4\pi|B|.\end{aligned} \tag{3.8}$$

The approach given above for deriving topological energy bounds is similar to those given in recent papers on the subject [63, 60]. We will apply this method again in Sec. 3.2.2 when

we derive energy bounds for our new baby Skyrme models. While (3.4) is a well-known topological energy bound for the baby Skyrme model, recently tighter bounds have been obtained by also taking into account energy contributions from the Skyrme term and the potential term [51, 63].

The inclusion of a potential term in the baby Skyrme model is important as it allows the model to evade Derrick's theorem [11] and thus have topological soliton solutions. This theorem rules out the existence of topological solitons in flat space scalar field theories by the requirement that a stationary point of the energy must also be stationary against rescaling. Therefore, if the energy of the theory after applying the spatial rescaling $x \mapsto \mu x$, which we denote by $e(\mu)$, has no stationary point, then there can be no static finite energy solutions except the vacuum.

We apply this argument to the baby Skyrme model. Under the rescaling $x \mapsto \mu x$, the static energy (3.1) becomes

$$e_{BS}(\mu) = E_2 + \mu^2 E_4 + \mu^{-2} E_0, \tag{3.9}$$

where we use E_2, E_4 and E_0 to denote the sigma term, Skyrme term and potential term, respectively. As a result of Derrick's theorem, we observe that the combination of a potential term and the Skyrme term allows the existence of topological solitons.

We can also derive a virial theorem satisfied by the baby Skyrme model by taking $\frac{de_{BS}}{d\mu}|_{\mu=1}$ and setting this to zero, to find

$$E_4 = E_0. \tag{3.10}$$

Contrast this with the results of applying the scaling argument to the Skyrme model, which has static energy

$$E_S = \int_{\mathbb{R}^3} \left(-\frac{1}{2}\mathrm{Tr}(R_i R_i) - \frac{1}{16}\mathrm{Tr}([R_i, R_j][R_i, R_j]) + m^2 \mathrm{Tr}(1 - U) \right) \mathrm{d}^3 x, \tag{3.11}$$

where m is related to the pion mass, the pion fields are written as $U : \mathbb{R}^3 \to \mathrm{SU}(2)$ and $R_i = (\partial_i U) U^\dagger$.

In this case, applying the rescaling produces

$$e_S(\mu) = \frac{1}{\mu} E_2 + \mu E_4 + \frac{1}{\mu^3} E_0, \tag{3.12}$$

so the potential term is unnecessary to evade Derrick's theorem. If we consider the static energy of the Skyrme model with no potential term, we can further obtain the virial theorem

$$E_2 = E_4. \tag{3.13}$$

We have seen that the potential term is a necessary component of the baby Skyrme model if there are to exist topological soliton solutions. However, the same is not true of the Skyrme model, in which Skyrmions can exist without the presence of a potential term. This difference between the two theories motivates us to investigate the design of baby Skyrme models that do not include a potential term but still have soliton solutions.

Many different functions $V(\phi)$ have been investigated as the potential term in the baby Skyrme model [40, 41, 42, 43]. Particular examples are

$$V(\phi) = \begin{cases} V_1 = m^2(1-\phi_3) & \text{(“old” potential)}, \\ V_2 = m^2(1-\phi_3^2) & \text{(“new” potential)}, \\ V_3 = m^2(1-\phi_3)^4 & \text{(holomorphic potential)}. \end{cases} \tag{3.14}$$

In Fig. 3.1, we present contour plots of energy density for the minimal energy solutions of topological charge $B = 1, 2, 3, 4$ in the baby Skyrme model with potentials V_1 and V_2. In the old baby Skyrme model V_1, higher-charge baby Skyrmions form chains [44], whereas in the new baby Skyrme model V_2 multisolitons form rings [43].

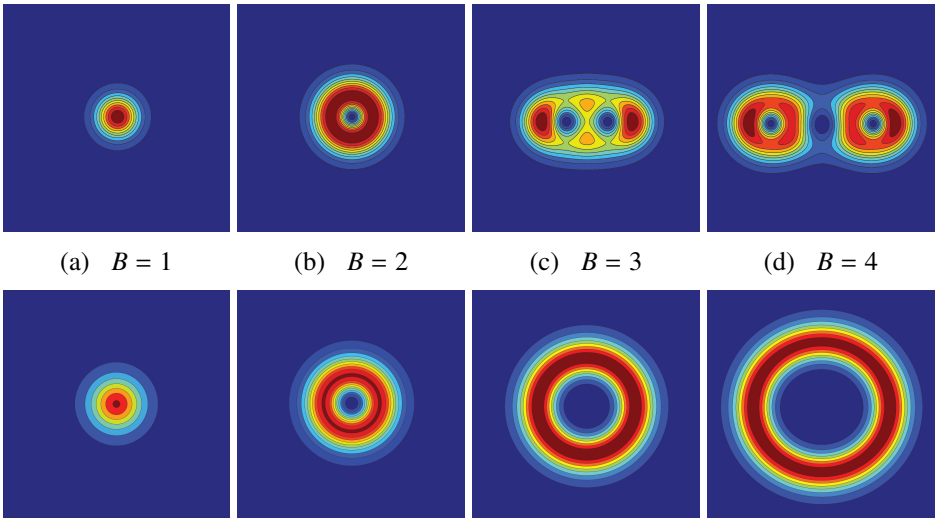

(a) $B = 1$ (b) $B = 2$ (c) $B = 3$ (d) $B = 4$

(e) $B = 1$ (f) $B = 2$ (g) $B = 3$ (h) $B = 4$

Figure 3.1: Contour plots of energy density for solitons of topological charge $B = 1, 2, 3, 4$ in the baby Skyrme model (3.1) with (a) - (d): the old potential V_1, (e) - (h): the new potential V_2.

For the holomorphic potential V_3, the static charge one soliton is given exactly by

$$\phi = \left(\frac{2\lambda x_1}{x_1^2 + x_2^2 + \lambda^2}, \frac{2\lambda x_2}{x_1^2 + x_2^2 + \lambda^2}, \frac{x_1^2 + x_2^2 - \lambda^2}{x_1^2 + x_2^2 + \lambda^2} \right), \tag{3.15}$$

where $\lambda = 1/(2^{\frac{1}{4}}\sqrt{m})$ is the width of the soliton and $x_1,\ x_2$ are the spatial coordinates . However, this potential produces a repulsive force between solitons, and no multisolitons exist [45, 46].

3.2 Baby Skyrme models without a potential

We propose a range of new baby Skyrme models that do not require a potential term to evade Derrick's theorem. To achieve this, we raise the sigma and Skyrme terms to the power α and β, respectively, and determine the range of acceptable values for these powers to ensure stability with respect to rescaling. As a starting point for the new static energy, take

$$E = \int_{\mathbb{R}^2} \left(c_1(\partial_i\phi \cdot \partial_i\phi)^\alpha + c_2(|\partial_i\phi \times \partial_j\phi|^2)^\beta \right) \mathrm{d}^2x, \tag{3.16}$$

where $c_1,\ c_2$ are positive real coupling constants, and $\alpha,\ \beta$ are real constants.

3.2.1 Derrick's scaling argument

To determine suitable values for α and β, we apply the rescaling $x \mapsto \mu x$ to the static energy (3.16) and consider the results of Derrick's theorem. This leads to the energy

$$e(\mu) = \mu^{2\alpha-2}E_2 + \mu^{4\beta-2}E_4. \tag{3.17}$$

There are three cases in which our model can evade Derrick's theorem:

$$\begin{aligned} &\text{(i)} \quad \alpha < 1 \ \text{ and } \ \beta > 0.5, \\ &\text{(ii)} \quad \alpha > 1 \ \text{ and } \ \beta < 0.5, \\ &\text{(iii)} \quad \alpha = 1 \ \text{ and } \ \beta = 0.5, \end{aligned} \tag{3.18}$$

with case (iii) providing a scale invariant model. We only consider cases (i) and (iii) because solutions in the models of case (ii) would either be compact or not have finite energy; see Appendix B.1 for a detailed discussion.

There is also a virial theorem satisfied by our models. Take $\frac{de}{d\mu}|_{\mu=1}$ and set this equal to zero. For case (iii) this is automatically satisfied; otherwise, we have

$$(2\alpha - 2)E_2 + (4\beta - 2)E_4 = 0. \tag{3.19}$$

The resulting virial theorem is

$$E_2 = \frac{1 - 2\beta}{\alpha - 1}\, E_4. \tag{3.20}$$

Recall that the Skyrme model without a potential term satisfies the virial theorem $E_2 = E_4$. Our models also satisfy this virial theorem when

$$\beta = 1 - \frac{\alpha}{2}. \tag{3.21}$$

This selection of models includes one in which the static energy (3.16) produces the same function $e_S(\mu)$ under rescaling as that for the Skyrme model (3.11) without a potential term. In this case the parameters are $\alpha = 0.5$ and $\beta = 0.75$.

3.2.2 Energy bounds

We have seen in Sec. 3.1 that the baby Skyrme model (3.1) satisfies a linear bound (3.4) on the energy of its solutions in terms of the number of solitons. This is a useful property shared by many soliton models [3]. Therefore, we require our new baby Skyrme models to satisfy such a lower bound on the energy. In the following, we use this condition to fix the parameter β in (3.16) and further restrict the family of models that we consider.

Defining the matrix D by $D_{ij} = \partial_i\phi \cdot \partial_j\phi$ as before, rewrite the energy (3.16) as

$$E = \int_{\mathbb{R}^2} \left(c_1(\lambda_1^2 + \lambda_2^2)^\alpha + c_2(2\lambda_1^2\lambda_2^2)^\beta \right) \mathrm{d}^2x, \tag{3.22}$$

where $\lambda_1^2,\ \lambda_2^2$ denote the eigenvalues of D.

To obtain a lower bound on the energy, we use the following special case of the inequality of the arithmetic and geometric means: for a, b non-negative,

$$\frac{a+b}{2} \geq \sqrt{ab}, \tag{3.23}$$

with equality if and only if $a = b$.

We obtain a lower bound on the energy by first applying inequality (3.23) twice to find

$$\begin{aligned} E &= 2\int_{\mathbb{R}^2} \left(\frac{1}{2}c_1(\lambda_1^2 + \lambda_2^2)^\alpha + \frac{1}{2}c_2(2\lambda_1^2\lambda_2^2)^\beta \right) \mathrm{d}^2x, \\ &\geq 2\int_{\mathbb{R}^2} \sqrt{c_1}(\lambda_1^2 + \lambda_2^2)^{\frac{\alpha}{2}} \sqrt{c_2}(2\lambda_1^2\lambda_2^2)^{\frac{\beta}{2}} \mathrm{d}^2x, \\ &\geq 2^{1+\frac{\beta}{2}} \sqrt{c_1c_2} \int_{\mathbb{R}^2} 2^{\frac{\alpha}{2}} |\lambda_1\lambda_2|^{\frac{\alpha}{2}} |\lambda_1\lambda_2|^\beta \mathrm{d}^2x, \\ &= 2^{1+\frac{\alpha+\beta}{2}} \sqrt{c_1c_2} \int_{\mathbb{R}^2} |\lambda_1\lambda_2|^{\frac{\alpha+2\beta}{2}} \mathrm{d}^2x. \end{aligned} \tag{3.24}$$

Then to ensure that the energy bound resulting from this calculation is linear in terms of the topological charge B, the required value of β is

$$\beta = 1 - \frac{\alpha}{2}. \tag{3.25}$$

The resulting topological energy bound is

$$E \geq 2^{\frac{3}{2}+\frac{\alpha}{4}} \sqrt{c_1 c_2}\, 4\pi |B|. \tag{3.26}$$

We note that the relation (3.25) between α and β is not necessary for models of the form (3.16) to have a linear energy bound. We can generalise our topological energy bound by splitting up the second term in the energy (3.22) into M components and using the inequality of the arithmetic and geometric means for $M+1$ components. Then the condition for a linear bound is

$$\beta = (M + 1 - \alpha)/2M. \tag{3.27}$$

Our bound is reproduced when setting $M = 1$. We choose to work with this relation between α and β because it was also found in Sec. 3.2.1 by requiring that the virial theorem (3.20) be simply $E_2 = E_4$: the virial theorem of the Skyrme model without a potential term.

In case (iii), there is an alternative energy bound derived by a standard completing the square argument. Here the static energy is given in terms of the eigenvalues $\lambda_1^2,\ \lambda_2^2$ as

$$E = \int_{\mathbb{R}^2} \left(c_1(\lambda_1^2 + \lambda_2^2) + c_2 \sqrt{2\lambda_1^2\lambda_2^2} \right) \mathrm{d}^2 x. \tag{3.28}$$

By completing the square, we find

$$\begin{aligned} E &= \int_{\mathbb{R}^2} \left(c_1(|\lambda_1| - |\lambda_2|)^2 + 2c_1|\lambda_1\lambda_2| + \sqrt{2}c_2|\lambda_1\lambda_2| \right) \mathrm{d}^2 x, \\ &= \int_{\mathbb{R}^2} c_1(|\lambda_1| - |\lambda_2|)^2 \mathrm{d}^2 x + (2c_1 + \sqrt{2}c_2) \int_{\mathbb{R}^2} |\lambda_1\lambda_2|\, \mathrm{d}^2 x, \\ &\geq 4\pi(2c_1 + \sqrt{2}c_2)|B|. \end{aligned} \tag{3.29}$$

So an alternative bound in case (iii) is given by

$$E \geq 4\pi(2c_1 + \sqrt{2}c_2)|B|. \tag{3.30}$$

This bound is saturated for solutions of the Bogomolny equation,

$$|\lambda_1| = |\lambda_2|, \tag{3.31}$$

which leads to the following system of equations:

$$\partial_1\phi \cdot \partial_1\phi = \partial_2\phi \cdot \partial_2\phi, \tag{3.32a}$$

$$\partial_1\phi \cdot \partial_2\phi = 0. \tag{3.32b}$$

Let z denote the complex coordinate $z = x + iy$ in the spatial plane and R the Riemann sphere coordinate on the target S^2. We can write solutions of Eqs. (3.32) in each topological sector B in terms of rational maps $R(z)$ as

$$\phi = \frac{1}{1+|R|^2}\Big(R + \bar{R},\ \ -i(R-\bar{R}),\ |R|^2 - 1\Big). \tag{3.33}$$

Here $R(z) = p(z)/q(z)$ is a ratio of two polynomials $p(z)$ and $q(z)$ with no common factors, and $B = \max\{\deg(p), \deg(q)\}$. To satisfy the boundary condition $\lim_{|x|\to\infty} \phi = (0,0,1)$ at infinity, we require $R(\infty) = \infty$. One important case is the axially symmetric rational map

$$R(z) = z^B. \tag{3.34}$$

Thus, we can find exact solutions for baby Skyrmions of any charge B in this model. In fact, this particular model is equivalent to the $O(3)$ sigma model. This is because taking $\alpha = 1$ and $\beta = 0.5$ gives the sum of the usual sigma term and the topological charge density. Since the topological charge density always integrates to a constant, the addition of this term to the $O(3)$ sigma model does not change the equations of motion and the solutions we find are the usual sigma model lumps.

It still remains to set the values of the coupling constants c_1 and c_2. In this paper, we choose

$$c_1 = 2^{-\frac{3+\alpha}{2}} \quad \text{and} \quad c_2 = 2^{\frac{\alpha}{2}} c_1, \tag{3.35}$$

and so obtain the final form of the static energy for our models as

$$E = 2^{-\frac{3+\alpha}{2}} \int_{\mathbb{R}^2} \Big((\partial_i\phi \cdot \partial_i\phi)^\alpha + 2(|\partial_1\phi \times \partial_2\phi|^2)^{1-\frac{\alpha}{2}} \Big) \mathrm{d}^2x. \tag{3.36}$$

This choice of coupling constants has three useful consequences. First, the choice of c_2 ensures that the bounds (3.26) and (3.30) in case (iii) coincide. It also causes the virial theorem $E_2 = E_4$ to be satisfied in case (iii), as we now have $c_1 = \frac{1}{4}$ and $c_2 = \frac{1}{2\sqrt{2}}$ and thus,

$$E_2 = 2c_1 \cdot 4\pi|B| = 2\pi|B| = \sqrt{2}c_2 \cdot 4\pi|B| = E_4. \tag{3.37}$$

Due to the scale invariance of this model, it is not necessary that the virial theorem be satisfied in this case. It is only due to the choice of constants (3.35) that the virial theorem (3.13) holds here.

Finally, for any choice of α, this combination of c_1 and c_2 sets the topological energy bound (3.26) to be

$$E \geq 4\pi|B|, \tag{3.38}$$

with the bound saturated when $\alpha = 1$. This is the well-known energy bound on the sigma term of the baby Skyrme model.

3.3 Numerical results

In this section, we calculate axially symmetric baby Skyrmion solutions for parameter $\alpha \in [0.5, 1]$ and with topological charges $B = 1 - 3, 10$. We minimise the energy functional (3.36) for rotationally symmetric Skyrme configurations using two different numerical approaches: 1D gradient flow and Newton's method for nonlinear systems. Finally, we perfom 2D energy minimisation simulations for a selection of our models and verify that the minimal energy solutions agree with those found when imposing axial symmetry. Skyrmion chain solutions are found to be of higher energy.

Note that the baby Skyrmion solutions for $\alpha = 0.5$ are discussed in a separate subsection as the solitons become *compactons*. These are solitons with compact support, taking vacuum values everywhere outside some finite region of space. Compact solitons have been studied before in the Skyrme-Faddeev model in the infinite mass limit [70], and in massive baby Skyrme models [71, 51, 72]. Compactons are numerically challenging and require a careful adjustment of our numerical methods.

3.3.1 Axial baby Skyrme solutions

To find axially symmetric soliton solutions of the equations of motion, we use the ansatz

$$\phi = (\sin f \cos(B\theta),\ \ \sin f \sin(B\theta),\ \ \cos f), \tag{3.39}$$

where r, θ are the usual polar coordinates, $f = f(r)$ is a radial profile function, and B is the topological charge of the configuration. Substituting (3.39) into (3.36) yields the energy

$$E = 2^{-\frac{3+\alpha}{2}} \cdot 2\pi \int_0^\infty \left(\left(f'^2 + B^2 \frac{\sin^2 f}{r^2} \right)^\alpha + 2 \left(f'^2 B^2 \frac{\sin^2 f}{r^2} \right)^{1-\frac{\alpha}{2}} \right) r\mathrm{d}r, \tag{3.40}$$

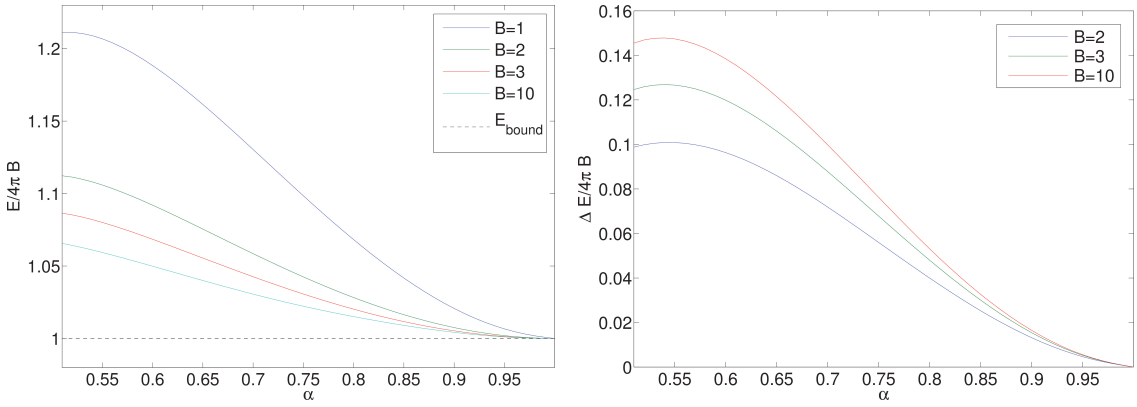

(a) (b)

Figure 3.2: Energy as a function of model parameter α for axially symmetric configurations with topological charges $B = 1 - 3,\ 10$. (a) Total energy E. (b) Binding energy per soliton $\Delta E/4\pi B$.

which depends only on the radial coordinate r. Here prime denotes differentiation with respect to the radial coordinate r. By the principle of symmetric criticality [3], solutions of the Euler-Lagrange equation for the simplified energy (3.40) will also solve the equations of motion for the original energy (3.36). However it is not guaranteed that the solutions found are minima of the full equations, and they could instead be saddle points. In the following, we minimise the energy (3.40) by solving the Euler-Lagrange equation (B.1) given in Appendix B.1 subject to the boundary conditions $f(0) = \pi$ and $f(\infty) = 0$ in two ways: through the use of a 1D flow method and also using Newton's method for nonlinear systems [73] with grid spacing $\Delta r = 10^{-4}$ over the interval $0 \leq r \leq 20$. For both methods, we monitor the topological charge and check the virial theorem (3.20) at each iteration step.

Figure 3.2(a) displays the total energy E as a function of model parameter α for axially symmetric baby Skyrmions with topological charges $B = 1 - 3, 10$. The topological energy bound is indicated by a dashed line. All energy values are given in units of $4\pi B$. The energy values are furthest from the bound towards $\alpha = 0.5$, but draw closer as α increases until the bound is finally saturated in the $\alpha = 1$ baby Skyrme model. As the charge increases, the difference between the energy value and the bound grows smaller. So the bound tightens for higher-charge solutions of a given model. Note that the energy difference between subsequent charges also decreases drastically. As a limiting case, we include in Fig. 3.2 the energy values for charge 10. In Fig. 3.2(b) we display the binding energy as a function of α,

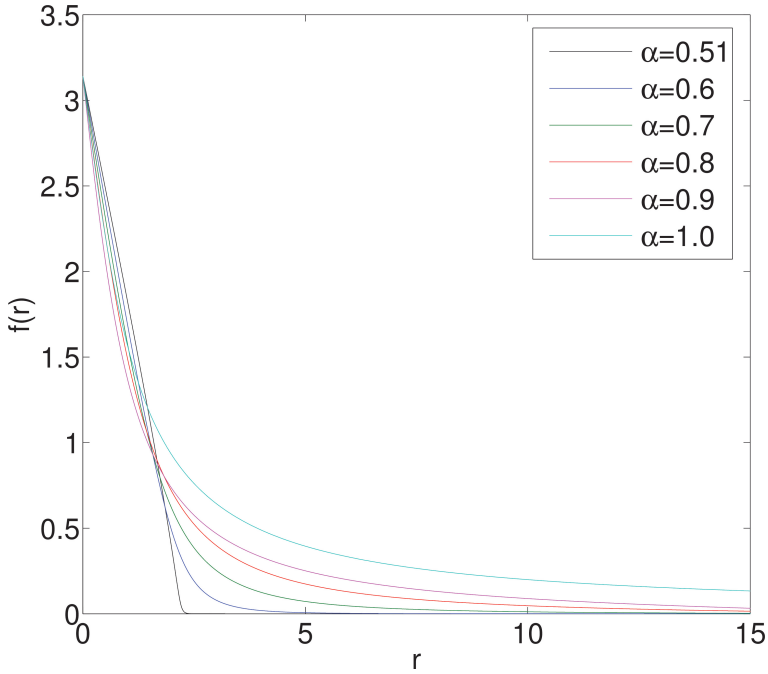

Figure 3.3: $B = 1$ profile functions $f(r)$ for model parameter $0.5 < \alpha \leq 1$.

where the binding energy per soliton is given by

$$\frac{\Delta E}{B} = E_1 - \frac{E_B}{B}, \tag{3.41}$$

with E_1 denoting the energy of the charge one solution and E_B denoting the energy of the charge B solution. The binding energy per soliton is the energy required to split a charge B baby Skyrmion into B charge one Skyrmions, divided by the total number of solitons. The binding energy is found to increase with the topological charge.

Another feature of the solutions which changes dramatically as α increases is illustrated in Fig. 3.3. Here we compare charge one profile functions $f(r)$ in a selection of the models ranging from $\alpha = 0.51$ to $\alpha = 0.9$ with the exact solution of the Bogomolny equation for $\alpha = 1$. The numerical profile functions were calculated using the Newton method over the interval $0 \leq r \leq 20$. For $\alpha = 0.51$, the profile function is tightly concentrated between $r = 0$ and $r = 2.2$. As α increases, the profile functions start to spread out. By $\alpha = 1$, the profile function is less localised and approaches the vacuum gradually.

A more detailed examination of the approach to the vacuum of the profile functions is given in Appendix B.1. In this appendix, we linearise the equation of motion as $r \to \infty$ and obtain solutions that describe the profile functions as they approach zero. The profile functions exhibit a power law behavior, $f(r) \sim r^{\lambda}$ for large r. As α tends to 0.5 the exponent

λ becomes increasingly negative, and the approach to the vacuum becomes steeper. At $\alpha = 0.5$ the exponent diverges suggesting that solutions in this model are compactons. Near the origin, for all values of α the charge one profile functions exhibit linear behavior. This is discussed in detail in Appendix B.2 where we linearise the equation of motion near the origin for any charge B.

3.3.2 Baby Skyrme solutions in the $\alpha = 0.5$ model

In this section, we present the results of 2D simulations for the compact charge one and two solitons obtained for model parameter $\alpha = 0.5$. As a starting point for our 2D energy minimisation routine we choose two different initial conditions: a rotationally symmetric configuration created from the 1D profile function for $\alpha = 0.5$ and the configuration relaxed with $\alpha = 0.51$.

To find profile functions in the $\alpha = 0.5$ model we minimise the energy (3.40) over intervals $r \in [0, R_{\text{est}}]$ for various boundary points R_{est} surrounding the expected compacton radius. Solving the corresponding field equation over each interval is accomplished by Newton's method for nonlinear systems with grid spacing $\Delta r = 10^{-2}$ due to its increased speed over the gradient flow method. We then seek the value of R_{est} that minimises the energy. This enables us to decide upon a numerical energy value for the solution up to one decimal place of accuracy, with the virial theorem and topological charge also correct to one decimal place.

By substituting the profile functions obtained by this method into the axially symmetric ansatz (3.39), we build 2D configurations. These are implemented as initial configurations in a 2D relaxation method similar to that described in Ref. [35]. We evolve the equations of motion derived from (3.36) in a fictitious time t and include a damping term governed by the dissipation ϵ. We periodically remove kinetic energy by setting $\dot{\phi} = 0$ at all grid points. In the following, the finite difference approximations are second-order accurate in the spatial derivatives. The simulations are performed on a $(401)^2$ grid with spacing Δx=0.02 for the charge one soliton and $\Delta x = 0.04$ for the charge two soliton. In both cases the dissipation parameter ϵ is set to 0.5.

In Fig. 3.4(a) we plot the energy density of the resulting $B = 1$ configuration. Figure 3.5(a) displays the energy density of a $B = 2$ configuration obtained by the same method. The energy of both solutions is localized in a finite region of space, and the steep approach

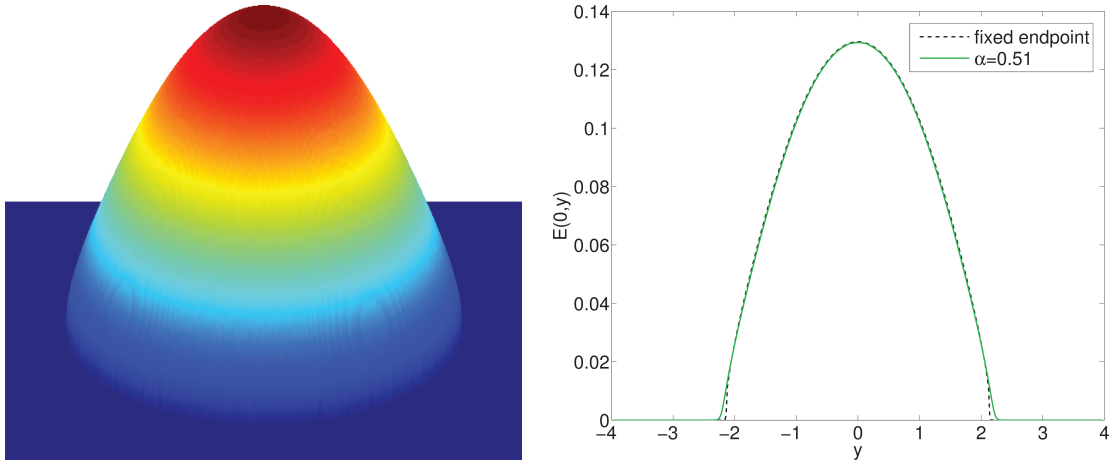

(a) (b)

Figure 3.4: Energy density for charge one baby Skyrmions with model parameter $\alpha = 0.5$. (a) Surface plot of the energy density. (b) We compare slices through the energy density obtained when relaxing two different $B = 1$ initial conditions: a baby Skyrme configuration relaxed with $\alpha = 0.51$ (green line) and a rotationally symmetric configuration generated from an $\alpha = 0.5$ profile function.

to the vacuum is evident at the boundaries of the compactons. The energy values for these solutions agree with those of the corresponding profile functions to one decimal place and are given in Table 3.1.

The second method that we implement to find solutions in this model is to take a 2D configuration with $\alpha = 0.51$ as an initial condition in the 2D relaxation code. The same grid and spacing are chosen as for the previous initial configuration. In Fig. 3.4(b) we compare charge one solutions obtained by both methods. We display slices along $x = 0$ through their energy density. The same comparison for charge two solitons is presented in Fig. 3.5(b). While the approach to the vacuum is not as steep for the second method, both methods generally agree well and describe the soliton's energy to one decimal place.

3.3.3 Higher charge solutions

To verify our axially symmetric charge one and two solutions and to investigate solutions of higher charge, we implement a 2D numerical method. We apply the same relaxation method as in the previous section, but with a different grid. For models excluding $\alpha = 0.5$, we use a $(201)^2$ grid with spacing $\Delta x = 0.2$. To create initial configurations, we substitute our numerical profile functions into the axial ansatz (3.39) to generate 2D configurations. We

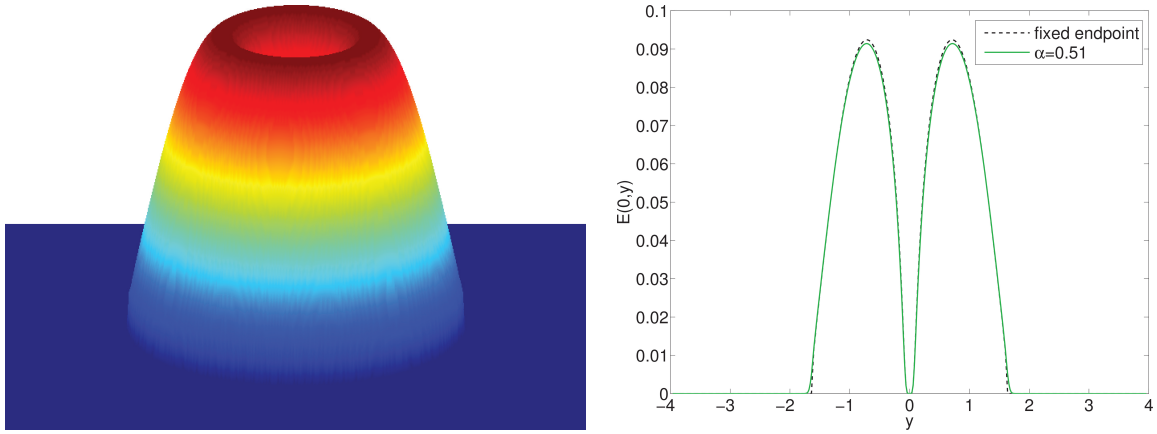

(a) (b)

Figure 3.5: Energy density for charge two baby Skyrmions with model parameter $\alpha = 0.5$. (a) Surface plot of the energy density. (b) We compare slices through the energy density obtained when relaxing two different $B = 2$ initial conditions: a baby Skyrme configuration relaxed with $\alpha = 0.51$ (green line) and a rotationally symmetric configuration generated from an $\alpha = 0.5$ profile function.

then take these configurations as initial conditions for our 2D energy minimisation algorithm to find solitons of different α values. For example, an $\alpha = 0.8$ axial solution is chosen as an initial configuration to obtain the $\alpha = 0.7$ solution.

In Table 3.1 we give the energy values of our numerical simulations for a selection of α values. All energy values are given in units of $4\pi B$, motivated by the energy bound of our models (3.38). We also present the binding energy for the 2D configurations, calculated using (3.41). For axial solutions the results of our 2D simulations agree to between two and three decimal places with the values obtained when minimising (3.40).

For higher charges, axial solutions remain the energetic minima, though other configurations have been obtained. In particular, we find chain configurations in our models by using three solitons in a line as an initial configuration. The energy values for the chain configurations are also presented in Table 3.1 and are denoted by a $*$. Their energy is higher than that of the axial configurations, and they do not satisfy the virial theorem. So these are local minima but not the global energy minimisers.

In Fig. 3.6 we compare the energies obtained by 1D gradient flow with those calculated by 2D relaxation for baby Skyrmions with topological charges $B = 1$ - 3. We plot the energy for axially symmetric configurations with model parameter $\alpha = 0.51$ - 1.0 and indicate all energy values computed by the full field simulations by points. As before, the topological

Table 3.1: Energy values obtained from full field simulations ($E^{(2D)}/4\pi B$) when compared to 1D gradient flow results ($E^{(1D)}/4\pi B$). The binding energy per soliton $\Delta E/4\pi B$ is calculated by (3.41) using the numerical 2D energy results. The two $B = 3$ configurations given are the axial solution (3.39) and the chain configuration of Fig. 3.8 which is denoted by 3*.

α	β	B	$E^{(1D)}/4\pi B$	$E^{(2D)}/4\pi B$	$\Delta E/4\pi B$
0.5	0.75	1	1.2	1.2	0.0
0.5	0.75	2	1.1	1.1	0.1
0.6	0.7	1	1.188	1.188	0.0
0.6	0.7	2	1.092	1.092	0.096
0.6	0.7	3	1.068	1.069	0.119
0.6	0.7	3*	—	1.081	0.107
0.7	0.65	1	1.130	1.130	0.0
0.7	0.65	2	1.059	1.058	0.072
0.7	0.65	3	1.043	1.042	0.088
0.7	0.65	3*	—	1.056	0.074
0.8	0.6	1	1.068	1.068	0.0
0.8	0.6	2	1.028	1.029	0.039
0.8	0.6	3	1.020	1.020	0.048
0.8	0.6	3*	—	1.036	0.032
0.9	0.55	1	1.021	1.020	0.0
0.9	0.55	2	1.008	1.007	0.013
0.9	0.55	3	1.005	1.005	0.015
0.9	0.55	3*	—	1.009	0.011

energy bound is indicated by a black dashed line. The black points denote the energy of axially symmetric baby Skyrmions calculated by full field relaxation. They lie on top of the lines showing the energy for baby Skyrmions of the same topological charge obtained by 1D gradient flow. The energy for charge three chain configurations is also included in the figure as a series of red points connected by a dashed red line. For $\alpha = 0.8$ the energy of the $B = 3$ chain is slightly higher than the $B = 2$ solution, but much lower than the $B = 1$ solution. So, it is *not* energetically favourable for the chain to split up into a $B = 1$ and $B = 2$ Skyrmion.

The energy density for $B = 1$ - 3 baby Skyrmions with $\alpha = 0.6$ - 0.9 is plotted in Fig. 3.7. They are all axially symmetric, and the effect of increasing α on the solutions can be seen by

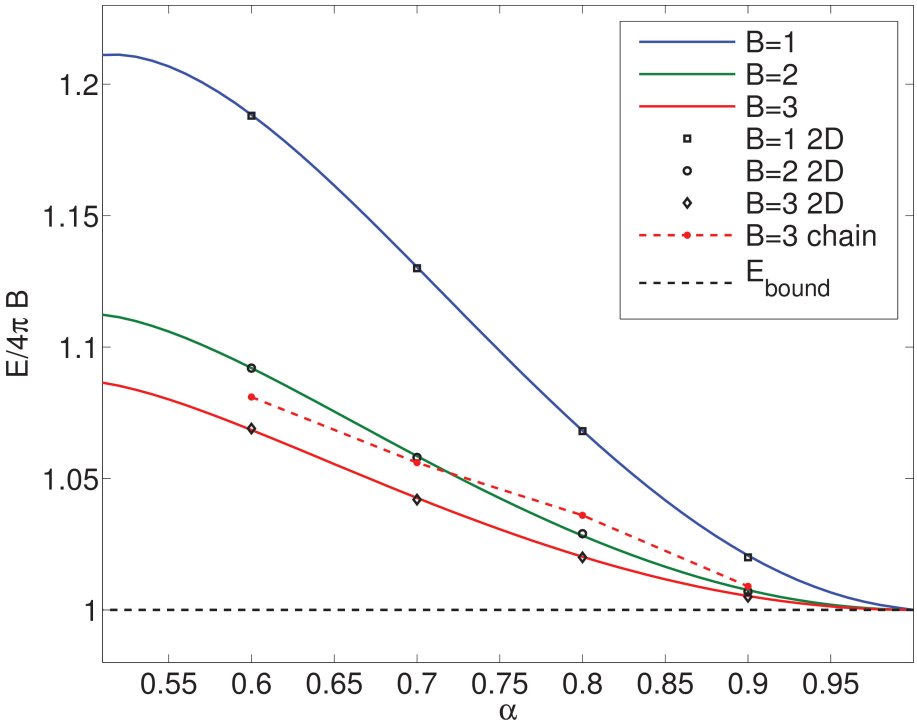

Figure 3.6: Total energy E for baby Skyrmions obtained with the axial ansatz (3.39) and for baby Skyrmions obtained with the 2D relaxation method.

comparing the graphs. This is most noticeable for the charge one solitons, where the energy density of the $\alpha = 0.6$ solution is concentrated over a wide area with only a small tail. As α increases, the tail of the energy density becomes wider while the area in which the energy density is most concentrated decreases in width and increases in height. A similar effect occurs for the charge two and three rings, which become thinner and taller as α increases.

In Fig. 3.8, we display the energy density of chain configurations for the same selection of models. The structure of the chain configurations changes significantly as α increases. For $\alpha = 0.6$, the solitons are very close together but as α increases, the chain starts to pull apart. For $\alpha = 0.9$, the chain almost splits into three separate solitons, though they remain close enough to deform each other. This may be explained by the approach to the Bogomolny solutions at $\alpha = 1$. The attraction between solitons becomes weaker and weaker until they do not feel any attraction or repulsion at $\alpha = 1$. Then the baby Skyrmions can be placed at arbitrary positions. In fact the solution space is the space of based rational maps. In the $\alpha = 1$ model, the energy of three separate solitons is identical to that of a three-soliton ring solution.

The chains observed at the lower α values most resemble those found in the baby Skyrme

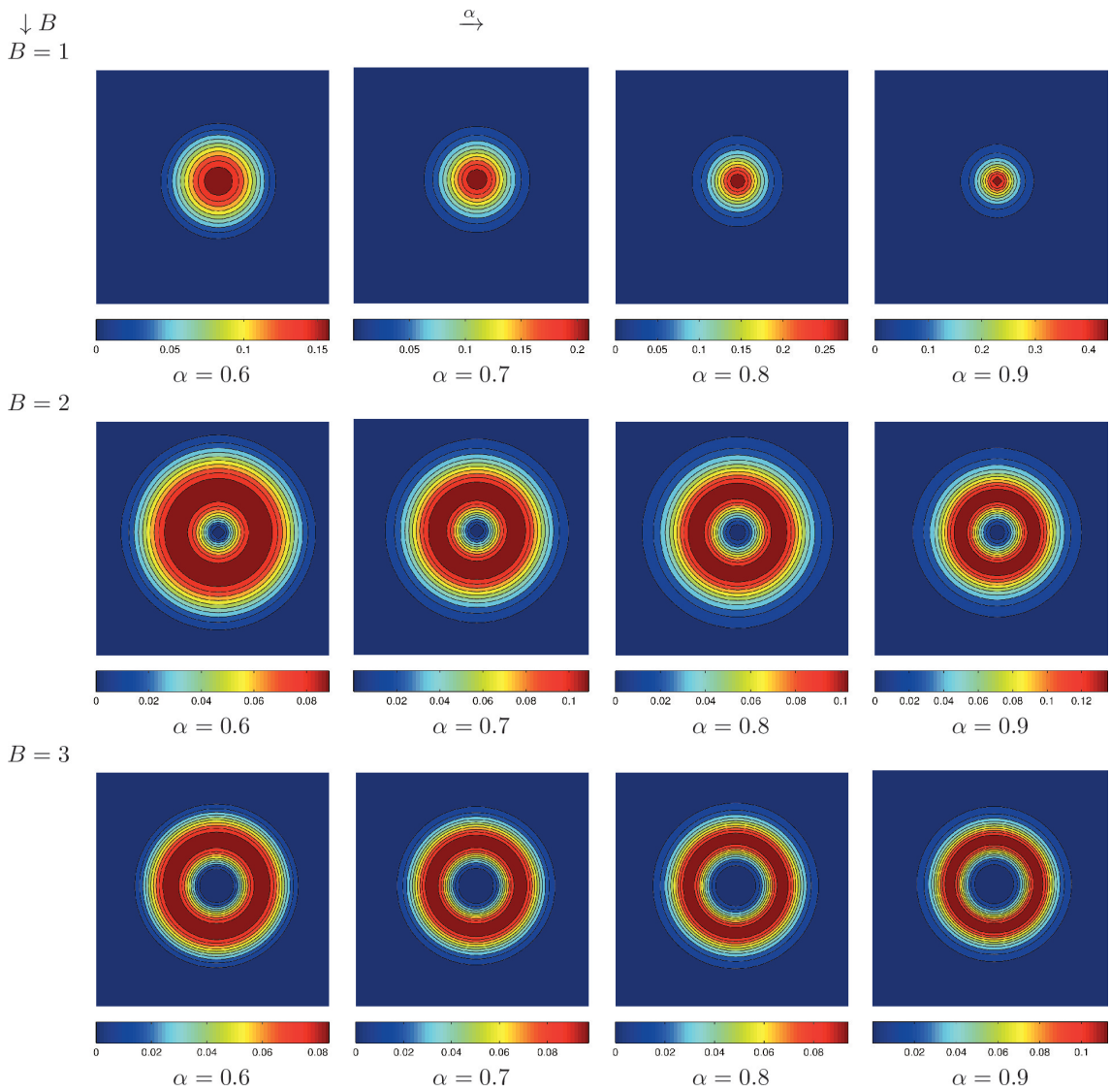

Figure 3.7: Energy density contour plots for baby Skyrmions with model parameter $\alpha = 0.6,\ 0.7,\ 0.8,\ 0.9$ and charges $B = 1 - 3$.

model [44], although the $\alpha = 0.6$ chain in particular appears more squashed. The chains observed at higher α values are quite different. However, comparisons could be drawn between the $\alpha = 0.9$ chain and the isospinning baby Skyrmions of Ref. [35] in which chains are also seen to break up.

3.4 Conclusions

We have developed a one-parameter family of baby Skyrme models that do not require a potential term to admit topological solitons. Starting with a general form for our models involving four parameters, we fixed three of these by specifying that our models should

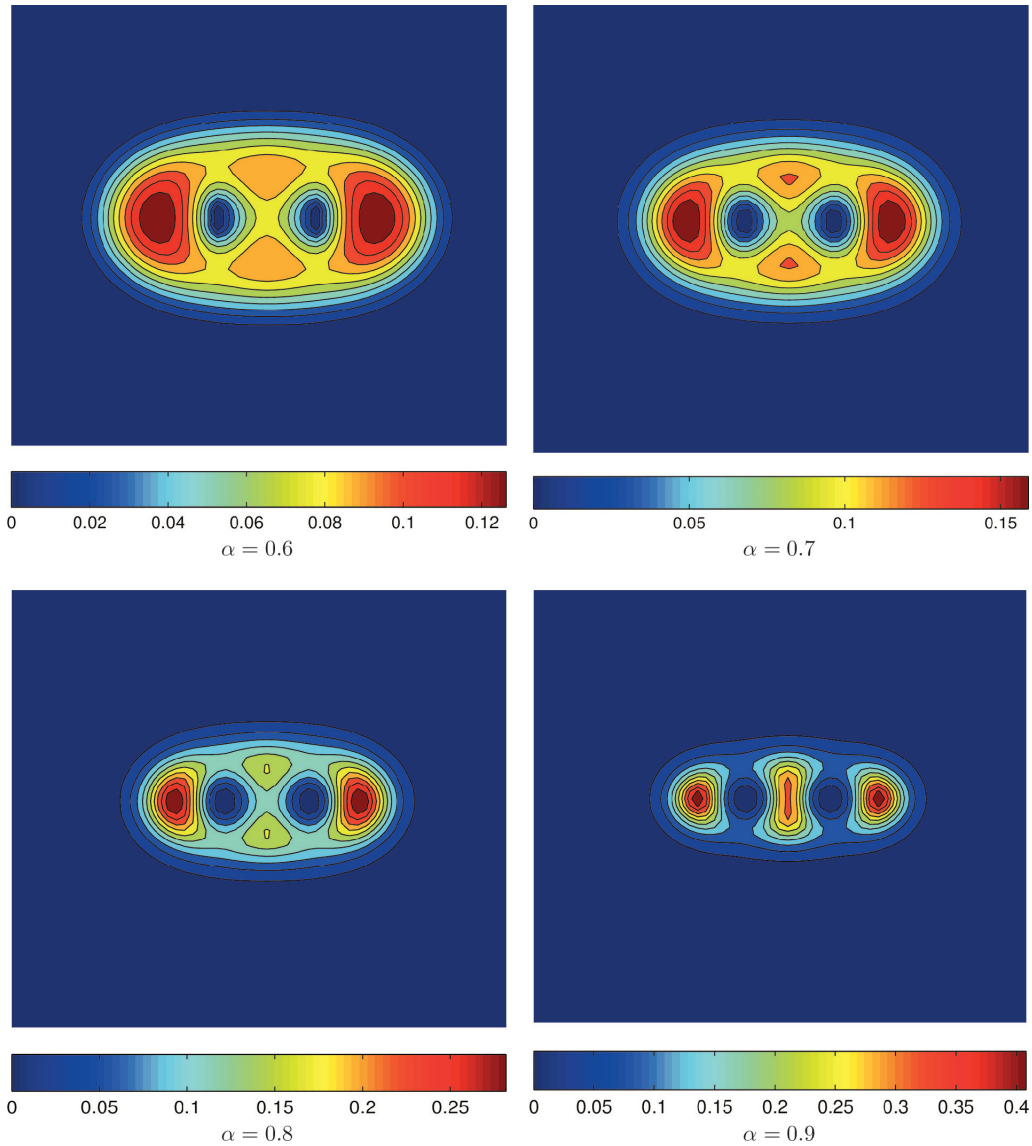

Figure 3.8: Contour plots of the energy density for $B = 3$ chain configurations. The value of α for each configuration is indicated underneath its plot.

satisfy the topological energy bound $E \geq 4\pi|B|$. Similarly to the Skyrme models described in Ref. [61], we found that at one end of our parameter range there is a model in which this bound can be saturated. This model is scale invariant, and exact solutions to the Bogomolny equations can be obtained for any topological charge. Furthermore, our choice of parameters ensures that all of our models satisfy the same virial theorem, $E_2 = E_4$, as the Skyrme model. In this way, we have designed a one-parameter family of baby Skyrme models without a potential whose scaling behaviour better matches the Skyrme model and which even includes a baby Skyrme model scaling exactly like the Skyrme model at the extreme of our parameter range where $\alpha = 0.5$.

Our investigation into the solitons of our models showed that their form greatly depends upon the choice of the parameter α. Solitons in the $\alpha = 0.5$ model are compactons. Both our numerical results for this model and linearisation arguments support this conclusion. Previous examples of compactons in baby Skyrme models [71, 51, 72] depend on the choice of potential term used, and typically occur for particular parameter values in a one-parameter family of potential functions. There is no potential term in our models but the choice of parameter is also important for the existence of compactons here.

Solitons in the models with $\alpha > 0.5$ were found to be less localised. We calculated solutions numerically for a selection of the models using three different methods. The energy of solutions to our models decreases as α increases, and higher-charge solutions are more tightly bound near the $\alpha = 0.5$ end of the parameter range. As we approach the extreme of the parameter range in which the energy bound can be saturated, the binding energy of solutions decreases to zero. The energy minimisers are axially symmetric solutions, even for topological charge three. However, we also observed other higher-charge configurations with greater energy, in particular $B = 3$ chain configurations. Chain solutions for $\alpha \in [0.6, 0.7]$ most closely resemble those observed in the old baby Skyrme model [44], while other chains have a very different appearance. In particular, as α increases our chain configurations begin to pull apart and become three almost separate solitons.

In this chapter we have provided an initial study of our new baby Skyrme models but there is still further work that could be done. In particular, we could investigate solitons of higher charges in our models to learn whether axially symmetric solutions would always be the minimal energy configurations. Another avenue for future work could be to include a potential term. Whilst the unique aspect of our models is that they do not require a potential term, it would be interesting to see what effect, if any, that different potentials would have on the solitons of the model. Following Ref. [63] and balancing the different terms with the potential would give rise to multi-parameter families of models which still obey a linear energy bound. The choice of potential has an important effect on the structure of solitons in the usual baby Skyrme model. Whether the same is true of our new models remains to be seen.

Chapter 4

Multi-vortex scattering

The Ginzburg-Landau model [74], also known as the Abelian-Higgs model, admits topological solitons called vortices. In condensed matter physics, the model is used to describe superconductors with the value taken by the coupling constant distinguishing between Type I and Type II superconductivity. The existence of vortices in this model was discovered by Abrikosov in 1957 in a study of the magnetic properties of Type II superconductors [4]. In two dimensions the vortices are particle-like, and in three dimensions they are strings. We will study the dynamics of vortices in (2+1)-dimensions and consider the gauged model which is comprised of the complex Higgs field and three gauge fields.

The behaviour of vortices differs between Type I and Type II superconductivity. In Ref. [75] the interaction energy between vortices was calculated, and numerical simulations were used to demonstrate that for values of the coupling constant describing Type I superconductors, two vortices attract each other, while for values describing Type II superconductors, two vortices repel each other. At the critical value of the coupling constant that separates Type I and II superconductivity, two vortices neither attract nor repel. A lower bound on the energy of vortices can be derived for any λ: for $\lambda \geq 1$ one can derive the bound $E \geq \pi N$, and since the energy is positive definite, for $\lambda < 1$ we have the bound $E \geq 0$. At critical coupling, the Bogomolny bound on the energy is saturated [10] and static vortex solutions can be obtained by solving a system of first order PDEs. We discuss this case in more detail in Sec. 4.1.

The scattering of two vortices has been studied both numerically and analytically by many authors. Two charge 1 vortices in a head-on collision will scatter at right angles, provided that the zeros of the Higgs field overlap [76, 77, 78, 79]. Numerical simulations

indicate that vortex scattering is approximately independent of the initial velocity v up to $v \approx 0.4c$ [76, 78]. After this, higher mode excitations become important and the kinetic energy loss from radiation becomes significant [76]. Ref. [78] also notes that for critically coupled vortices the scattering is approximately elastic until $v \approx 0.3c$. We will always take $c = 1$, unless stated otherwise.

Vortex dynamics has also been understood through the use of analytical approximations. For instance, the dynamics of slow-moving vortices is well-approximated by geodesic motion on the moduli space of static solutions of the Bogomolny equations, modulo gauge equivalence [80]. The moduli space approximation captures important features of the dynamics such as the right angle scattering of two vortices in a head-on collision. An alternative approximation was presented in Ref. [81], which proposes that the scattering of two vortices depends on the phase gradient of the Higgs field. For vortices at critical coupling, the authors discuss a self-force coming from the phase winding and depending on the velocity. They use this to explain vortex scattering in the absence of an intervortex force at critical coupling. Whilst the focus of this chapter is a numerical study of multivortex scattering, in the future we intend to compare our results to the predictions of analytical approximations.

Whilst the scattering of individual vortices is well-understood, to our knowledge there has been little investigation into the scattering of multi-vortex solutions in the Ginzburg-Landau model. In this chapter, we present the initial results of our investigations into such scattering processes. We carry out numerical simulations of the scattering of two multi-vortex rings, each comprised of between two and four vortices and find an unexpected variety of scattering outcomes. Our simulations indicate that there exist windows of initial velocity in which different scattering behaviours are observed. This invites a natural comparison with the kink scattering simulations discussed in Chapter 2, but we have not previously seen such behaviours observed for vortices.

We begin this chapter with a brief review of the gauged Ginzburg-Landau model. We discuss the construction of initial conditions for our scattering simulations, including the particular care taken to preserve our choice of gauge after boosting static vortices. The results of numerical simulations into the scattering of multi-vortex rings are presented in Sec. 4.3, and we present a preliminary analysis of the energy contributions from individual vortices after the collisions in Sec. 4.4. We end by summarising our results and discussing further work to be carried out for this project.

4.1 Vortices in the gauged Ginzburg-Landau model

We consider the gauged Ginzburg-Landau model, which is a gauge theory with gauge group $U(1)$. The complex scalar field $\phi(\mathbf{x}) = \phi(t, x, y)$ is coupled to an electromagnetic field with gauge potential $a_\mu(\mathbf{x}) = a_\mu(t, x, y)$, $\mu = 0, 1, 2$. The Lagrangian is

$$L = \int \left(-\frac{1}{4} f_{\mu\nu} f^{\mu\nu} + \frac{1}{2} \overline{D_\mu \phi} D^\mu \phi - \frac{\lambda}{8} (1 - \overline{\phi}\phi)^2 \right) \, \mathrm{d}^2 x, \tag{4.1}$$

where λ is a real parameter, $f_{\mu\nu}$ is the field tensor, given by

$$f_{\mu\nu} = \partial_\mu a_\nu - \partial_\nu a_\mu, \tag{4.2}$$

and $D_\mu \phi$ is the covariant derivative,

$$D_\mu \phi = \partial_\mu \phi - i a_\mu \phi. \tag{4.3}$$

To ensure finite energy, vortex solutions must satisfy $D_\mu \phi \to 0$ and $|\phi| \to 1$ as $|x| \to \infty$. The Lagrangian (4.1) is invariant under gauge transformations

$$\phi(\mathbf{x}) \mapsto e^{i\alpha(\mathbf{x})} \phi(\mathbf{x}), \quad a_\mu(\mathbf{x}) \mapsto a_\mu(\mathbf{x}) + \partial_\mu \alpha(\mathbf{x}). \tag{4.4}$$

The parameter λ distinguishes between Type I and Type II superconductivity. If $\lambda < 1$, then we model Type I superconductivity, and if $\lambda > 1$ then the model describes Type II superconductivity. The value $\lambda = 1$ separating the two regimes is known as critical coupling. As we will discuss shortly, the choice of λ also controls whether vortices in this model will attract or repel each other.

Since we are working in two dimensions, the field tensor $f_{\mu\nu}$ has three components: the magnetic field $B = f_{12}$, and the electric fields $e_1 = f_{01}$, and $e_2 = f_{02}$. The topological charge is an integer N giving the net number of vortices in a solution. It can be written in terms of the magnetic field as

$$N = \frac{1}{2\pi} \int B \, \mathrm{d}^2 x. \tag{4.5}$$

Before discussing vortex dynamics, we will first consider static solutions in this model. The potential energy is given by

$$V = \frac{1}{2} \int \left(B^2 + \overline{D_i \phi} D_i \phi + \frac{\lambda}{4} (1 - \overline{\phi}\phi)^2 \right) \, d^2 x. \tag{4.6}$$

In the case of critical coupling, $\lambda = 1$, there is a Bogomolny bound [10] on the energy. By completing the square, the integrand of (4.6) can be written as

$$\left(B \mp \frac{1}{2}(1-\overline{\phi}\phi)\right)^2 + (\overline{D_1\phi} \mp i\overline{D_2\phi})(D_1\phi \pm iD_2\phi) \pm B \mp i\left(\partial_1(\overline{\phi}D_2\phi) - \partial_2(\overline{\phi}D_1\phi)\right). \quad (4.7)$$

The last term in the expression (4.7) is a two-dimensional curl, and by applying Green's theorem we can write its integral as an integral over the circle at infinity S^1_∞,

$$i\int \left(\partial_1(\overline{\phi}D_2\phi) - \partial_2(\overline{\phi}D_1\phi)\right)\, \mathrm{d}^2x = i\int_{S^1_\infty} \overline{\phi}D_1\phi\, \mathrm{d}x \;+\; \overline{\phi}D_2\phi\, \mathrm{d}y. \quad (4.8)$$

Since vortex solutions have finite energy, we require that $D_i\phi \to 0$ and $|\phi| \to 1$ as $|x| \to \infty$, and hence this integral is zero. Further, using (4.5) to evaluate the integral of B as $2\pi N$, we find that the integral of (4.7) is

$$E = V = \frac{1}{2}\int \left(\left(B \mp \frac{1}{2}(1-\overline{\phi}\phi)\right)^2 + (\overline{D_1\phi} \mp i\overline{D_2\phi})(D_1\phi \pm iD_2\phi)\right) \mathrm{d}^2x \pm \pi N. \quad (4.9)$$

Since the integrand in (4.9) is non-negative, we can deduce that its integral is also non-negative, and thus find that $E \geq \pm\pi N$. It is clear that the energy (4.6) is positive, and so when $N > 0$ the plus sign gives the significant bound. Similarly, for $N < 0$ we take the minus sign. In general, we have the Bogomolny bound

$$E \geq \pi|N|, \quad (4.10)$$

which is saturated for solutions of the Bogomolny equations

$$\begin{aligned} D_1\phi \pm iD_2\phi &= 0, \\ B \mp \frac{1}{2}\left(1-\overline{\phi}\phi\right) &= 0. \end{aligned} \quad (4.11)$$

To obtain static vortices for any value of λ, we can exploit the circular symmetry of vortex solutions. This is easier if we work in polar coordinates r and θ. In these coordinates, we have the gauge fields

$$a_r = a_1\cos\theta + a_2\sin\theta, \quad a_\theta = -a_1 r\sin\theta + a_2 r\cos\theta, \quad (4.12)$$

and the field tensor becomes $f_{r\theta} = rf_{12}$. The potential energy in polar coordinates is given by

$$V = \frac{1}{2}\int_0^\infty\int_0^{2\pi}\left(\frac{1}{r^2}f_{r\theta}^2 + \overline{D_r\phi}D_r\phi + \frac{1}{r^2}\overline{D_\theta\phi}D_\theta\phi + \frac{\lambda}{4}(1-\overline{\phi}\phi)^2\right)\, r\,dr\,d\theta. \quad (4.13)$$

By taking into account the circular symmetry of vortex solutions, we determine that the fields must take the form $\phi(r,\theta) = \phi(r)e^{iN\theta}$, $a_r(r,\theta) = a_r(r)$, and $a_\theta(r,\theta) = a_\theta(r)$. We fix $a_r(r) = 0$ using an r-dependent gauge transformation. Substituting these expressions into (4.13), we arrive at the reduced energy

$$V = \pi \int_0^\infty \left(\frac{1}{r^2}\left(\frac{da_\theta}{dr}\right)^2 + \left(\frac{d\phi}{dr}\right)^2 + \frac{1}{r^2}(N-a_\theta)^2\phi^2 + \frac{\lambda}{4}\left(1-\phi^2\right)^2 \right) r\,dr, \tag{4.14}$$

for which the field equations are

$$\begin{aligned} \frac{d^2\phi}{dr^2} + \frac{1}{r}\frac{d\phi}{dr} - \frac{1}{r^2}(N-a_\theta)^2\phi + \frac{\lambda}{2}(1-\phi^2)\phi = 0, \\ \frac{d^2a_\theta}{dr^2} - \frac{1}{r}\frac{da_\theta}{dr} + (N-a_\theta)\phi^2 = 0. \end{aligned} \tag{4.15}$$

By the principle of symmetric criticality, solutions of (4.15) are also solutions of the equations of motion for (4.13). We solve (4.15) for the profile functions $\phi(r)$, $a_\theta(r)$, through the use of a finite difference method. The boundary conditions are $\phi(0) = 0$, $a_\theta(0) = 0$, $\phi(\infty) = 1$, and $a_\theta(\infty) = N$.

Fig. 4.1 displays the profile functions for charge (a) $N = 1$, and (b) $N = 2$ vortex solutions with parameter $\lambda = 1$, along with (c) the energy density for both vortex solutions, and (d) the magnetic field, which in this case is given by $B(r) = \frac{1}{r}\partial_r a_\theta$. We see from these plots that the vortices have a finite core size, outside of which they approach the vacuum exponentially. The energy density for an $N = 1$ vortex is a peak, whilst for $N = 2$ it is ring-like. This is more apparent in the 2D plots that we will consider later on, but can also be seen here in Fig. 4.1(c).

In Fig. 4.2, we plot the energy E/π against N for $\lambda = 0.5,\ 1.0,\ 1.5$. This illustrates the effect of the parameter λ on the vortex behaviour. Denote by E_1 the energy of a single vortex and by E_N the energy of N coincident vortices. An example of Type I superconductivity ($\lambda < 1$) is given by $\lambda = 0.5$ in Fig. 4.2. Here we see that $E_N < NE_1$. Thus the energy is reduced as vortices come together, and so they will attract in this regime. Conversely, for Type II superconductivity ($\lambda > 1$), which is represented by $\lambda = 1.5$ in Fig. 4.2, we have $E_N > NE_1$, and the vortices will repel one another. For critical coupling, $\lambda = 1$, the vortices saturate a Bogomolny bound, and the energy grows linearly with N since $E_N = NE_1$. In this case the vortices can be placed anywhere, and do not attract or repel.

To construct initial conditions for vortex scattering simulations, we will first need static

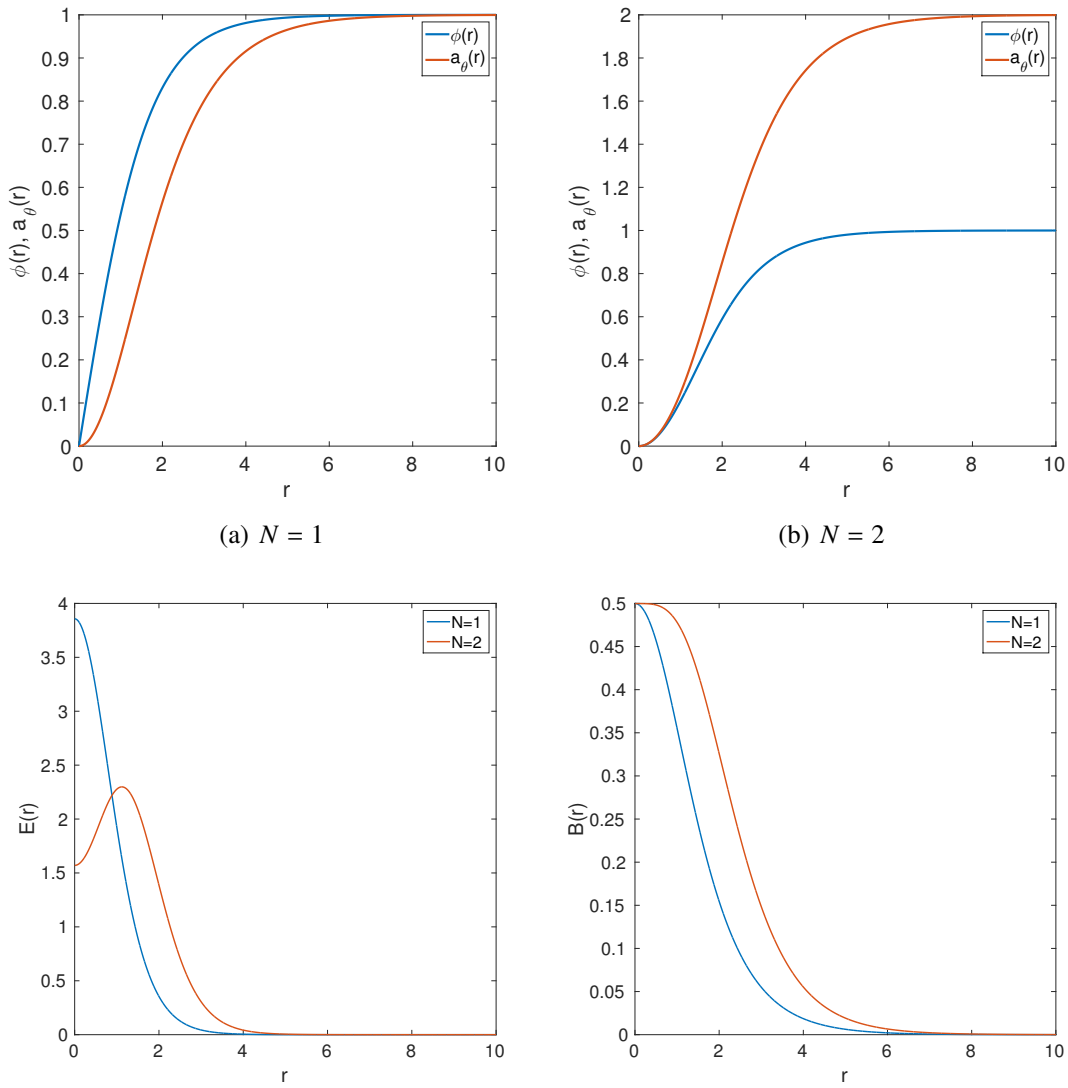

(a) $N = 1$ (b) $N = 2$

(c) $E(r)$ (d) $B(r)$

Figure 4.1: Profile functions for $\lambda = 1$ vortex solutions with (a) $N = 1$, (b) $N = 2$, and the associated (c) energy density $E(r)$, and (d) magnetic field $B(r)$.

vortex solutions on a 2D grid. We obtain such solutions by solving the gradient flow equations

$$\partial_0\phi = D_{ii}\phi + \frac{\lambda}{2}(1 - \overline{\phi}\phi)\phi,$$
$$\partial_0 a_i = -\epsilon_{ij}\partial_j B - \frac{i}{2}(\overline{\phi}D_i\phi - \phi\overline{D_i\phi}), \tag{4.16}$$

where ϵ_{ij} is given by $\epsilon_{12} = 1$, and $\epsilon_{21} = -1$, using a finite difference method. We typically work on a grid of size 601×601 with grid spacing $\Delta x = \Delta y = 0.1$, and timestep $\Delta t = 0.001$. The spatial derivatives are approximated with fourth order accuracy.

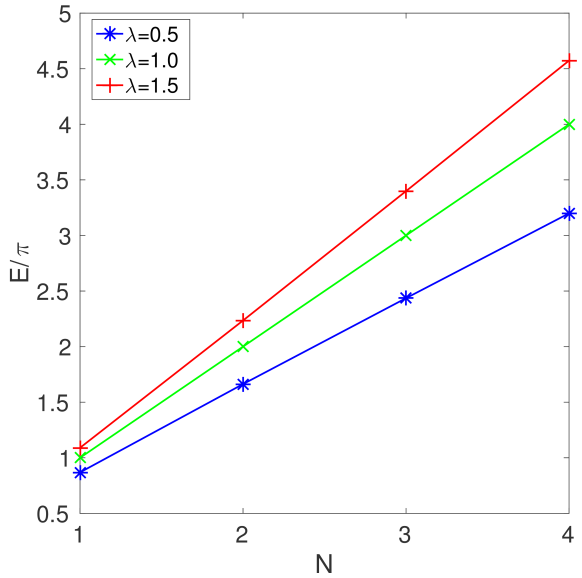

Figure 4.2: Energy of vortex profile functions for different values of λ and N.

Fig. 4.3 shows the energy density of vortex solutions obtained by this method for topological charge (a) $N = 1$ and (b) $N = 2$. The circular symmetry of each solution is evident in both contour plots. We see that for the solution of two coincident vortices given in Fig. 4.3, the energy density forms a ring. In later sections, we will refer to such solutions as *multi-vortex rings*, or *N-vortex rings*, where N is the topological charge of the solution.

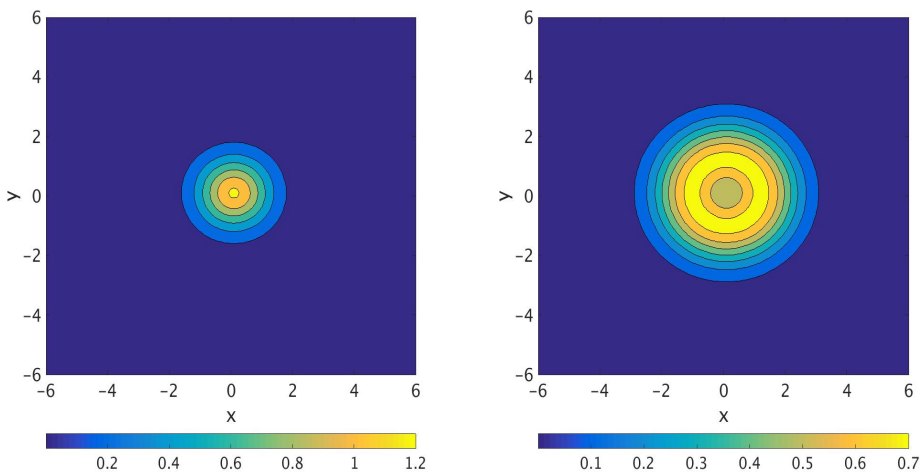

(a) $N = 1$ (b) $N = 2$

Figure 4.3: Contour plot of energy density for critically coupled vortex solutions with topological charge (a) $N = 1$, (b) $N = 2$.

4.2 Vortex dynamics

To simulate vortex scattering, we use the second-order dynamics. We evolve the vortices according to the equations

$$\begin{aligned} D_\mu D^\mu \phi - \frac{\lambda}{2}(1 - \overline{\phi}\phi)\phi &= 0, \\ \partial_\mu f^{\mu\nu} + \frac{i}{2}\left(\overline{\phi} D^\nu \phi - \phi \overline{D^\nu \phi}\right) &= 0, \end{aligned} \tag{4.17}$$

and choose to work in the temporal gauge $a_0 = 0$. Our numerical simulations use a leapfrog method with grid spacing $\Delta x = \Delta y = 0.1$, and timestep $\Delta t = 0.01$. The typical grid size used in our simulations is 601×601, though for some longer simulations we use 1001×1001 grids, and the finite difference approximations to the spatial derivatives are fourth order accurate.

To generate initial conditions for vortex scattering, we first boost a static solution to move at a given initial velocity v in the x-direction. This process also affects the gauge fields, and so we need to apply a gauge transformation after boosting to ensure that we remain in the temporal gauge. Under a Lorentz boost in the x-direction, our coordinates transform as

$$t \mapsto \tilde{t} = \gamma(t - vx), \qquad x \mapsto \tilde{x} = \gamma(x - vt), \qquad y \mapsto \tilde{y} = y, \tag{4.18}$$

where $\gamma = 1/(1 - v^2)$ is the Lorentz factor. We can write this as $\tilde{\mathbf{x}} = \Lambda \mathbf{x}$, where

$$\Lambda = \begin{pmatrix} \gamma & -\gamma v & 0 \\ -\gamma v & \gamma & 0 \\ 0 & 0 & 1 \end{pmatrix} \tag{4.19}$$

The Higgs field transforms as $\tilde{\phi}(\mathbf{x}) = \phi(\Lambda^{-1}\mathbf{x})$. Writing $\mathbf{a}(\mathbf{x}) = (a_0(\mathbf{x}), a_1(\mathbf{x}), a_2(\mathbf{x}))$, the gauge fields transform as $\tilde{\mathbf{a}}(\mathbf{x}) = \Lambda \mathbf{a}(\Lambda^{-1}\mathbf{x})$. Since we began in the temporal gauge, $a_0 = 0$, the individual gauge fields become

$$\tilde{a}_0(\mathbf{x}) = -\gamma v a_1(\Lambda^{-1}\mathbf{x}) \quad \tilde{a}_1(\mathbf{x}) = \gamma a_1(\Lambda^{-1}\mathbf{x}), \quad \tilde{a}_2(\mathbf{x}) = a_2(\Lambda^{-1}\mathbf{x}). \tag{4.20}$$

To transform back to the temporal gauge, we need to choose an $\alpha(t, x, y)$ so that

$$0 = \tilde{a}_0 + \partial_t \alpha. \tag{4.21}$$

Combining this with (4.20) gives $\partial_t \alpha = v\tilde{a}_1$. We can approximate α by

$$\alpha(t, x, y) = \alpha(0, x, y) + t\partial_t \alpha(0, x, y) + ..., \tag{4.22}$$

and we take

$$\alpha(t, x, y) \approx vt\tilde{a}_1(0, x, y). \tag{4.23}$$

We use this approximation of $\alpha(t, x, y)$ to gauge transform $\tilde{\phi}$, $\tilde{a}_1$, and $\tilde{a}_2$ according to (4.4) and return to the temporal gauge.

To create our initial conditions for vortex scattering, we combine two vortex solutions which have been boosted towards each other. We achieve this by using the Abriksov ansatz. This states that, given a vortex solution $(\phi(\mathbf{x}), a_\mu(\mathbf{x}))$, we can obtain an approximate multi-vortex solution as

$$\hat{\phi}(\mathbf{x}) = \prod_i \phi(\mathbf{x} - \mathbf{x_i}), \quad \hat{a}_\mu(\mathbf{x}) = \sum_i a_\mu(\mathbf{x} - \mathbf{x_i}), \tag{4.24}$$

where the $\{x_i\}$ are the positions of the vortex centres. This ansatz is very accurate if all vortices are widely separated.

An example of an initial condition for our multi-vortex scattering simulations is given in Fig. 4.4. It shows the energy density of a solution of two 2-vortex rings which have been boosted towards each other with initial velocity $v = 0.3$. This configuration is at critical coupling ($\lambda = 1$), as are all of the scattering simulations carried out in this chapter.

One way to summarise the information obtained from our scattering simulations is to track the positions of the vortices as the minima (which are also the zeros) of the Higgs field ϕ. For a simulation with N vortices, there are N minima to find. To begin, we find the smallest value of ϕ on our grid, and use the location of this as an initial approximation to the position of the first vortex, $\mathbf{x_1}$. Initial guesses for the other $N - 1$ vortex positions are taken to be the locations of the other smallest ϕ values on the grid. To accept one of these values as an initial guess, the value of ϕ must be less than a given tolerance and further than a given number of grid points away from any previous $\mathbf{x_i}$ guesses. This is to ensure that we do not double-count the same point unnecessarily and that we do not choose a value that is too large to be close to a zero. If we cannot find a value satisfying these conditions, then we repeat a previous guess. Since we know that our simulations begin with two well separated vortex rings, we expect to begin with only two distinct position values. To refine our initial guesses

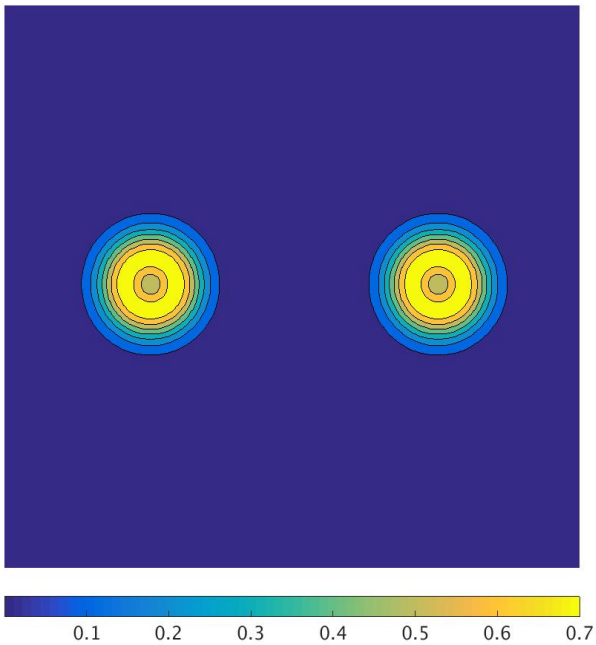

Figure 4.4: Contour plot of the energy density of two 2-vortex rings boosted towards each other with initial velocity $v = 0.3$ at critical coupling.

for the vortex positions, we use the amoeba minimisation routine (as given in Ref. [73]) to find a more accurate position of the minimum. We calculate any values needed in between the grid points by polynomial interpolation.

After the initial step, we calculate the vortex positions every 100 timesteps. Now when seeking the minimal values of ϕ on the grid, we search in a box around the previous location of that vortex. Again we require that the value of ϕ must be less than a given tolerance and further than a given number of grid points away from any previous $\mathbf{x_i}$ guesses to be accepted. If we cannot find such a point, then the initial guess is taken to be the same as the closest accepted guess to the previous location of the vortex in question. The greatest challenge in tracking vortex positions during our simulations is handling the steps in which vortices come together to form rings, or when rings separate into multiple individual vortices. Some trial and error was used to find appropriate values of the tolerance and allowed distances from other points in order to accurately track the positions of all vortices at such times.

As an example, we use this position tracking method to track the scattering of two critically coupled vortices initially located at $(\pm 4, \pm b)$, where the impact parameter b is the initial vertical distance between the two vortices. We boost the vortices towards each other

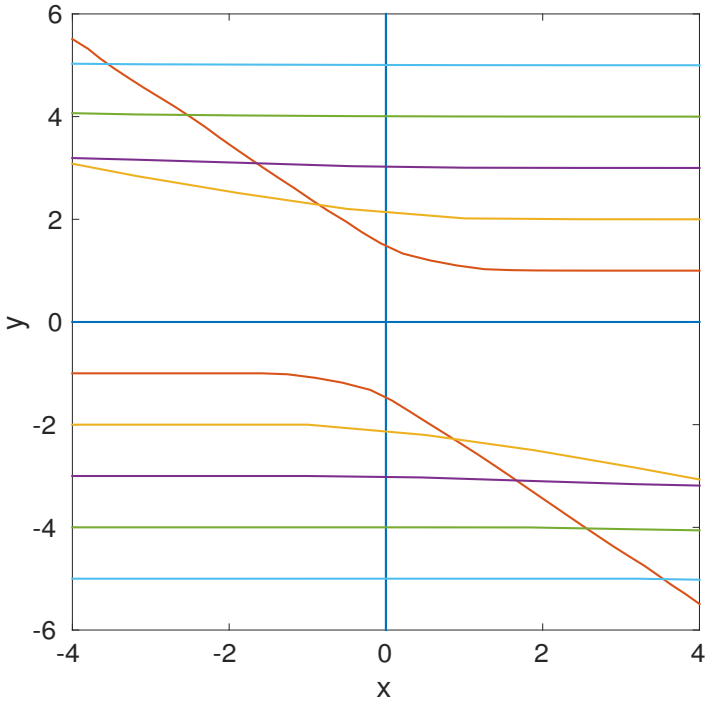

Figure 4.5: Scattering of two vortices at critical coupling with initial velocity $v = 0.3$ and initial positions $(\pm 4, \pm b)$ for impact parameter $b = 0,\ 2,\ 4,\ 6,\ 8,\ 10$.

with initial velocity $v = 0.3$ for a range of different b values, and plot the vortex positions throughout the scattering process in Fig. 4.5. We recover the same information as was found in previous studies of vortex scattering (e.g. Refs. [76, 77, 78, 79]). In a head on collision ($b = 0$), the vortices scatter at right angles. As b increases, the vortex trajectories bend away from each other less and less, until eventually they are no longer affected by one another.

Before discussing the results of our simulations, we would like to note a current issue with our dynamics code. When boosting a single 2-vortex ring to move at an initial velocity v, we observe that after a significant period of time the ring will break up into two individual vortices, which we would not expect to happen. The time that it takes for the ring to break up is dependent on the initial velocity, with the ring remaining intact for a longer period of time for smaller initial velocities, but travelling a further distance for greater initial velocities. For any v, the ring does not split up until after the time at which the vortex rings collide in our multi-vortex scattering simulations. However this does occur at a time within the length of our simulations and so our results may be compromised. We are currently working to address this issue, but for now we present the results of our preliminary simulations which form the first investigation carried out into collisions of multi-vortex rings.

4.3 Multi-vortex scattering

We now present the results of our numerical investigations into the scattering of multi-vortex rings. All of our simulations concern vortices at critical coupling and begin with two well-separated N-vortex rings which are boosted towards each other with an initial velocity v. In this section, we describe the scattering behaviours that we observe for $N = 2$, and $N = 3$ vortex rings.

We first consider the scattering of two 2-vortex rings. In our simulations, we have observed two distinct scattering behaviours. The first, and most common, outcome of the scattering of two 2-vortex rings is shown in Fig. 4.6. This displays snapshots of the energy density during the scattering of two 2-vortex rings with initial velocity $v = 0.3$. Fig. 4.6(a) shows the initial configuration of two well-separated 2-vortex rings. In Fig. 4.6(b), we see the rings collide and form a chain-like structure in which the two vortices at the centre form a ring and the other two vortices are situated on either side. Figs. 4.6(c) and (d) show that the central pair of vortices scatter through each other at right angles and escape along the y-axis, whilst the outer vortices continue to approach each other along the x-axis. In Fig. 4.6(e), we see the latter pair of vortices collide and form a ring. They scatter at right angles and emerge along the y-axis, as seen in Fig. 4.6(f). However, they do not escape to infinity like the other pair of vortices, but instead form a bound state in which they repeatedly scatter through each other at right angles.

In Fig. 4.7, we track the vortex positions during scattering processes for some values of the initial velocity v where this scattering outcome is observed. Since the vortices are most frequently located on either the x- or y-axis, we plot the x and y coordinates of the vortex positions against time. This enables us to clearly see the times at which each pair of vortices scatters through each other as the points at which one coordinate becomes zero and the other non-zero. The plots on the left show the x-coordinate of the vortex position, which is initially $x = \pm 6$, and the plots on the right show the y-coordinate, which begins as $y = 0$ for all vortices. The values of the initial velocity considered are $v = 0.2$ in Figs. 4.7(a) and (b), $v = 0.4$ in Figs. 4.7(c) and (d), and $v = 0.6$ in Figs. 4.7(e) and (f).

Initially there are two pairs of coincident vortex zeros approaching the origin. As they near the origin, each pair splits up into a faster moving zero and a slower one. The faster vortices from the positive and negative x-directions meet at $x = 0$ and from then on their

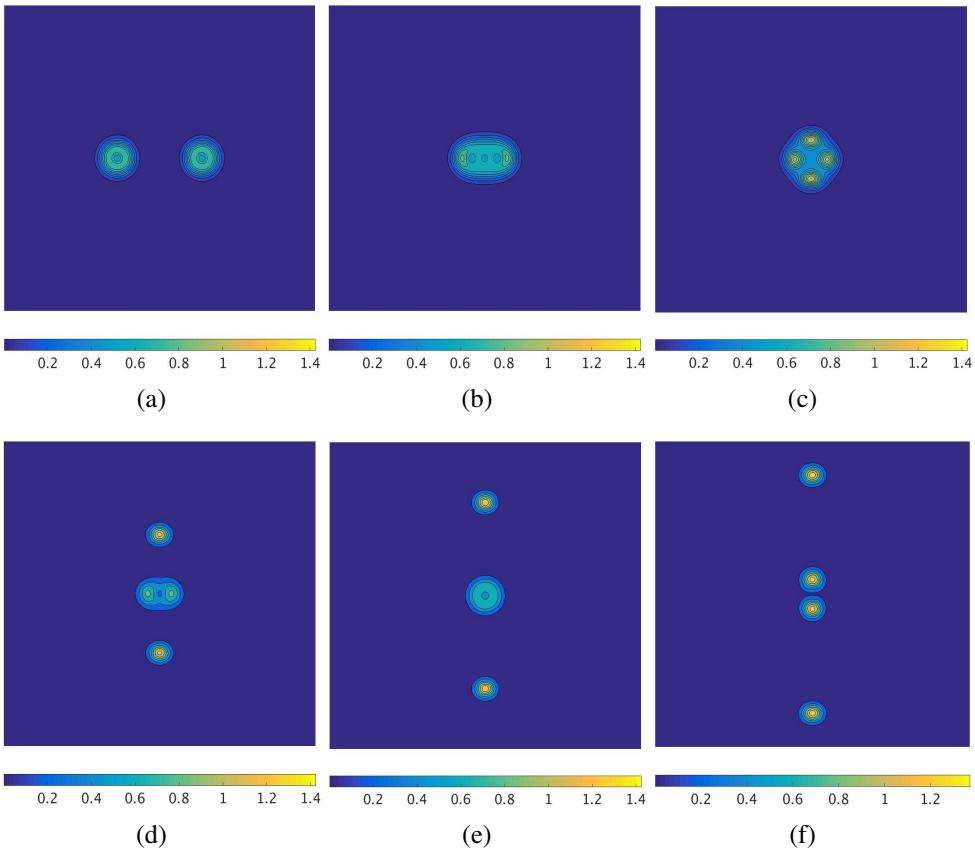

Figure 4.6: Snapshots of the energy density during the scattering of two 2-vortex rings at critical coupling with initial velocity $v = 0.3$. The rings collide, and one pair of vortices scatters at right angles to escape along the y-axis. The other vortex pair forms a bound state at the origin in which the vortices repeatedly scatter through each other at right angles.

x-coordinate value remains zero. Comparing this with the y-coordinate plots, we see that at this time the y-coordinate of these two vortices becomes non-zero as they travel apart along the y-axis, eventually moving at a constant speed. The other pair of vortices meet at the origin at a later time than the first pair, and they travel a small distance apart along the y-axis. After some time, the two vortices travel back to $y = 0$ and emerge along the x-axis again. This is a pattern that will repeat itself, as we see in the plots for the greater initial velocities. As the initial velocity increases, the intervals between each scattering of the bound state vortices decreases. Note that whilst in the figures we plot the positions for $t \in [0, 250]$ the simulations have been run over a longer period of time. We do not see the bound state vortices scatter a second time in Figs. 4.7(a) and (b), which correspond to $v = 0.2$, but we can confirm this does occur at a later time.

For certain values of the initial velocity, we observe a different scattering outcome. As in the previous case, a pair of faster moving vortices will scatter at right angles and escape to

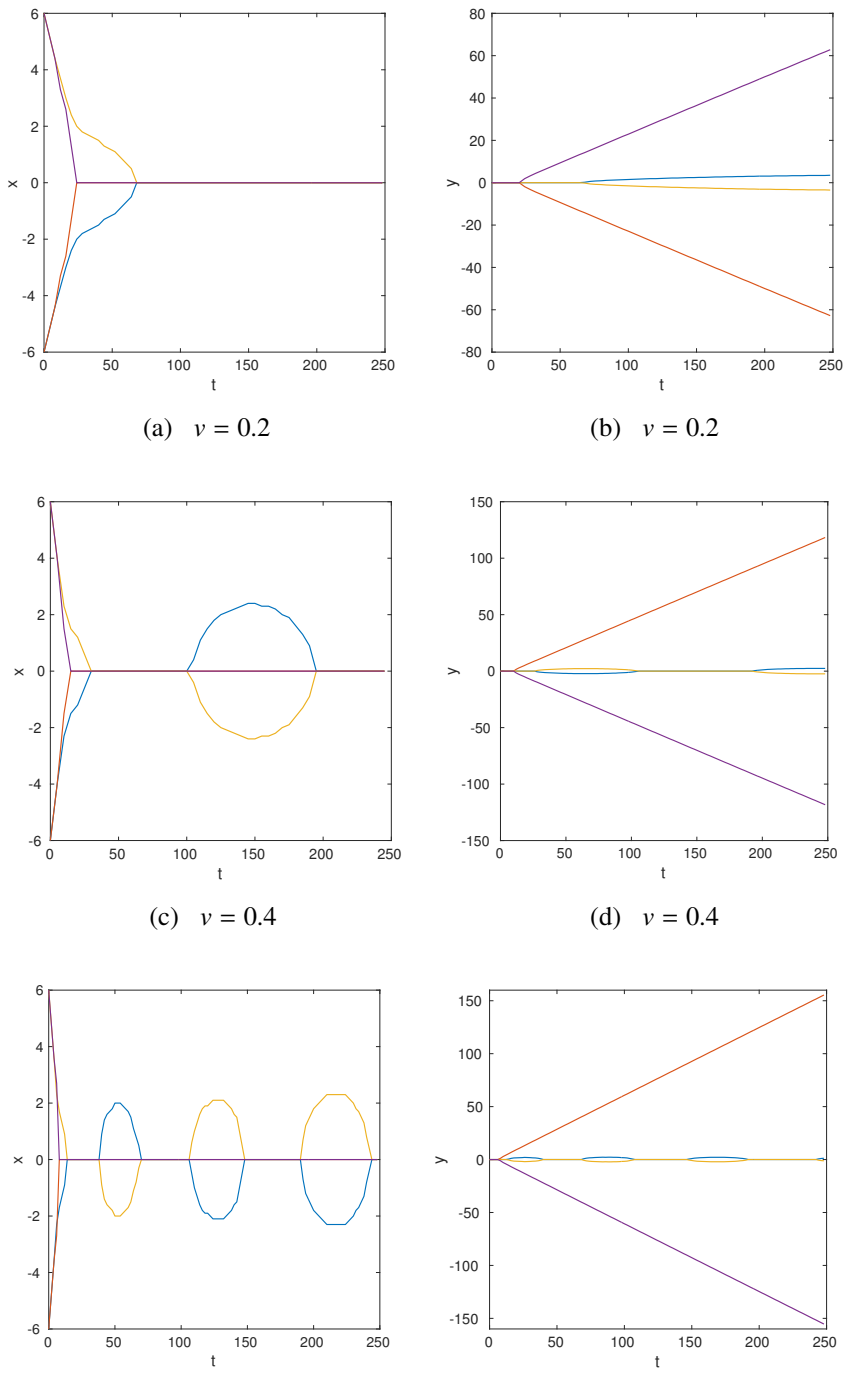

(a) $v = 0.2$ (b) $v = 0.2$

(c) $v = 0.4$ (d) $v = 0.4$

(e) $v = 0.6$ (f) $v = 0.6$

Figure 4.7: Vortex positions during the scattering of two 2-vortex rings at critical coupling. We plot x- and y-coordinates of the vortex position against time for different initial velocity v. (a) x-coordinate with $v = 0.2$. (b) y-coordinate with $v = 0.2$. (c) x-coordinate with $v = 0.4$. (d) y-coordinate with $v = 0.4$. (e) x-coordinate with $v = 0.6$. (f) y-coordinate with $v = 0.6$.

infinity along the y-axis. However the remaining pair of vortices do not form a bound state, but can escape along either the x- or y-axis after scattering through each other a number of

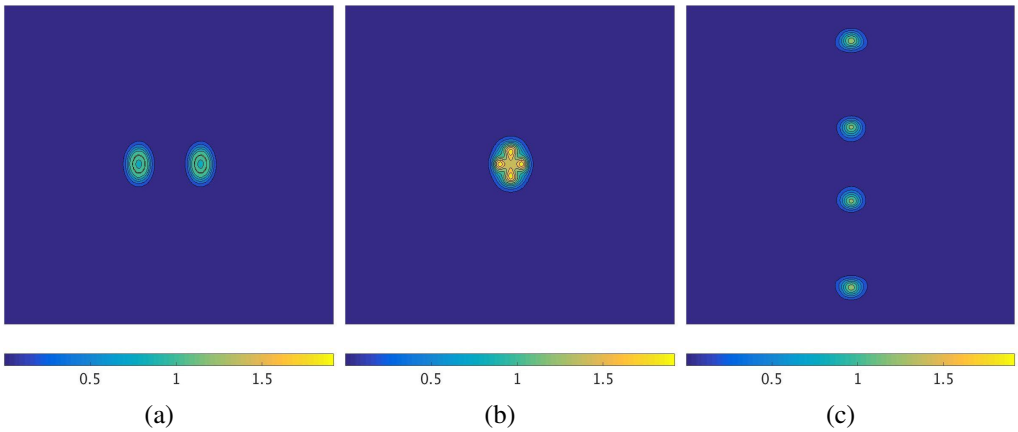

Figure 4.8: Snapshots of the energy density during the scattering of two 2-vortex rings at critical coupling with initial velocity $v = 0.75$. The rings collide and one pair of vortices scatters at right angles. The two other vortices then scatter through each other and escape to infinity along the y-axis.

times. An example of this behaviour is illustrated in Fig. 4.8 which corresponds to initial velocity $v = 0.75$. Fig. 4.8(a) shows the initial configuration of two well-separated 2-vortex rings that have been boosted towards each other. The rings travel at high speed and are clearly distorted by Lorentz contraction. We see the rings collide in Fig. 4.8(b) and the inner pair of vortices scatter at right angles. Shortly after, the remaining pair of vortices also scatter at right angles. In Fig. 4.8(c), we see both pairs of vortices escape to infinity along the y-axis. Note that the first pair of vortices to scatter move faster than the other two.

Fig. 4.9 displays the vortex positions as a function of time for three different values of the initial velocity corresponding to three different ways in which the central pair of vortices can escape. Figs. 4.9(a) and (b) present the x- and y-coordinates of the vortex position for initial velocity $v = 0.64$, respectively. In this case, the central pair of vortices scatter through each other for the first time around $t \approx 12$ and emerge along the y-axis. They scatter through each other again at $t \approx 42$ and then for a final time at $t \approx 113$, after which they escape along the y-axis. In Figs. 4.9(c) and (d), we display the scattering outcome when $v = 0.65$. In this case the vortices scatter through each other first at $t \approx 11$ and again at $t \approx 44$, after which they escape to infinity along the x-axis. Figs. 4.9(e) and (f) correspond to initial velocity $v = 0.75$. Here the central pair of vortices only scatter through each other once and immediately after this they escape along the y-axis.

For greater initial velocities, the two scattering outcomes are found to occur in certain windows of the initial velocity. This is somewhat unexpected, as we have not seen such

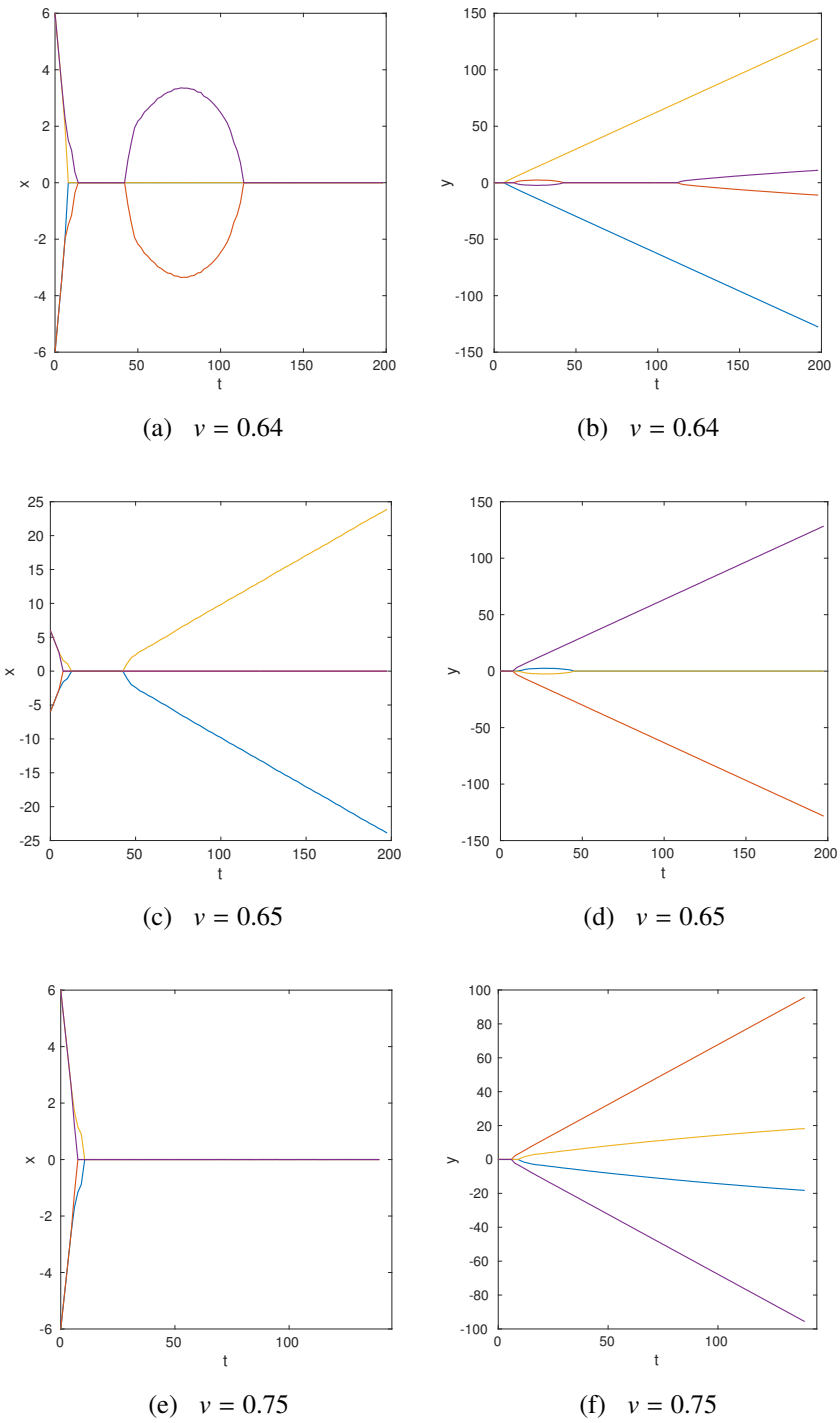

(a) $v = 0.64$ (b) $v = 0.64$

(c) $v = 0.65$ (d) $v = 0.65$

(e) $v = 0.75$ (f) $v = 0.75$

Figure 4.9: Vortex positions during the scattering of two 2-vortex rings at critical coupling. We plot x- and y-coordinates of the vortex position against time for different initial velocity v. (a) x-coordinate with $v = 0.64$. (b) y-coordinate with $v = 0.64$. (c) x-coordinate with $v = 0.65$. (d) y-coordinate with $v = 0.65$. (e) x-coordinate with $v = 0.75$. (f) y-coordinate with $v = 0.75$.

windows emerge in previous simulations of vortex scattering. However they are common in kink-antikink scattering, where they have been observed in models such as the ϕ^4 model

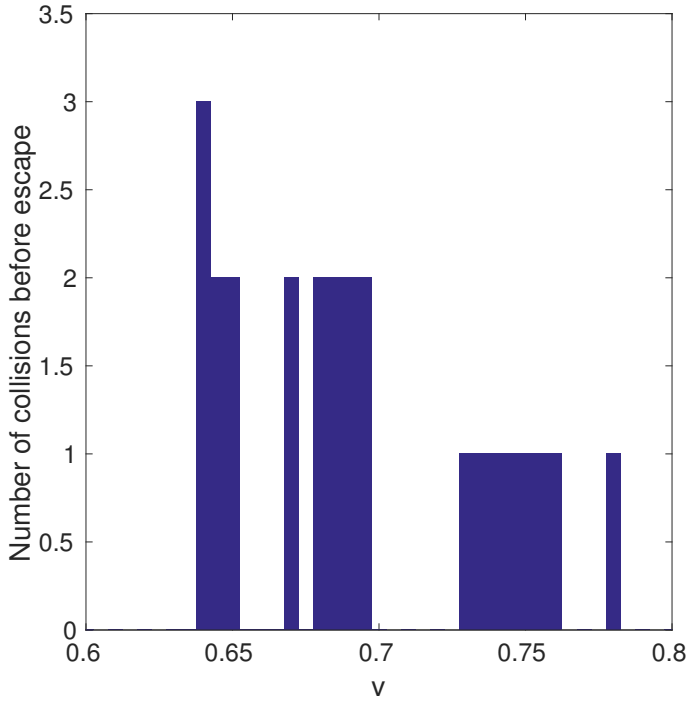

Figure 4.10: Number of collisions prior to the escape of the central two vortices during the scattering of two 2-vortex rings against initial velocity $v \in [0.6, 0.8]$. Where the vortices do not escape but instead form a bound state, we count zero collisions to make the distinction between windows of the different scattering behaviours clearer, though in fact they collide repeatedly and never escape.

[12, 13, 17], and the ϕ^6 model [20, 21]. In Fig. 4.10 we provide an overview of the different windows of scattering behaviour for initial velocity $v \in [0.6, 0.8]$. We plot the number of collisions before the central two vortices escape along an axis against the initial velocity. To clearly visualise the distinction between the two different scattering outcomes, we count zero collisions if the vortices form a bound state, even though in this case the vortices will collide and scatter through each other repeatedly for the duration of the simulation. For vortices in windows of the escape behaviour, an odd number of collisions indicates that they escape along the y-axis, and an even number that they escape along the x-axis. The number of collisions is conserved in each window of the escape behaviour. So far we have found that the number of collisions in the escape windows decreases with initial velocity. The longest window is the 1-collision window for $v \in [0.73, 0.76]$. In this plot we have only tested in increments of 0.01 due to the length of time required for each simulation. With more time we would refine the resolution to find out if there are any smaller windows around the edges of these existing ones.

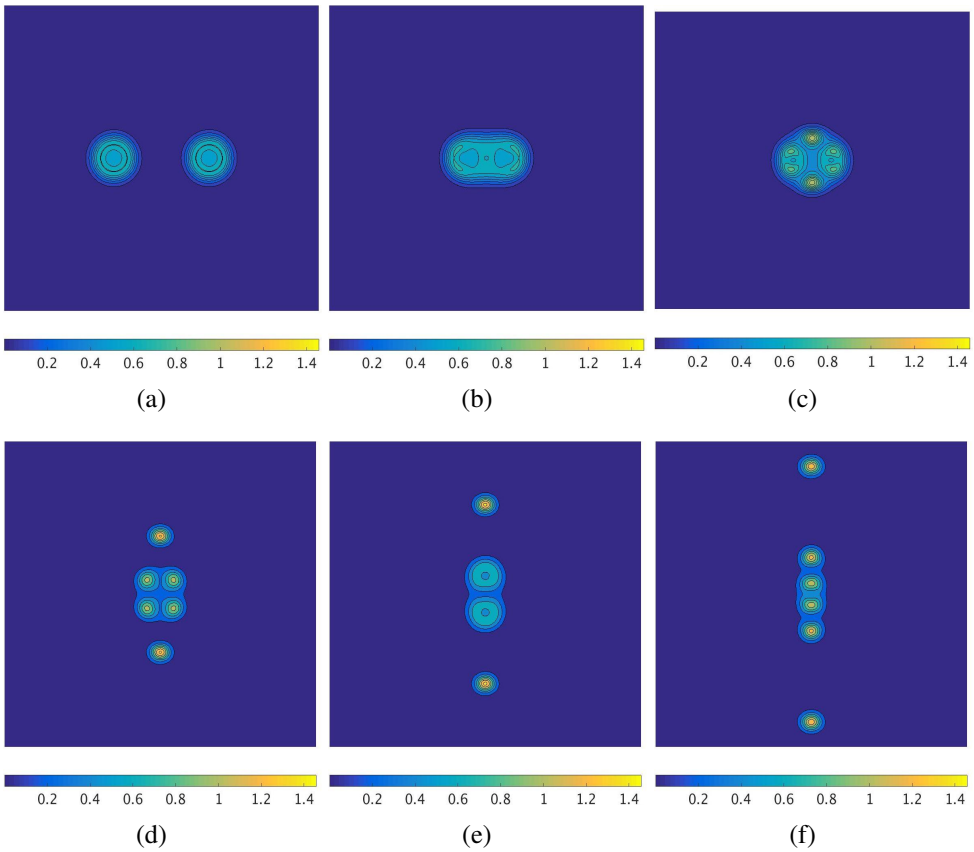

Figure 4.11: Snapshots of the energy density during the scattering of two 3-vortex rings at critical coupling with initial velocity $v = 0.3$. The rings collide and one pair of vortices scatters at right angles and escapes along the y-axis. The remaining four vortices split into pairs and scatter at right angles. They emerge on the y-axis, where the outer two vortices separate to infinity and the inner pair form a bound state, repeatedly scattering through each other at right angles.

We also simulate head-on collisions of two 3-vortex rings and find two types of scattering outcome depending on the initial velocity. In Fig. 4.11 we display snapshots of the energy density during the scattering of two 3-vortex rings with initial velocity $v = 0.3$. The initial configuration of two well separated 3-vortex rings is shown in Fig. 4.11(a), and we see in Figs. 4.11(b) and (c) that two vortices, one taken from each ring, scatter at right angles through the origin and escape to infinity along the y-axis. The remaining vortices in each ring separate into four individual vortices, as seen in Fig. 4.11(d). The upper and lower pairs of vortices each scatter at right angles and emerge along the y-axis. This process is seen in Figs. 4.11(e) and (f). The outer vortices escape to infinity along the y-axis, though more slowly than the first pair to scatter. The inner two vortices form a bound state similar to that observed in the case of two 2-vortex rings.

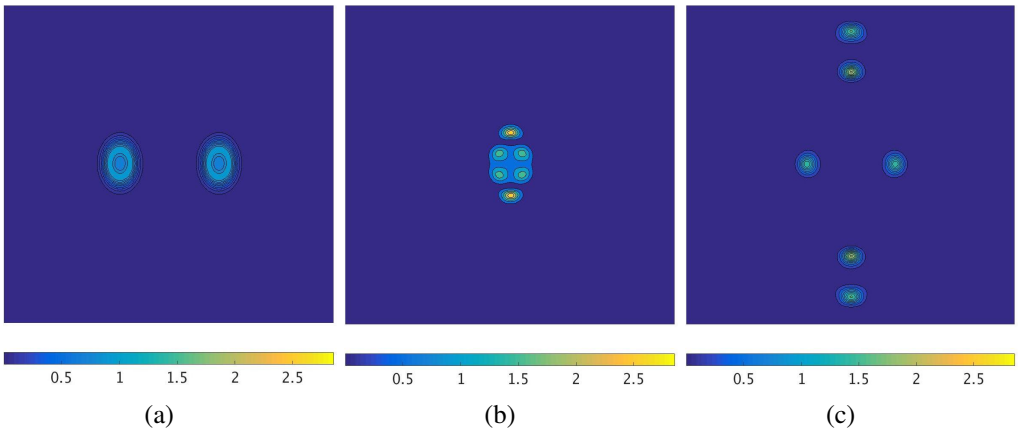

Figure 4.12: Snapshots of the energy density during the scattering of two 3-vortex rings at critical coupling with initial velocity $v = 0.7$. The rings collide and one pair of vortices scatters at right angles. The other four vortices then scatter through each other. Two of them escape to infinity along the y-axis and the other two escape along the x-axis.

The other scattering outcome is illustrated in Fig. 4.12, which shows snapshots of the energy density during the scattering of two 3-vortex rings with initial velocity $v = 0.7$. The initial configuration of two well-separated rings is seen in Fig. 4.12(a). As before, when the two rings collide, a pair of vortices scatters at right angles and escapes along the y-axis. Fig. 4.12(b) presents the vortex configuration shortly after this, where two vortices are travelling apart along the y-axis and four vortices remain at the centre. When the remaining four vortices collide and scatter, two escape along the y-axis and two escape along the x-axis. All of the vortices travel to infinity after their collisions, as shown in Fig. 4.12(c). The first two vortices to scatter travel much faster than the other four.

In Fig. 4.13 we plot the x- and y-coordinates of the vortex positions against time during the scattering of two 3-vortex rings with initial velocity $v = 0.3,\ 0.6,\ 0.71$. Initially the vortices are located at $(\pm 6, 0)$ with three zeros at each point. One vortex breaks away from each ring, and these scatter through each other and emerge along the y-axis. The remaining vortex zeros from each ring slowly move apart in the y-direction whilst approaching $x = 0$. In Fig. 4.13, this corresponds to the x-coordinates approaching zero (two from the positive x-direction and two from the negative x-direction), and the y-coordinates moving away from zero (two in the positive y-direction and two in the negative y-direction). One zero in the positive x-axis corresponds to a zero moving in the positive y-direction, and the other to a zero moving in the negative y-direction. The same is true of the zeros in the negative x-axis. When the x-coordinates reach $x = 0$, the two pairs of vortices (one pair with positive y and

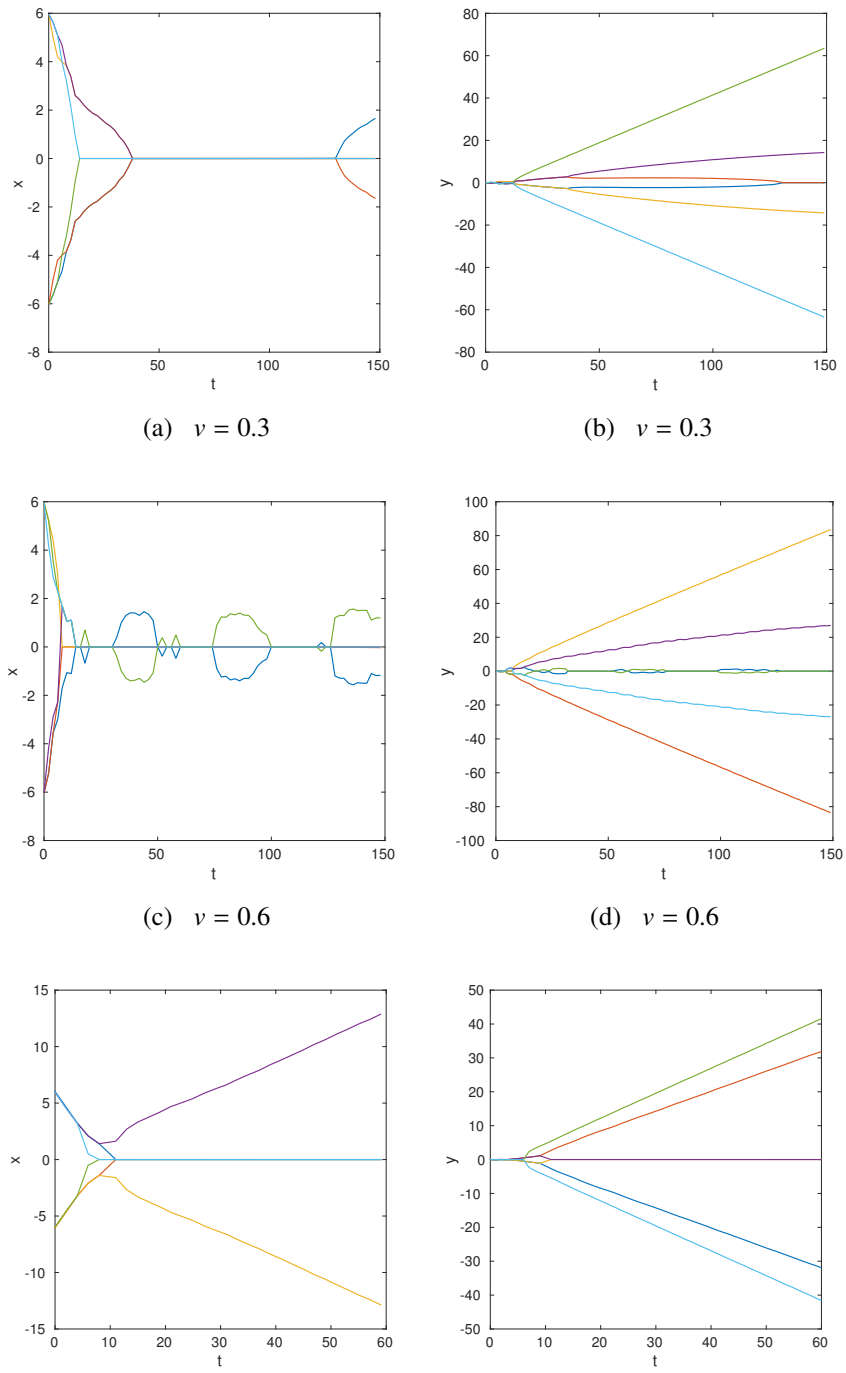

(a) $v = 0.3$ (b) $v = 0.3$

(c) $v = 0.6$ (d) $v = 0.6$

(e) $v = 0.71$ (f) $v = 0.71$

Figure 4.13: Vortex positions during the scattering of two 3-vortex rings at critical coupling. We plot x- and y-coordinates of the vortex positions against time for different initial velocity v. (a) x-coordinate with $v = 0.3$. (b) y-coordinate with $v = 0.3$. (c) x-coordinate with $v = 0.6$. (d) y-coordinate with $v = 0.6$. (e) x-coordinate with $v = 0.71$. (f) y-coordinate with $v = 0.71$.

one with negative y) scatter through each other. This is seen as each pair of coincident y-coordinates separating into two distinct lines. The outer two of these vortices escape slowly

along the y-axis, and in Figs. 4.13(a), (b) and (c), (d) the remaining pair of vortices form a bound state, repeatedly scattering through each other. As initial velocity v increases, the interval between each collision of the bound pair of vortices decreases. For $v = 0.6$, several collisions of the bound state vortices are visible in the figures, though for $v = 0.3$ we only see two. We can confirm that when the simulation is run for a longer time than that shown in these figures, it is clear that a bound state has been formed. Figs. 4.13(e), (f) correspond to initial velocity $v = 0.71$, where the two remaining vortices do not form a bound state, but instead escape along the x-axis.

4.4 Velocity of the escaping vortices

One aspect of the scattering of multivortex rings that we can measure is the velocity v_{out} of any escaping pairs of vortices. In this section we will use this information to approximate different contributions to the energy of the multivortex system.

Table 4.1 provides outgoing velocity data for multivortex scattering simulations with a total number of four or six vortices and for a range of initial velocities v_{in}. The solutions with topological charge $N = 4$ correspond to the scattering of two 2-vortex rings, and topological charge $N = 6$ corresponds to the scattering of two 3-vortex rings. Recall that in both cases, when the rings collide a pair of vortices escapes along the y-axis. The outgoing velocity v_{out} given in Table 4.1 is that of these vortices. Any vortices which escape later during the simulations travel more slowly.

To analyse the contribution to the energy of this escaping pair of vortices, we will approximate the kinetic energy of the system. First we consider the case of two 2-vortex rings. We assume that all of the incoming kinetic energy is transferred to the first outgoing pair of vortices, with none left to the remaining two vortices. This is a reasonable approximation to make since the remaining two vortices move much more slowly, regardless of whether they escape along an axis or form a bound state. To approximate the kinetic energy of the system, we first use a classical approximation. Let M denote the mass of a single vortex. Then we approximate the kinetic energy as

$$\frac{1}{2}\left(4Mv_{\text{in}}^2\right) = \frac{1}{2}\left(2Mv_{\text{out}}^2\right). \tag{4.25}$$

Table 4.1: Outgoing velocity v_{out} of escaping pairs of vortices after the scattering of two $(N/2)$-vortex rings with initial velocity v_{in} and $N = 4, 6$. The given velocity is that of the first pair of vortices to escape during the simulation.

	v_{out}	
v_{in}	$N = 4$	$N = 6$
0.05	0.06	0.07
0.1	0.13	0.16
0.15	0.20	0.24
0.2	0.27	0.31
0.25	0.33	0.39
0.3	0.39	0.45
0.35	0.44	0.50
0.4	0.49	0.53
0.45	0.54	0.56
0.5	0.58	0.57
0.55	0.61	0.57
0.6	0.64	0.56
0.65	0.66	0.53
0.7	0.69	0.52

Solving this for the outgoing velocity in terms of v_{in} gives

$$v_{\text{out}} = \sqrt{2} v_{\text{in}}. \tag{4.26}$$

This approximation should work well for small values of v_{in}, but for greater initial velocities we should perform a relativistic calculation. In this case our assumption that all of the incoming kinetic energy goes to the first outgoing pair of vortices implies that

$$4M\gamma_{\text{in}} = 2M\gamma_{\text{out}} + 2M, \tag{4.27}$$

where $\gamma_{\text{in/out}} = 1/\sqrt{1 - v_{\text{in/out}}^2}$. We can solve (4.27) for v_{out} in terms of v_{in}. A comparison of these two approximations with the velocity data from Table 4.1 is given in Fig. 4.14(a). We see that the first two points for each approximation agree very well with each other and also with the measured data. As v_{in} increases, the approximations become less accurate, with the relativistic approximation better than the classical one, as we would expect.

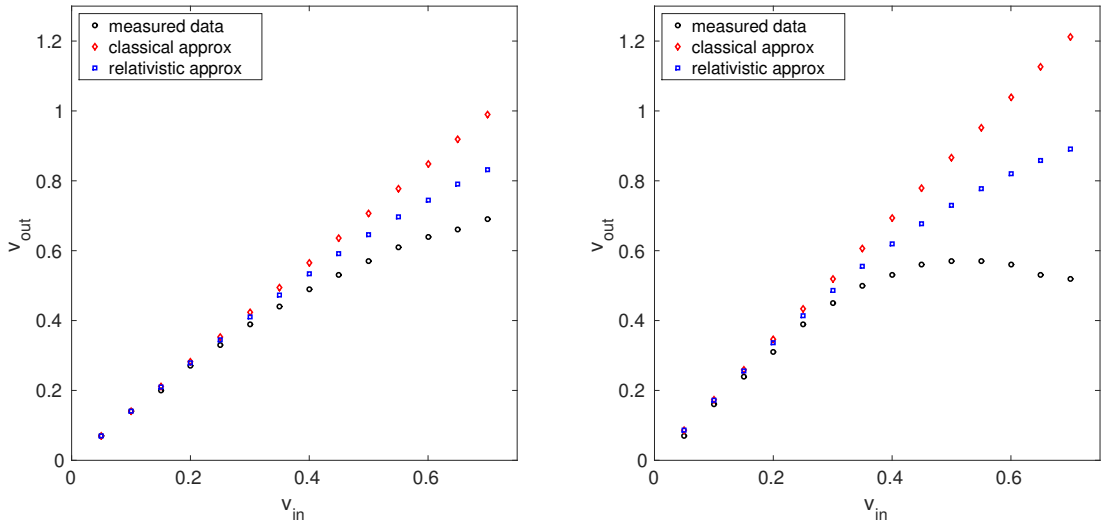

(a) $N = 4$ (b) $N = 6$

Figure 4.14: A comparison of our two energy approximations for (a) two 2-vortex rings, and (b) two 3-vortex rings, with the measured data from Table 4.1. Outgoing velocity v_{out} is plotted against incoming velocity v_{in} for the real data as black circles, for the classical approximation as red diamonds and for the relativistic approximation as blue squares.

Applying the same analysis to the outgoing velocity data for the $N = 6$ vortices, we assume that all of the incoming kinetic energy goes to the first escaping pair of vortices with none left in the bound state at the middle or any other pair of escaping vortices. First, we use a classical approximation, for which the kinetic energy is

$$\frac{1}{2}\left(6Mv_{\text{in}}^2\right) = \frac{1}{2}\left(2Mv_{\text{out}}^2\right). \tag{4.28}$$

This gives the outgoing velocity in terms of the initial velocity as

$$v_{\text{out}} = \sqrt{3}v_{\text{in}}. \tag{4.29}$$

For the second approximation, we perform a relativistic calculation. Then assuming that all of the incoming kinetic energy goes to the outgoing pair of vortices, we have

$$6M\gamma_{\text{in}} = 2M\gamma_{\text{out}} + 4M, \tag{4.30}$$

which we can solve for v_{out} in terms of v_{in}. In Fig. 4.14(b), we compare the results of our two approximations for $N = 6$ with the data from Table 4.1. As for the $N = 4$ vortices, we see that the approximations agree quite well with the measured data for low initial velocities, but become increasingly worse as the initial velocity increases. Both approximations for

the $N = 6$ system are less successful than the corresponding approximations for $N = 4$. However this is to be expected as in this calculation we have ignored four vortices, and thus four energy contributions, whereas we only ignored two for $N = 4$. Fig. 4.14(b) also confirms that the relativistic approximation is better than the classical approximation for any initial velocity.

In these approximations we have excluded information which is important, particularly for larger initial velocities. Of course there is an energy contribution from any bound state or slowly escaping vortices. Given that our approximations work well for small v_{in}, it is reasonable to ignore their contributions during low speed collisions, but for greater initial velocity they should be taken into account. A first step to extend our analysis is to include these energy contributions. For any escaping vortices, we can measure their velocity and add their kinetic energy to our approximations. To capture the energy of a bound state, we will calculate the energy in a box at the centre of the grid and add this to our approximations. Since the bound state vortices remain at the centre of the grid as they repeatedly scatter through each other, taking the energy in a large enough box should give the energy of this bound state.

From our simulations of the scattering process, we have also noticed what seems to be some radial vibration excited in the vortices after the collision. To fully understand the energy contributions, our ultimate goal is to analyse the vibrational modes and factor this in to our approximation. We would adjust (4.27) to include this information as

$$4M\gamma_{\text{in}} = 2M_1\gamma_{\text{out}} + 2M_2, \tag{4.31}$$

where $M_{1,2} = M + E_{\text{vib}1,2}$, the sum of the single vortex mass and the vibrational energy associated to the vortex.

4.5 Conclusions

We have carried out numerical simulations of the scattering of multi-vortex rings in the Ginzburg-Landau model. We began with a review of the model and its vortex solutions. Static solutions were obtained numerically and we boosted these solutions to obtain moving vortices, whilst taking care to preserve our choice of gauge. To produce initial configurations for our scattering simulations, we combined boosted vortex solutions using the Abrikosov

ansatz. We implemented a method for tracking the positions of vortices and used this to recreate well-known results for the scattering of two vortices with different impact parameters.

First we studied the head-on collision of two 2-vortex rings at critical coupling. We carried out numerical simulations for a range of different initial velocities v and found two different scattering outcomes. In both cases, when the vortex rings collide a pair of vortices scatters at right angles and escapes along the y-axis, but the behaviour of the remaining vortex pair changes with v. For most initial velocities, the vortex pair at the centre forms a bound state in which the vortices repeatedly scatter through each other at right angles. The interval between each collision of the vortices decreases with increasing v. The other possible scattering outcome is that the vortex pair escape to infinity along the x- or y-axis after a number of collisions. These vortices will move much more slowly than the first pair of escaping vortices.

At higher velocities, the two scattering outcomes for the remaining vortex pair appeared in alternating windows of initial velocity. For the escape behaviour, the number of collisions prior to the vortices escaping along an axis was conserved in each window. We have not seen such windows appear in vortex scattering simulations before, however they are a common feature of kink-antikink scattering and were even observed in Chapter 2 of this thesis, where we studied kink scattering in the presence of false vacua. In kink-antikink scattering, the kink and antikink will either annihilate or reflect off each other and travel apart to infinity. In windows where the kinks collide and separate to infinity, there are a number of collisions, or "bounces", counted before they escape, and this number is found to be conserved in each window. For multi-vortex scattering, the "bounce" number could be compared to the number of collisions before the two vortices escape along the x- or y- axis.

We also considered a head-on collision of two 3-vortex rings. Some features of these scattering processes were similar to those observed for 2-vortex rings. When the rings collide, two vortices scatter at right angles and escape along the y-axis, just as was the case for 2-vortex rings. The remaining four vortices split into two pairs, which scatter and emerge along the y-axis. Two of these vortices then escape to infinity and the remaining pair can either form a bound state similar to that observed in 2-vortex ring scattering, or escape along the x-axis after a number of collisions.

To analyse the results of our simulations, we measured the velocity of the first escaping

pair of vortices. We compared the measured velocity data to the predictions of a classical and a relativistic approximation to the kinetic energy, where we assumed that all of the incoming kinetic energy was transferred to this escaping pair of vortices. As we would expect, the relativistic approximation was more successful, although both approximations became less accurate as the initial velocity increased. We intend to extend this analysis to include approximations to the energy of the other vortices and to account for any energy from radial vibration of the vortices.

This chapter concerns work in progress and there are still further ideas that we wish to pursue. Firstly, with more time we would improve our vortex scattering code, as discussed in Sec. 4.2. We would also carry out simulations with greater resolution to confirm the existence of further windows of the escape behaviour. Eventually we intend to compare our numerical results to the predictions of the moduli space approximation. There is a conjecture that the vortices should remain rings [82] and so far our numerical simulations contradict this. Further developments to the project could be to consider N-vortex rings for larger N, and to vary the impact parameter in our simulations. Our work so far has only concerned vortices at critical coupling, so it would also be interesting to consider Type I and Type II vortex ring scattering.

Chapter 5

Vortices and impurities

In the previous chapter, we discussed the scattering of multi-vortex rings in the Ginzburg-Landau model of superconductivity. This chapter concerns vortex dynamics in a different setting. We investigate the scattering of vortices in the presence of magnetic impurities. Our aim is to provide an initial numerical study of such scattering processes for different choices of impurity. Previous studies of vortices in the presence of magnetic impurities have concentrated on the case of critical coupling. We carry out numerical simulations for critically coupled vortices, but also consider other values of the coupling constant λ.

The study of vortices in the presence of impurities has attracted interest in recent years. A notable example is the work of Tong and Wong in Ref. [83] concerning BPS vortices in the presence of electric and magnetic impurities. They argued that there still exists a moduli space of solitons after the addition of electric and magnetic impurities, and discussed the manner in which the moduli space dynamics is affected by each type of impurity. Ref. [83] has motivated several studies of vortices in product Abelian gauge theories which can be related to vortices in the presence of magnetic impurities. For example, existence theorems for solutions of vortices and anti-vortices in such models have been proven [84], and similar ideas have been explored in an Abelian Chern-Simons-Higgs model [85].

We have been particularly motivated by Ref. [86], in which the authors investigated the dynamics of vortices at critical coupling with magnetic impurities. They obtained solutions in flat space by numerically solving the Bogomolny equation for localised, axially symmetric impurities, and their numerics suggested the existence of a moduli space of vortex solutions. They also discussed vortices in hyperbolic space, where they calculated exact solutions and moduli space metrics for a delta function impurity. We will extend their results

for localised axially symmetric impurities in flat space by carrying out numerical simulations of the full field equations. This enables us to consider vortices away from critical coupling and to numerically simulate vortex dynamics.

As yet, there has not been a comprehensive numerical study of the scattering of vortices with magnetic impurities. In the previous chapter we summarised the results of numerical investigations into the scattering of two vortices in the Ginzburg-Landau model, such as those found in Refs. [76, 77, 78, 81]. In particular, these studies have explored the relationship between the scattering angle and impact parameter and any dependence of the scattering behaviour on the initial velocity given to the vortices. We carry out similar calculations for vortices scattering with magnetic impurities.

The chapter begins with an introduction to vortices in the presence of magnetic impurities. We discuss the Bogomolny bound satisfied by vortices at critical coupling and obtain vacuum solutions for different values of the coupling constant λ and for different impurities. The energy of static vortex solutions in the presence of magnetic impurities can be evaluated, and we find that away from critical coupling the impurity can either attract or repel the vortex depending on the value of the coupling constant λ and the impurity parameters. We carry out numerical simulations of the scattering of vortices at critical coupling with magnetic impurities and analyse our findings. Finally we summarise the results of the chapter and note opportunities for further work.

5.1 Vortices with magnetic impurities

We consider the deformation of the action (4.1) that was proposed in Ref. [83] to include magnetic impurities,

$$L = \int \left(-\frac{1}{4} f_{\mu\nu} f^{\mu\nu} + \frac{1}{2} \overline{D_\mu \phi} D^\mu \phi - \frac{\lambda}{8} (1 + \sigma - |\phi|^2)^2 + \frac{1}{2} \sigma B \right) d^2 x, \tag{5.1}$$

where σ is a fixed, static source term for the magnetic field $B = f_{12}$. We restrict our attention to localised, axially symmetric impurities of the form $\sigma(x, y) = ce^{-d(x^2+y^2)}$, where $c, d \in \mathbb{R}$, and $d > 0$.

We begin by obtaining vacuum solutions in this model. The potential energy for vortices in the presence of magnetic impurities is given by

$$V = \frac{1}{2} \int \left(B^2 + \overline{D_i \phi} D_i \phi + \frac{\lambda}{4} (1 + \sigma - |\phi|^2)^2 - \sigma B \right) d^2 x. \tag{5.2}$$

At critical coupling, it is again possible to obtain a Bogomolny bound on the energy. We first complete the square on the integrand of (5.2), to find

$$\left(B - \frac{1}{2}(1 + \sigma - \overline{\phi}\phi)\right)^2 + \overline{(D_1\phi + iD_2\phi)}(D_1\phi + iD_2\phi) + B - i\left(\partial_1(\overline{\phi}D_2\phi) - \partial_2(\overline{\phi}D_1\phi)\right). \tag{5.3}$$

As before, the final term above integrates to zero. Using this fact in combination with the expression for the topological charge (4.5) we see that

$$E = V = \frac{1}{2}\int\left(\left(B - \frac{1}{2}(1 + \sigma - \overline{\phi}\phi)\right)^2 + \overline{(D_1\phi + iD_2\phi)}(D_1\phi + iD_2\phi)\right)\mathrm{d}^2x + \pi N, \tag{5.4}$$

leading us to the Bogomolny bound

$$E \geq \pi N. \tag{5.5}$$

This is saturated for solutions of the Bogomolny equations

$$\begin{aligned} D_1\phi + iD_2\phi &= 0, \\ B - \frac{1}{2}\left(1 + \sigma - \overline{\phi}\phi\right) &= 0. \end{aligned} \tag{5.6}$$

Note that this is the same bound satisfied by vortices in the original model (4.6), and the only difference in the equations is the additional σ in the second Bogomolny equation.

We can derive a lower bound on the energy when $\lambda \neq 1$ in a similar way. We rewrite the integrand of (5.2) as

$$\begin{aligned} \left(B - \frac{1}{2}(1 + \sigma - \overline{\phi}\phi)\right)^2 + \overline{(D_1\phi + iD_2\phi)}(D_1\phi + iD_2\phi) + B - i\left(\partial_1(\overline{\phi}D_2\phi) - \partial_2(\overline{\phi}D_1\phi)\right) \\ + \frac{\lambda - 1}{4}\left(1 + \sigma - \overline{\phi}\phi\right)^2. \end{aligned} \tag{5.7}$$

Integrating this produces the same result as before, but with one additional term. The energy is bounded from below by

$$E \geq \pi N + \frac{\lambda - 1}{8}\int\left(1 + \sigma - \overline{\phi}\phi\right)^2 \mathrm{d}^2x. \tag{5.8}$$

When $\lambda \geq 1$, the additional term is non-negative, and we have the bound (5.5) which is saturated at critical coupling. For the more general bound (5.8) to be meaningful, we must argue that $\int(1+\sigma-\overline{\phi}\phi)^2\,\mathrm{d}^2x$ is bounded. This is true as long as σ and ϕ are non-singular and

decay sufficiently quickly at infinity. We consider impurities of the form $\sigma(x, y) = ce^{-d(x^2+y^2)}$, which all decay very fast, and considering the asymptotics for ϕ shows that it also decays fast enough. We will also discuss the limit in which σ approaches a delta function. In this case, a square of a delta function is introduced into the Lagrangian (5.1), which is not defined. However, as noted in Ref. [86], it does make sense to substitute a delta function for σ in the equations of motion, and we can consider this to be a limit of impurities for which the energy is well-defined.

5.1.1 Symmetric solutions

We first study the effect of the impurity on the vacuum configuration. To simplify the problem of solving for vacuum solutions, we assume circular symmetry. As in the previous section, we convert to polar coordinates $r,\ \theta$, and fix the radial gauge $a_r = 0$. Then we have $\phi(r, \theta) = \phi(r)e^{iN\theta}$, and $a_\theta(r, \theta) = a_\theta(r)$, and will solve for the real profile functions $\phi(r)$ and $a_\theta(r)$. For fields of this form, the energy (5.2) becomes

$$V = \pi \int \left(\phi'^2 + \frac{a_\theta'^2}{r^2} + \frac{(N - a_\theta)^2}{r^2}\phi^2 + \frac{\lambda}{4}(1 + \sigma - \phi^2)^2 - \frac{\sigma}{r}a_\theta' \right) r\, dr. \tag{5.9}$$

To calculate $\phi(r)$ and $a_\theta(r)$, we solve the reduced field equations

$$\begin{aligned} \phi'' + \frac{\phi'}{r} - \frac{(N - a_\theta)^2}{r^2}\phi + \frac{\lambda}{2}(1 + \sigma - \phi^2)\phi &= 0, \\ a_\theta'' - \frac{a_\theta'}{r} - \frac{r}{2}\sigma' + (N - a_\theta)\phi^2 &= 0, \end{aligned} \tag{5.10}$$

via a finite difference method similar to that discussed in Chapter 3, subject to the boundary conditions $\phi'(0) = 0$, $a_\theta(0) = 0$, $\phi(\infty) = 1$, $a_\theta(\infty) = N$. We consider impurities of the form $\sigma(r) = ce^{-dr^2}$, where $c, d \in \mathbb{R}$, and $d > 0$.

In Fig. 5.1 we display the profile functions $\phi(r)$, $a_\theta(r)$, the energy density $E(r)$, and the magnetic field $B(r)$ for vacuum solutions in the presence of three different magnetic impurities: $\sigma(r) = 4e^{-r^2}$ in solid lines, $\sigma(r) = -4e^{-r^2}$ in dashed lines, and $\sigma(r) = -8e^{-2r^2}$ in dotted lines. Solutions for $\lambda = 0.5$ are shown in blue and those for $\lambda = 1.5$ are shown in red. Though the profile functions were calculated over $r \in [0, 20]$, to highlight the more interesting features of the solutions we only display the ranges $r \in [0, 5]$ for the profile functions and $r \in [0, 3]$ for the energy density and magnetic field. We see that the effect of the impurity is localised, with the fields taking their usual vacuum values away from the impurity. In Ref. [86] it was noted that for vortices at critical coupling $\phi(0) \to 0$ as

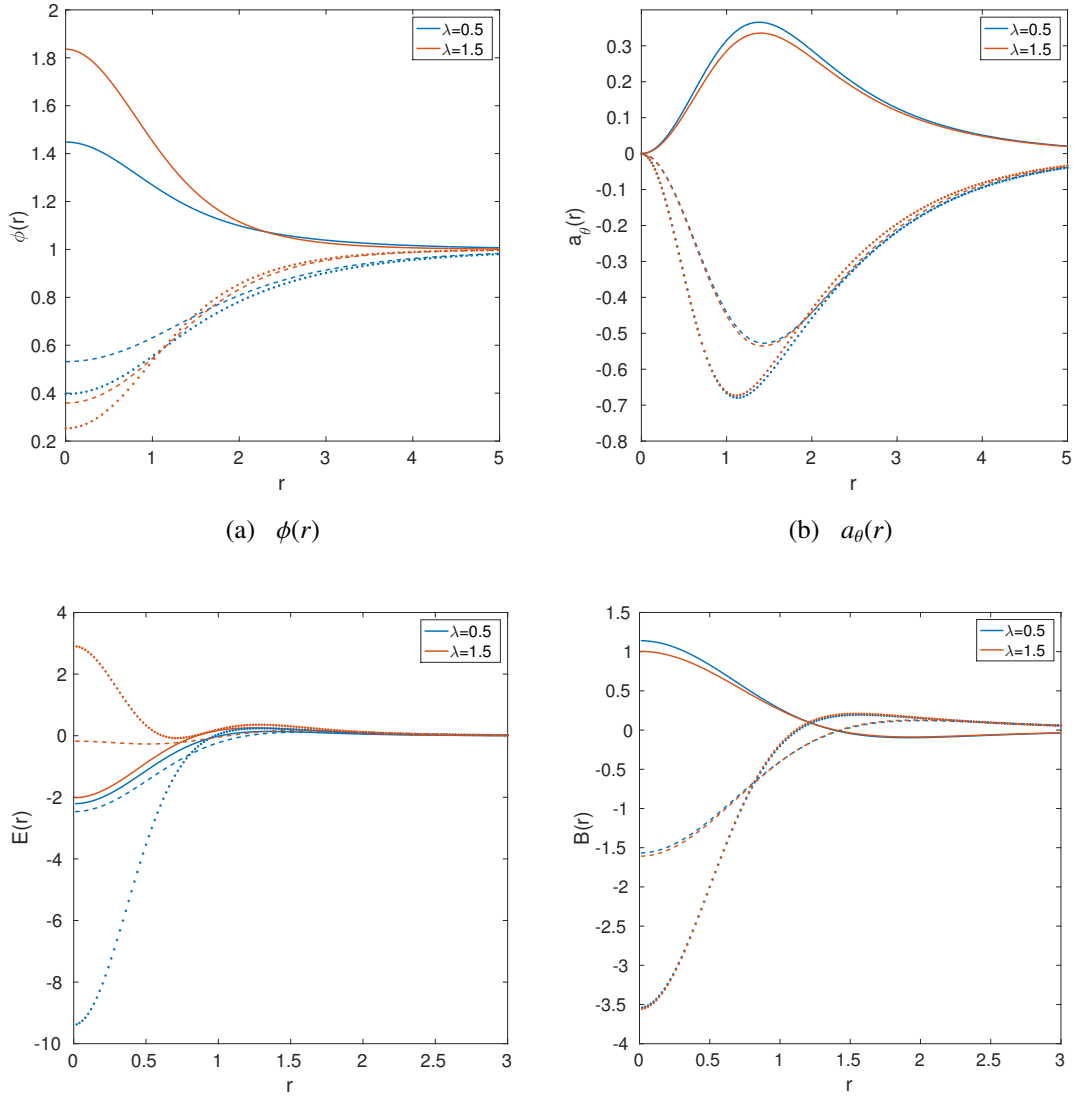

(a) $\phi(r)$ (b) $a_\theta(r)$

(c) $E(r)$ (d) $B(r)$

Figure 5.1: Vacuum solutions obtained by solving equations (5.10) with $\lambda = 0.5$ (in blue), and $\lambda = 1.5$ (in red), in the presence of the impurities $\sigma(r) = 4e^{-r^2}$ (solid lines), $\sigma((r) = -4e^{-r^2}$ (dashed lines), and $\sigma(r) = -8e^{-2r^2}$ (dotted lines). In the subfigures we display (a) profile function $\phi(r)$, (b) profile function $a_\theta(r)$, (c) energy density $E(r)$, (d) magnetic field $B(r)$.

$c \to -\infty$, and $\phi(0) \to \infty$ as $c \to +\infty$. We have observed the same behaviour away from critical coupling, and this has been tested over a much greater range of c than those shown here. In Fig. 5.1(b) we see that $a_\theta(r) \geq 0$ for $c > 0$ and $a_\theta \leq 0$ for $c < 0$.

The energy density plot shows that there is a region of negative energy density, which is not the case in the absence of a magnetic impurity. We previously saw that it is possible to derive a lower bound on the energy for any λ as (5.8), with the bound saturated when $\lambda = 1$.

Since there is a lower bound on the energy for any λ and σ, even with the negative energy density taken into account the energy has a minimal value. For $c > 0$, the energy density for $\lambda = 0.5$ is similar in shape to that for $\lambda = 1.5$ and the same impurity, however for $c < 0$ there is a significant difference in the energy density depending on λ. For $\lambda = 0.5$, the region of negative energy density becomes more significant, which is especially clear for $\sigma(r) = -8e^{-2r^2}$. By contrast, for $\lambda = 1.5$, the region of negative energy density becomes much less significant. For $\sigma(r) = -8e^{-2r^2}$, the energy density is positive at the origin, whereas all other solutions have negative energy density at the origin. We see from Fig. 5.1(d) that the value of λ does not significantly alter the magnetic field $B(r)$, though changing the sign of c roughly reverses the sign of $B(r)$.

We examine more carefully the effect of varying the coupling constant λ on the vacuum solutions in Fig. 5.2. This displays the profile functions, energy density and magnetic field for the vacuum solutions with $\sigma(r) = 4e^{-r^2}$, and $\lambda = 0.5,\ 1.0,\ 1.5$. We see in Fig. 5.2(a) that the value of $\phi(0)$ increases with increasing λ. Similarly, Fig. 5.2(b) indicates that the maximum of $a_\theta(r)$ increases with increasing λ. The energy density, as shown in Fig. 5.2(c), has a more significant region of negative energy for $\lambda < 1$, and for such values of the coupling constant, the total vacuum energy is negative. For $\lambda > 1$, the positive region of the energy density is more significant, and the total vacuum energy is positive. At critical coupling our numerical methods evaluate the energy as zero to five decimal places. Though we see from Fig. 5.2(d) that there are some differences in the magnetic field depending on λ, the value of the topological charge is unaffected, as we would expect.

For $c < 0$, the authors of Ref. [86] applied a singular gauge transformation to show in the case of critical coupling that a delta function impurity of the form $-4\pi\alpha\delta(z)$ for $\alpha \in \mathbb{N}$ "behaves" like an $(N + \alpha)$-vortex solution. By "behaves" we mean that the vortex and impurity solution looks identical to an $(N + \alpha)$-vortex solution with the gauge field shifted down by α. In Fig. 5.3, we plot vacuum profile functions $\phi(r)$, $a_\theta(r)$ for impurities of the form $\sigma(r) = -4de^{-dr^2}$. As d increases, these impurities approach the delta function with $\alpha = 1$. We display vacuum solutions for $\lambda = 0.5,\ 1.0,\ 1.5$, and in each subfigure we also plot an $N = 1$ vortex profile function for the same λ as a solid black line. For $a_\theta(r)$, the $N = 1$ profile function is shifted down so that it can be compared with the impurity vacuum solutions. As d increases, regardless of the value of λ, the vacuum solutions approach the vortex profile functions, with a singularity at the origin for $a_\theta(r)$. This suggests that, for

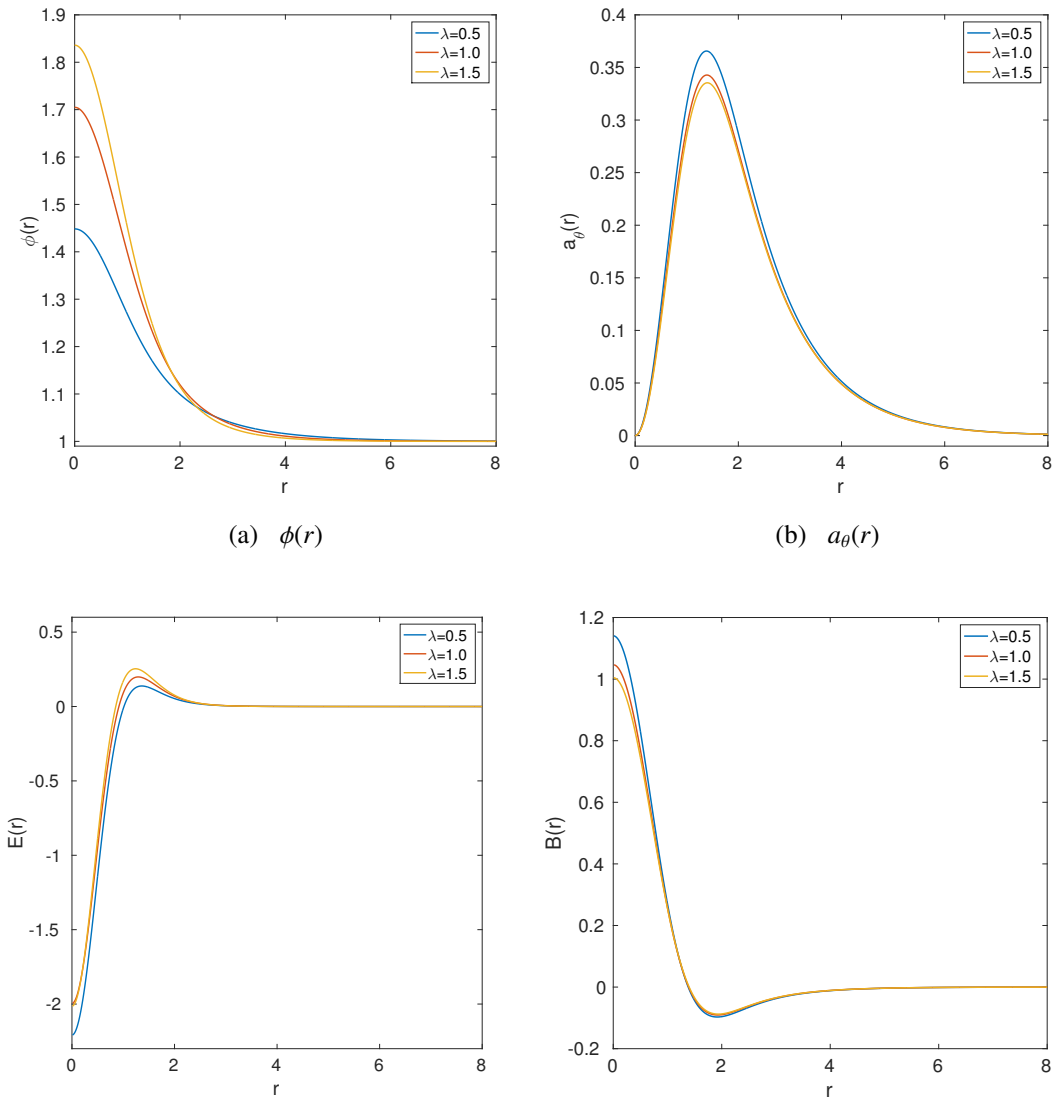

(a) $\phi(r)$ (b) $a_\theta(r)$

(c) $E(r)$ (d) $B(r)$

Figure 5.2: Vacuum solutions obtained by solving equations (5.10) with three different values of λ in the presence of the impurity $\sigma(r) = 4e^{-r^2}$. In each subfigure, we display (a) profile function $\phi(r)$, (b) profile function $a_\theta(r)$, (c) energy density $E(r)$, (d) magnetic field $B(r)$.

negative c, a delta function impurity behaves like a vortex in the Type I and II regimes, as well as at critical coupling. The numerical evidence is compelling, and it should be possible to generalise the argument of Ref. [86] to any value of λ.

In the following, we present our initial progress towards a generalisation of the argument of Ref. [86]. The idea is to formally relate an axial vortex of degree $N = n + m$ with an axial vortex of degree n in the presence of an impurity of strength m via a singular gauge

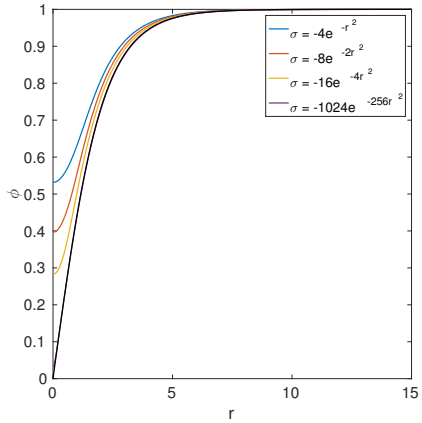

(a) $\lambda = 0.5,\ \phi(r)$

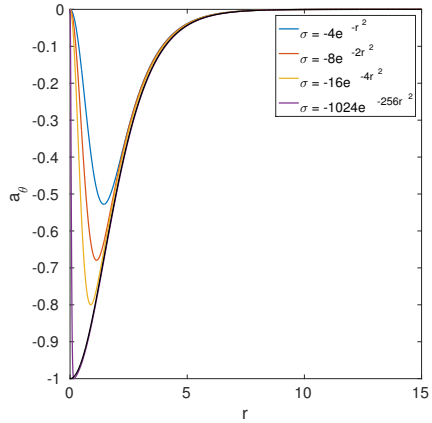

(b) $\lambda = 0.5,\ a_\theta(r)$

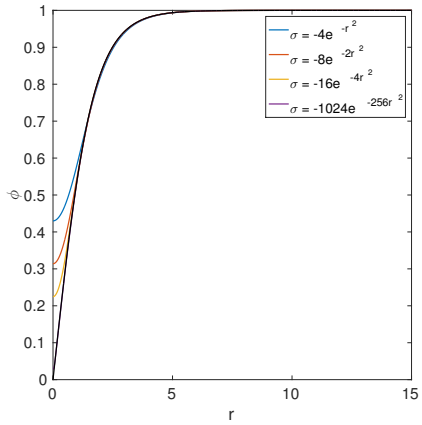

(c) $\lambda = 1.0,\ \phi(r)$

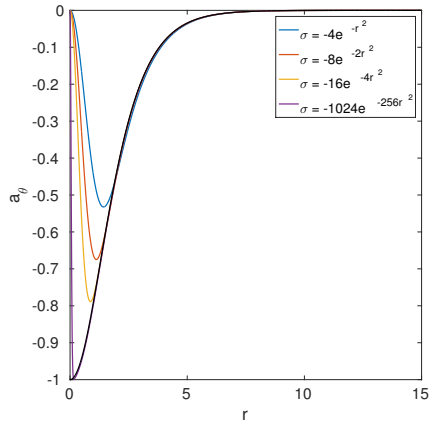

(d) $\lambda = 1.0,\ a_\theta(r)$

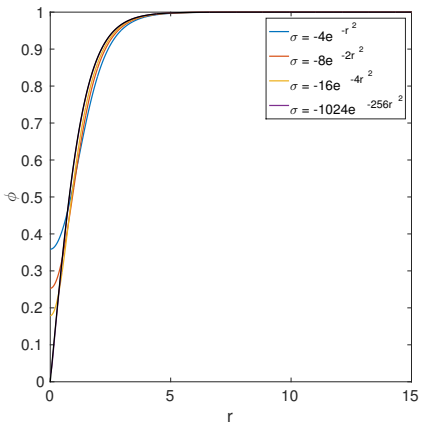

(e) $\lambda = 1.5,\ \phi(r)$

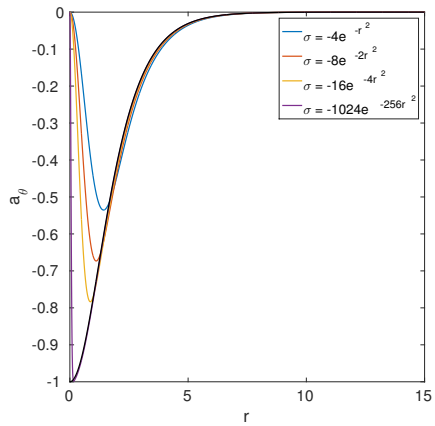

(f) $\lambda = 1.5,\ a_\theta(r)$

Figure 5.3: Vacuum profile functions $\phi(r)$, $a_\theta(r)$ for impurities $\sigma(r) = -4de^{-dr^2}$ and coupling constants (a) $\lambda = 0.5$, (b) $\lambda = 1.0$, (c) $\lambda = 1.5$. In each subfigure we plot an $N = 1$ vortex profile function for that coupling constant as a solid black line. Note that for a_θ the profile function is shifted down to enable comparison with the impurity vacuum solutions.

transformation. As in the argument at critical coupling, we define

$$h = 2\log\phi, \tag{5.11}$$

so $e^h = |\phi|^2$. The quantity h is gauge invariant, and it is finite everywhere except for at the zeros of ϕ. We will rewrite the profile function equations (5.10) for an axial vortex of degree N in terms of h. First we consider the equation for ϕ from (5.10) with no impurity ($\sigma \equiv 0$). This can be written in terms of h as

$$h'' + \frac{1}{r}h' + \frac{1}{2}\left(h'\right)^2 - \frac{2\left(N - a_\theta\right)^2}{r^2} + \lambda\left(1 - \mathrm{e}^h\right) = 2N\delta(r). \tag{5.12}$$

This is well-defined for $r > 0$, but the first four terms become singular as $r \to 0$. For $r \approx 0$, the Higgs field satisfies $\phi \approx r^N$, so $h \approx 2N\log r$. The terms $h'' + \frac{1}{r}h'$ are the radial part of the Laplacian. Since $\log r$ is the Green's function of the two dimensional Laplacian, we have regularised these terms by adding $2N\delta(r)$ on the right-hand-side of equation (5.12).

The remaining singular terms as $r \to 0$ are

$$\frac{(h')^2}{2} - \frac{2(N - a_\theta)^2}{r^2}. \tag{5.13}$$

Recall that the gauge field a_θ satisfies the boundary conditions $a_\theta(0) = 0$ and $a_\theta(\infty) = N$. Using the boundary condition $a_\theta(0) = 0$ and differentiating h for $r \approx 0$ as $h' \approx 2N/r$, we see that these two terms cancel.

We have now rewritten the profile function equation (5.10) for the Higgs field ϕ of an axial vortex of degree $N = n + m$ in terms of h. To relate this to an axial vortex of degree n in the presence of an impurity of strength m, we perform the singular gauge transformation $a_\theta(r) \mapsto \tilde{a}_\theta(r) = a_\theta(r) - m$, for $r > 0$. Then equation (5.12) becomes

$$h'' + \frac{1}{r}h' + \frac{1}{2}\left(h'\right)^2 - \frac{2\left(n - \tilde{a}_\theta\right)^2}{r^2} + \lambda\left(1 + \sigma(r) - \mathrm{e}^h\right) = 2n\delta(r), \tag{5.14}$$

where we have moved $2m\delta(r)$ to the left-hand-side and defined $\sigma(r) = -\frac{2m}{\lambda}\delta(r)$. This is the radial equation of a vortex of charge n in the presence of an impurity $\sigma(r)$ at the origin.

Rewriting the equation for $\tilde{a}_\theta$ from (5.10) for an axial vortex of degree N with $\sigma \equiv 0$ in terms of h and making the singular gauge transformation $a_\theta(r) \mapsto \tilde{a}_\theta(r) = a_\theta(r) - m$ gives

$$\tilde{a}_\theta'' - \frac{\tilde{a}_\theta'}{r} + (n - \tilde{a}_\theta)\mathrm{e}^h = 0. \tag{5.15}$$

To compare this with Equation (5.10) with a non-zero impurity, we include the term $-\frac{r}{2}\sigma'$, so that (5.15) becomes

$$\tilde{a}_\theta'' - \frac{\tilde{a}_\theta'}{r} - \frac{r}{2}\sigma' + (n - \tilde{a}_\theta)\mathrm{e}^h = 0. \tag{5.16}$$

When considering the equation for ϕ, we chose $\sigma(r) = -\frac{2m}{\lambda}\delta(r)$. In this case the term $-\frac{r}{2}\sigma'$ becomes $\frac{mr}{\lambda}\delta'(r)$ which is equivalent to $-\frac{m}{\lambda}\delta(r)$ using the properties of generalised functions. We rewrite (5.16) as

$$\tilde{a}_\theta'' - \frac{\tilde{a}_\theta'}{r} + (n - \tilde{a}_\theta)\mathrm{e}^h = \frac{m}{\lambda}\delta(r). \tag{5.17}$$

As $r \to \infty$, the gauge potential $\tilde{a}_\theta \to n$, which is the topological charge. As $a_\theta(0) = 0$, we should have $\tilde{a}_\theta(0) = -m$. However, a solution of n vortices in the presence of a magnetic impurity would have the boundary condition $\tilde{a}_\theta(0) = 0$. Equation (5.17) is singular at $r = 0$, which is consistent with a jump of the form $\tilde{a}_\theta(0) = 0$ and $\lim_{r\to 0^+} \tilde{a}_\theta = -m$. This confirms the observation that $\tilde{a}_\theta(r)$ is not well defined at the origin. It remains to fully understand the equation for the gauge potential and the role of the factor of λ in the chosen form of $\sigma(r)$.

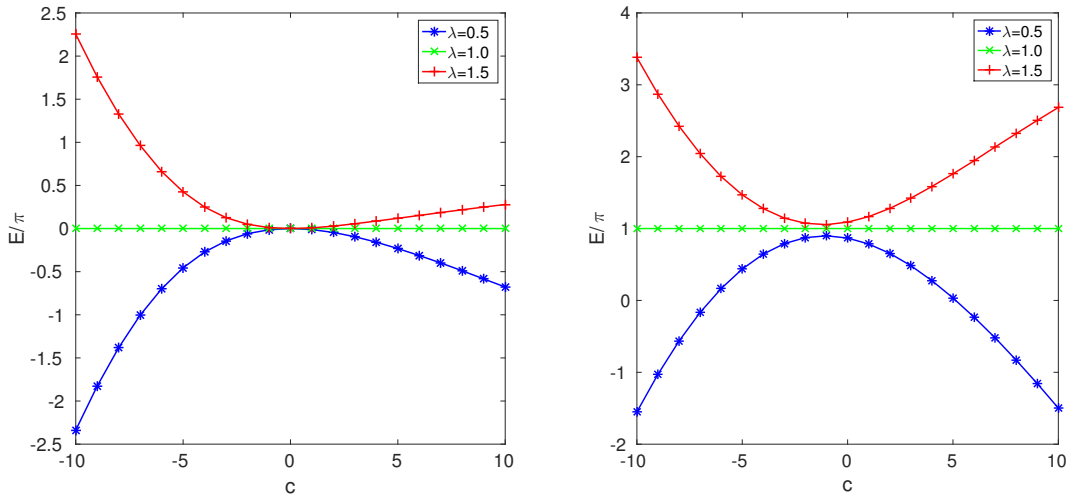

(a) $N = 0$ (b) $N = 1$

Figure 5.4: Energy E/π of profile function solutions obtained by solving equations (5.10). In each subfigure we display energy against c for impurities of the form $\sigma(r) = ce^{-r^2}$ with topological charge (a) $N = 0$, and (b) $N = 1$.

In Fig. 5.4 we compare the energy of profile function solutions to equations (5.10) for $\lambda = 0.5,\ 1.0,\ 1.5$ and different values of the topological charge N. Fig. 5.4(a) gives the vacuum energy as a function of c for impurities of the form $\sigma(r) = ce^{-r^2}$. For any λ, the vacuum energy is zero at $c = 0$, since this describes the case in which there is no impurity. For $\lambda = 0.5$, the vacuum energy is negative and decreases as $|c|$ increases, whilst for $\lambda = 1.5$ the energy is positive and increasing with $|c|$. Note that for $c < 0$, the energy increases or decreases more steeply than for $c > 0$, and at roughly the same rate for both $\lambda = 0.5$ and

$\lambda = 1.5$. However for $c > 0$, the decrease in energy for $\lambda = 0.5$ is steeper than the increase in energy for $\lambda = 1.5$.

Fig. 5.4(b) displays energy as a function of c for topological charge $N = 1$. For both $\lambda = 0.5$ and $\lambda = 1.5$, the energy curves away from the constant energy $E_1\big|_{\lambda=1}/\pi = 1$, with the point of closest approach to this line being at $c \approx -1.3$, though the specific value is slightly different for each λ. For $c > 0$, the energy for $\lambda = 1.5$ is strictly increasing with increasing c, and for $\lambda = 0.5$ it is strictly decreasing. However for $c < 0$ there is a region in which the energy decreases with decreasing c for $\lambda = 1.5$, and increases for $\lambda = 0.5$. This is interesting as it indicates that for $\lambda > 1$ we can lower the energy of a vortex by including an impurity. As is the case in the absence of an impurity, the energy for $\lambda < 1$ is strictly less than $E_1\big|_{\lambda=1}/\pi = 1$ for any c, whilst the energy for $\lambda > 1$ is strictly greater than 1.

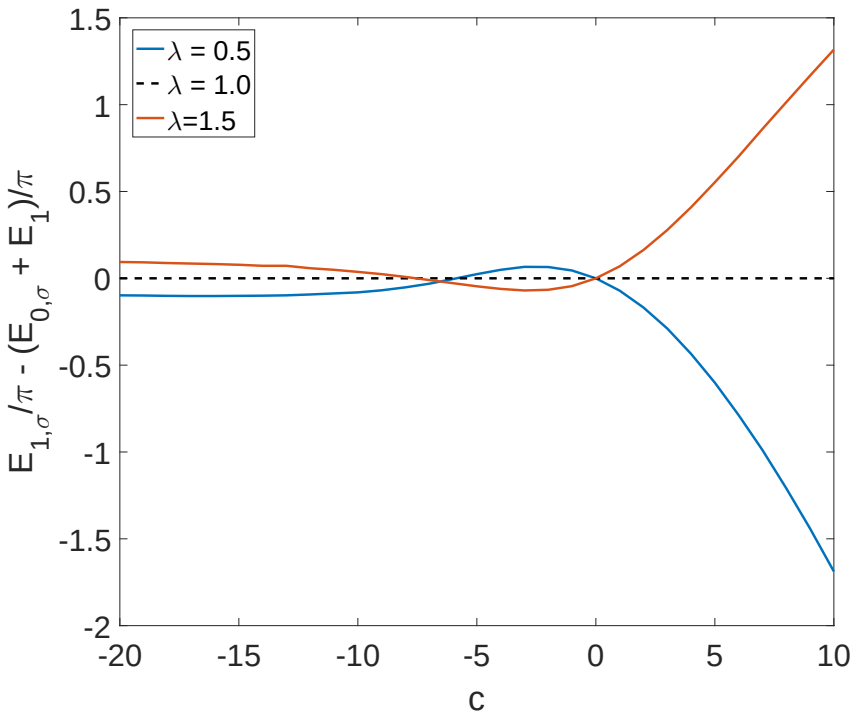

Figure 5.5: Energy difference $\left(E_{1,\sigma} - (E_{0,\sigma} + E_1)\right)/\pi$ as a function of c for impurities of the form $\sigma(r) = ce^{-r^2}$, and $\lambda = 0.5,\ 1.0,\ 1.5$. Where the energy difference is positive, the impurity will repel a vortex, and where it is negative the impurity and vortex will attract.

To determine whether a vortex and impurity will attract or repel, we consider the difference between the energy of an impurity coincident to a vortex and one which is well-separated from the vortex. Let $E_{N,\sigma}$ denote the energy of an N-vortex profile function coincident to an impurity σ, and E_N the energy of an N-vortex profile function with no impurity.

We approximate the energy of a well-separated vortex and impurity by $(E_1 + E_{0,\sigma})$: the sum of the energy of a single vortex with no impurity and the vacuum energy for the impurity σ. If $E_{1,\sigma} - (E_1 + E_{0,\sigma}) > 0$, then the energy is lower when the vortex and impurity are well-separated and so they will repel. If $E_{1,\sigma} - (E_1 + E_{0,\sigma}) < 0$ then the energy is lower when the vortex and impurity are coincident and so they will attract.

In Fig. 5.5, we plot the energy difference $E_{1,\sigma} - (E_1 + E_{0,\sigma})$ against c for impurities of the form $\sigma(r) = ce^{-r^2}$, and $\lambda = 0.5,\ 1.0,\ 1.5$. At critical coupling, the energy difference is always zero since the vortex and impurity neither attract nor repel. The energy difference is also zero at $c = 0$ for any λ because there is no impurity in this case. For $c > 0$, the energy difference is positive for $\lambda = 1.5$, and negative for $\lambda = 0.5$, indicating that a vortex and impurity will repel for $\lambda = 1.5$ and attract for $\lambda = 0.5$. For $c < 0$, there are two regimes in which the impurity can either attract or repel a vortex, and the range of c for which each behaviour occurs depends on λ. For $\lambda = 1.5$, if $c \in (-7.5, 0)$ then the energy difference is negative so the impurity attracts a vortex, and for $c < -7.5$ the energy difference is positive so the vortex and impurity repel. Similarly, for $\lambda = 0.5$, the energy difference is positive for $c \in (-5.84, 0)$, and negative for $c < -5.84$. At the critical values of c between each regime, the energy difference is zero, and so the vortex and impurity neither attract nor repel.

Since for $c < 0$ a delta function impurity behaves like another vortex, we would expect it to attract a vortex for $\lambda < 1$ and repel it for $\lambda > 1$. However we have found two different regimes of behaviour for $c < 0$ in which the impurity can either attract or repel a vortex. The critical value of c separating the two regimes depends on the coupling constant λ and the impurity parameter d. For each λ, we calculate these values by fixing d and evaluating the energy difference $E_{1,\sigma} - (E_1 + E_{0,\sigma})$ for a range of c. The value of c at which the energy difference is zero is the critical value separating the two regimes for the chosen d. In Fig. 5.6, we plot the critical values of c against d for $\lambda = 0.5,\ 1.5$ in blue and red respectively. We will refer to these as the *critical lines* separating the two regimes of behaviour. Impurities for which (d, c) is located below the critical line will attract a vortex for $\lambda = 0.5$ and repel it for $\lambda = 1.5$. Conversely if (d, c) is located above the critical line, then the impurity repels a vortex for $\lambda = 0.5$ and attracts it for $\lambda = 1.5$.

We previously approximated a delta function impurity by $\sigma(r) = -4de^{-dr^2}$, which approaches a delta function of strength $\alpha = 1$ as d increases. We also plot the line $c = -4d$ corresponding to these impurities in Fig. 5.6. For small d, our approximation to a delta

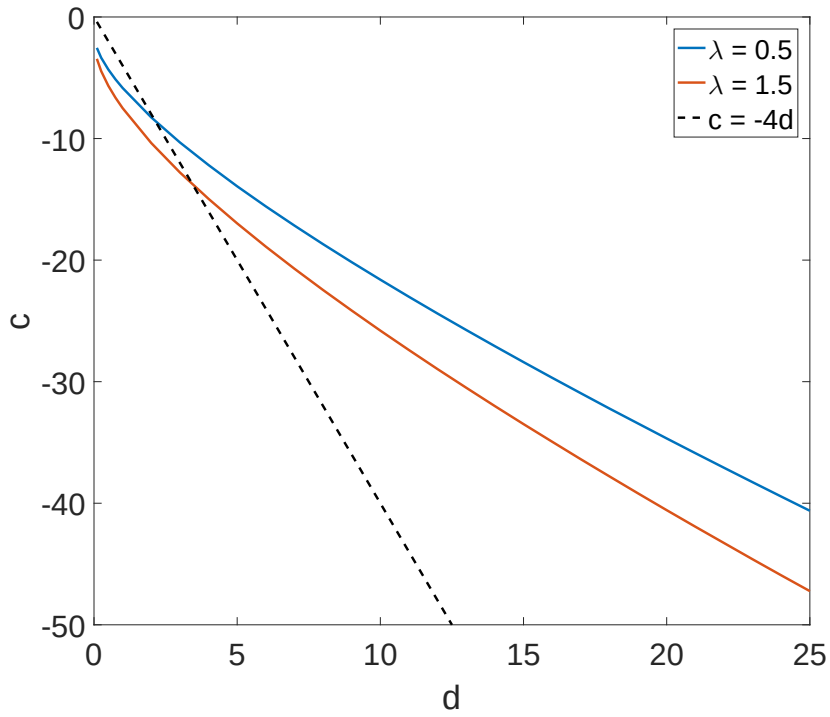

Figure 5.6: We plot the critical values of c at which the impurity changes from attracting to repelling a vortex against d for impurities of the form $\sigma(r) = ce^{-dr^2}$, and $\lambda = 0.5,\ 1.5$. The line $c = -4d$, where the impurities approach a delta function of strength $\alpha = 1$ as d increases, is shown as a dashed line for comparison.

function impurity does not behave like a vortex: the impurities are located above the critical line and will repel a vortex for $\lambda = 0.5$ and attract it for $\lambda = 1.5$. However as d increases, the line $c = -4d$ crosses the critical c line, and the impurities do behave like vortices. For $\lambda = 1.5$ the intersection between the two lines occurs at $d \approx 3.5$, and for $\lambda = 0.5$ at $d \approx 2.2$. Since an impurity of this form only becomes more like a delta function as d increases, this supports our conclusion that a delta function impurity behaves like a vortex for $c < 0$.

5.1.2 Impurity asymptotics

As a final comment on the profile function equations, we discuss the impurity strength. This is calculated in Ref. [86] by linearising the Bogomolny equation for large r, but we will calculate the same quantities by linearising the profile function equations (5.10), following a similar argument for vortices given in Ref. [87]. We consider a vacuum solution in the presence of an impurity σ. As $r \to \infty$, we have the boundary conditions $\phi(\infty) = 1$, and

$a_\theta(\infty) = 0$. We linearise the profile functions at infinity by taking

$$\phi(r) = 1 + \alpha(r), \qquad a_\theta(r) = \beta(r), \tag{5.18}$$

where $\alpha(r)$ and $\beta(r)$ are small. Assuming that the impurity decays sufficiently rapidly as $r \to \infty$, we obtain the linearised profile function equations

$$\begin{aligned} \alpha'' + \frac{1}{r}\alpha' - \lambda\alpha = 0, \\ \beta'' - \frac{1}{r}\beta' - \beta = 0, \end{aligned} \tag{5.19}$$

or equivalently

$$\begin{aligned} \lambda\left(\frac{d^2\alpha(\sqrt{\lambda}r)}{d(\sqrt{\lambda}r)^2} + \frac{1}{\sqrt{\lambda}r}\frac{d\alpha(\sqrt{\lambda}r)}{d(\sqrt{\lambda}r)} - \alpha\right) = 0, \\ \frac{d}{dr}\left(\frac{\beta}{r}\right) + \frac{1}{r}\frac{d}{dr}\left(\frac{\beta}{r}\right) - \left(1 + \frac{1}{r^2}\right)\frac{\beta}{r} = 0. \end{aligned} \tag{5.20}$$

These are identical to the equations that were obtained for a vortex in Ref. [87] and their solutions are

$$\alpha(r) = qK_0\left(\sqrt{\lambda}r\right), \qquad \beta(r) = mrK_1(r), \tag{5.21}$$

where $K_0(r)$ and $K_1(r)$ are Bessel functions. The interpretation is that for large r, the vortex, or in this case the impurity, can be considered to be made up of a scalar monopole of charge q and a magnetic dipole of moment m [87]. At critical coupling $q = m$, and this is what we call the point charge of the impurity. To show that $q = m$ in this case, we substitute the profile function expressions for $N = 0$ into the Bogomolny equations (5.6) to obtain

$$\begin{aligned} r\frac{d\phi}{dr} + a_\theta\phi = 0, \\ \frac{1}{r}\frac{da_\theta}{dr} - \frac{1}{2}(1 + \sigma - \phi^2) = 0. \end{aligned} \tag{5.22}$$

We substitute the asymptotic forms (5.18) into the first equation above and find

$$\beta(r) = -r\frac{d\alpha}{dr}. \tag{5.23}$$

Since $\frac{dK_0}{dr} = -K_1(r)$, and we have already found that $\alpha(r) = qK_0(\sqrt{\lambda}r)$, we can write $\beta(r)$ as

$$\beta(r) = qrK_1(r). \tag{5.24}$$

Comparing this with the expression for $\beta(r)$ in (5.21), we find $q = m$.

For any λ, we can calculate q and m by fitting the solutions (5.21) to numerical vacuum solutions of (5.10). In Table 5.1, we give the values of q and m for different impurities and $\lambda = 0.5,\ 1.0,\ 1.5$. Notice that the values of q and m are positive for $c > 0$ and negative for $c < 0$. We can see this by considering how the approach to the vacuum values of the profile functions in Fig. 5.1 changes with the sign of c and comparing this with the shape of the Bessel functions K_0 and K_1. For $c > 0$ the profile functions approach the vacuum from above, asymptotically matching the shape of a Bessel function, but for $c < 0$ they approach from below, matching the shapes of $-K_0$ and $-K_1$. Earlier we discussed the conjecture that impurities $\sigma(r)$ approaching a delta function will behave like a vortex. In Table 5.1 we illustrate this at critical coupling with impurities $\sigma(r) = -4e^{-r^2},\ -8e^{-2r^2},\ -16e^{-4r^2}$ approaching a delta function. The point charge of a single critically coupled vortex was numerically calculated in Ref. [88] as 1.7079. We see in the table that the strength of the impurity approaches this value as the impurity approaches a delta function, with the values already identical to two decimal places for $\sigma(r) = -16e^{-4r^2}$.

In Ref. [87], the vortex asymptotics was used to understand how the attraction or repulsion between two vortices depends on the value of λ. Since we have found the large r behaviour of an impurity to be of the same form as that of a vortex, we adapt the expression for the intervortex potential of two vortices (see for example Ref. [87]) to obtain that for a vortex and an impurity. Let $q_\sigma,\ m_\sigma$ be the charge and moment of an impurity σ, and $q_V,\ m_V$ correspond to those of a vortex. Then the static potential is given by

$$U(s) = 2\pi\left(m_\sigma m_V K_0(s) - q_\sigma q_V K_0(\sqrt{\lambda}s)\right). \tag{5.25}$$

Here s denotes the distance between the vortex and impurity. We plot the potential (5.25) for three different impurities in Fig. 5.7. In each figure, the black dashed line gives the potential for $\lambda = 1$, which, since $q = m$ here, is always zero. We plot the potential for $\lambda = 0.5$ in blue, and for $\lambda = 1.5$ in red. Each figure represents a different regime of impurity behaviour as observed in the previous section: (a) $c > 0$, (b) $c < 0$ above the critical line separating the two behaviours (as shown in Fig. 5.6), and (c) $c < 0$ below the critical line. The potential for $c > 0$ is the most clearly different from the other two, as the signs of the Bessel functions have been reversed. Figs. 5.7(b) and (c) are a similar shape to one another, though in (c) the critical points of the functions are more exaggerated. We note that this approximation is only accurate past some critical value of the separation between the vortex and impurity, s_c which depends on the values of q and m, and we expect it to break down for $s \leq s_c$.

Table 5.1: Some different impurities and the corresponding values of q and m.

λ	Impurity	q	m
	e^{-r^2}	0.12	0.30
	$-e^{-r^2}$	−0.16	−0.35
0.5	$2e^{-r^2}$	0.22	0.57
	$-2e^{-r^2}$	−0.35	−0.76
	$4e^{-r^2}$	0.37	1.02
	$-4e^{-r^2}$	−0.89	−1.91
	e^{-r^2}	0.29	0.29
	$-e^{-r^2}$	−0.35	−0.35
1.0	$2e^{-r^2}$	0.56	0.56
	$-2e^{-r^2}$	−0.74	−0.74
	$4e^{-r^2}$	0.99	0.99
	$-4e^{-r^2}$	−1.82	−1.82
	$-8e^{-2r^2}$	−1.73	−1.73
	$-16e^{-4r^2}$	−1.71	−1.71
	e^{-r^2}	0.50	0.30
	$-e^{-r^2}$	−0.59	−0.35
1.5	$2e^{-r^2}$	0.94	0.55
	$-2e^{-r^2}$	−1.28	−0.75
	$4e^{-r^2}$	1.64	0.98
	$-4e^{-r^2}$	−2.99	−1.77

The force due to $U(s)$ is given by

$$-U'(s) = 2\pi \left(m_\sigma m_V K_1(s) - \sqrt{\lambda} q_\sigma q_V K_1(\sqrt{\lambda} s) \right). \tag{5.26}$$

When $\lambda = 1$, we know that $q = m$ for both a vortex and an impurity, so these terms cancel and there is no force. If $\lambda < 1$, then $K_1(s)$ decays faster than $K_1(\sqrt{\lambda}s)$, and so the behaviour is determined by the sign of q_σ. For a vortex $q_v < 0$, and for an impurity we saw that $q_\sigma < 0$ if $c < 0$ and $q_\sigma > 0$ if $c > 0$. Combining these, we find that for $\lambda < 1$ the net force is negative if $c < 0$ and positive if $c > 0$. So this argument suggests that a vortex and impurity

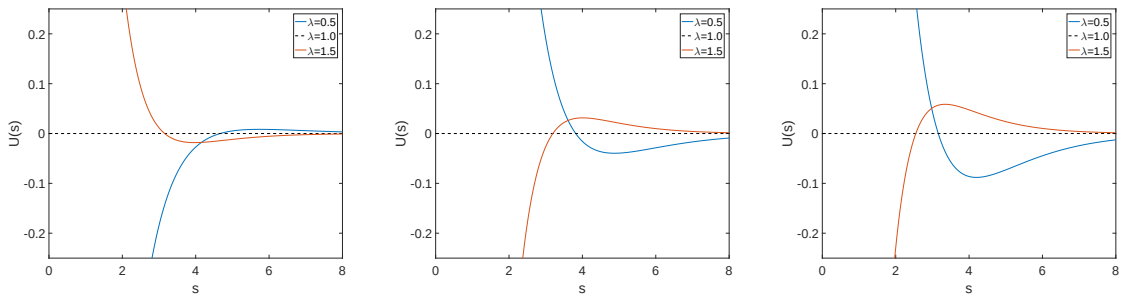

(a) $\sigma = 4e^{-r^2}$ (b) $\sigma = -4e^{-r^2}$ (c) $\sigma = -16e^{-4r^2}$

Figure 5.7: The potential (5.25) for a vortex and impurity with $\lambda = 0.5,\ 1.0,\ 1.5$ and impurities (a) $\sigma(r) = 4e^{-r^2}$, (b) $\sigma(r) = -4e^{-r^2}$, and (c) $\sigma(r) = -16e^{-4r^2}$.

will attract if $c < 0$ and repel if $c > 0$. Similarly, if $\lambda > 1$, then the $K_1(\sqrt{\lambda}s)$ term decays faster and so the $K_1(s)$ term dominates. The type of force depends on the sign of m_σ. We know that $m_V < 0$, and we have that $m_\sigma < 0$ if $c < 0$ and $m_\sigma > 0$ if $c > 0$. The net force is positive if $c < 0$ and negative if $c > 0$, indicating that a vortex and impurity will repel for $c < 0$ and attract for $c > 0$. Comparing these predictions with the three regimes that we have found by considering the energy difference, we see that they are only accurate in one case – for impurities σ found below the critical line (shown in Fig. 5.6 for $\lambda = 0.5,\ 1.5$). This argument incorrectly predicts the behaviour for both $c > 0$ and impurities with $c < 0$ found above the critical line. However the case in which an impurity approaches a delta function is correctly predicted to behave like a vortex.

5.1.3 Static vortices and impurities

Next we obtain static vortex solutions in the presence of magnetic impurities on a 2D grid. We solve the gradient flow equations

$$\begin{aligned} \partial_0\phi &= D_{ii}\phi + \frac{\lambda}{2}\left(1 + \sigma - |\phi|^2\right)\phi, \\ \partial_0 a_i &= -\epsilon_{ij}\left(\partial_j B - \frac{1}{2}\partial_j\sigma\right) - \frac{i}{2}\left(\overline{\phi}D_i\phi - \phi\overline{D_i\phi}\right), \end{aligned} \tag{5.27}$$

using a finite difference method that is first order in time, and fourth order in space, similar to that applied in Chapter. 4. We use timestep $\Delta t = 0.001$, and grid spacing $\Delta x = \Delta y = 0.1$, and typically solve on grids of size 401×401.

To generate initial conditions, we first use the vacuum profile functions obtained by solving (5.10) to create a vacuum solution on the 2D grid. Then we apply the Abriksov

ansatz (4.24) to combine this with a solution describing a vortex at a given position in the absence of an impurity. This creates an approximate solution of a vortex at the specified position in the presence of a magnetic impurity located at the origin. Where the vortex and impurity are well-separated this is already very accurate, but even for vortices close to the origin it provides us with a useful initial condition from which to begin solving (5.27).

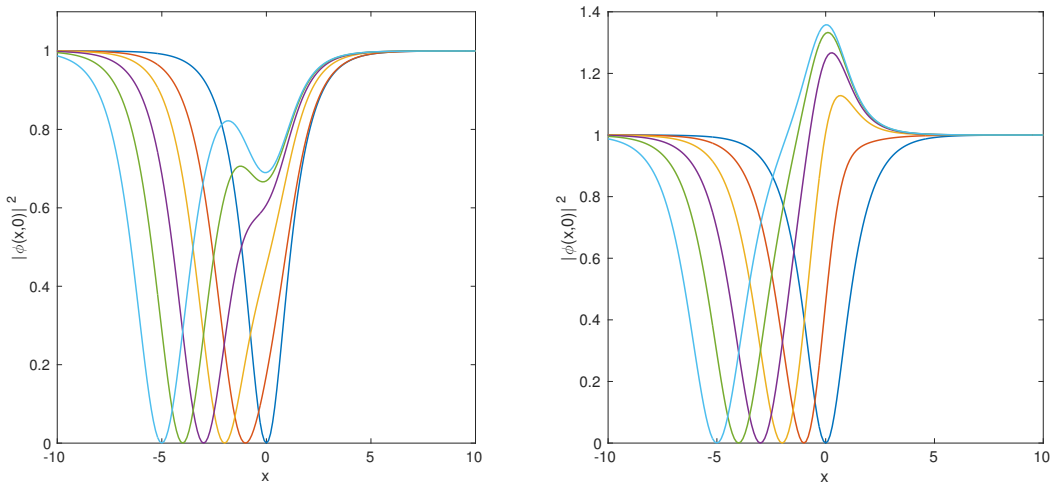

(a) $\lambda = 1.0,\ \sigma = -e^{-r^2}$ (b) $\lambda = 1.0,\ \sigma = e^{-r^2}$

Figure 5.8: Plot of $|\phi(x,0)|^2$ against x for one vortex at critical coupling placed at different positions, and two different impurities σ.

In Fig. 5.8, we plot $|\phi(x,0)|^2$ against x for critically coupled vortices positioned at a range of initial locations in the presence of the impurities (a) $\sigma(r) = -e^{-r^2}$, and (b) $\sigma(r) = e^{-r^2}$. We note that these solutions were also calculated in Ref. [86] using the Bogomolny equation (5.6). We have obtained the same solutions by solving the gradient flow equations (5.27). For vortices positioned far away from the impurity, the solution looks like a superposition of a single vortex in the absence of an impurity with the vacuum solution in the presence of a magnetic impurity. When the vortex and impurity are closer together, the effect of the impurity on the vortex becomes more apparent. We see in both of the subfigures that a vortex positioned at the origin effectively "screens" the impurity.

To numerically confirm the existence of a moduli space of solutions at critical coupling we evaluate the energy of vortex and impurity solutions for different values of the separation s between the vortex and impurity. We calculate the energy E/π for a single vortex and impurity at critical coupling to be 1 to four decimal places regardless of the separation s. To illustrate the possible cases away from critical coupling, in Fig. 5.9 we display the energy

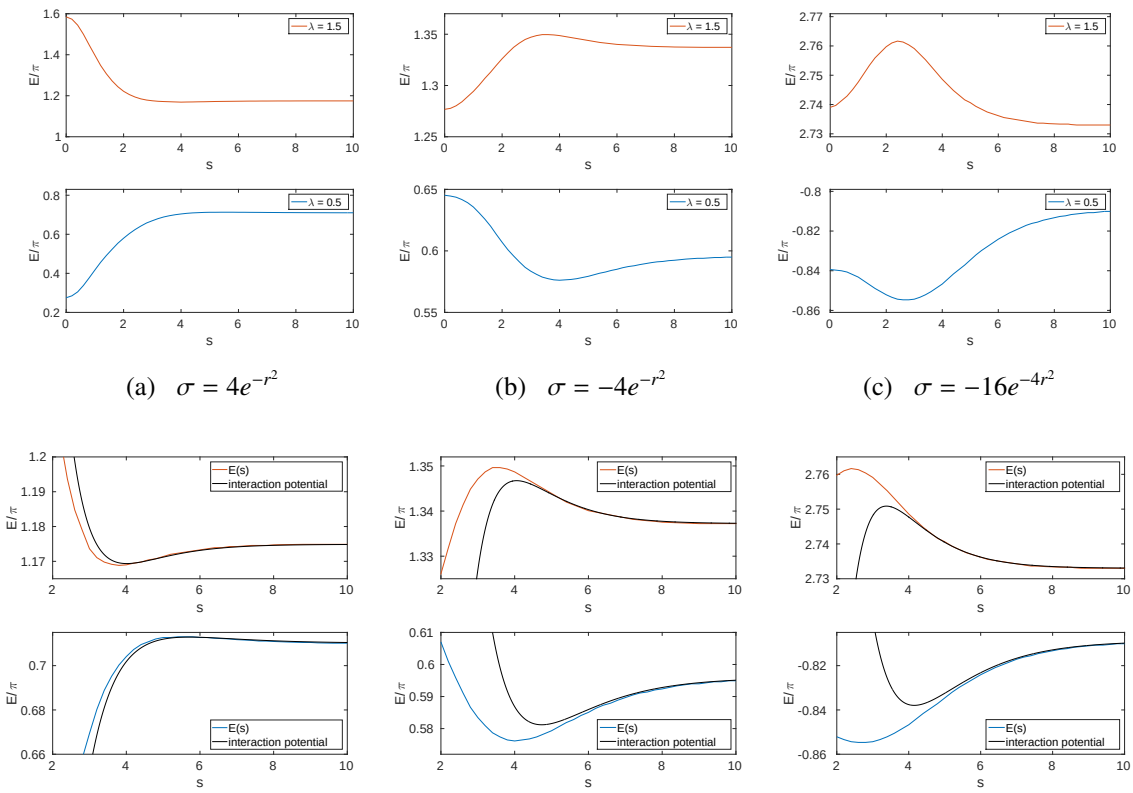

(a) $\sigma = 4e^{-r^2}$ (b) $\sigma = -4e^{-r^2}$ (c) $\sigma = -16e^{-4r^2}$

(d) $\sigma = 4e^{-r^2}$ (e) $\sigma = -4e^{-r^2}$ (f) $\sigma = -16e^{-4r^2}$

Figure 5.9: (a)-(c) Energy E/π as a function of the separation s between a single vortex and an impurity σ for $\lambda = 0.5$ (in blue) and $\lambda = 1.5$ (in red). (d)-(f) We zoom into the figures (a)-(c) for $s \geq 2$ and compare them with the corresponding interaction potential (5.25) shifted by the energy of a well-separated vortex and impurity (shown in black).

E/π of a single vortex in the presence of an impurity σ as a function of s for $\lambda = 0.5,\ 1.5$ and three different impurities. This reveals a more complicated relationship between the impurity and vortex than that predicted by considering the sign of $E_{1,\sigma} - (E_1 + E_{0,\sigma})$ and explains why the asymptotics disagreed with these results.

Figs. 5.9(a) and (d) correspond to the impurity $\sigma(r) = 4e^{-r^2}$. Here the energy calculation $E_{1,\sigma} - (E_1 + E_{0,\sigma})$ predicted that the impurity would repel the vortex for $\lambda > 1$ and attract it for $\lambda < 1$, though the asymptotics suggested the opposite effect. Initially the energy decreases with increasing s for $\lambda = 1.5$ and increases with increasing s for $\lambda = 0.5$. However a close examination of the energy at larger values of s (see Fig. 5.9(d)) reveals that this behaviour reverses for $s > 4$: the energy begins to slightly increase with s for $\lambda = 1.5$ and to very slightly decrease with s for $\lambda = 0.5$, before settling on a constant value $E|_{s\to\infty}$. This is the behaviour predicted by the asymptotics, and in Fig. 5.9(d) we also plot the corresponding

interaction potential (5.25) shifted by the value $E|_{s\to\infty}$ as a black line. The asymptotic prediction agrees very well with $E(s)/\pi$ for $s > 5$. The energy calculation disagreed with the asymptotic prediction because it only compared the energy of a well-separated vortex and impurity $E|_{s\to\infty}$ to that of a coincident vortex and impurity $E(0)$, and so it missed the subtle change in behaviour at larger values of s. The true behaviour is more complicated than that indicated by either prediction: when vortex and impurity are close, the impurity will attract the vortex for $\lambda < 1$ and repel it for $\lambda > 1$, but when they are further apart the impurity will repel the vortex for $\lambda < 1$ and attract it for $\lambda > 1$

In Figs. 5.9(b) and (e) we show similar plots for the impurity $\sigma(r) = -4e^{-r^2}$. In this case the energy calculation predicted that the impurity would attract the vortex for $\lambda > 1$ and repel it for $\lambda < 1$, and the asymptotic prediction disagreed. As before, we see that the energy prediction is correct for smaller values of s, but that the behaviour changes when $s > 4$, at which point the shifted interaction potential becomes a good fit for $E(s)/\pi$.

Figs. 5.9(c) and (f) correspond to the impurity $\sigma(r) = -16e^{-4r^2}$, which was one of the impurities for which the predictions of both the energy calculation and the asymptotics agreed. In this case they both predicted that the impurity should repel the vortex when $\lambda > 1$ and attract it when $\lambda < 1$. However, as shown in the figures, the opposite is true for small s, with the behaviour changing for $s > 2.5$. Let E_{stat} denote the energy at the stationary point of $E(s)$. Unlike the previous cases, the change in energy of the behaviour at small s is less significant than that of the behaviour at large s, i.e. $|E_{\text{stat}} - E(0)| < |E_{\text{stat}} - E|_{s\to\infty}|$. So it is the large s behaviour which determines whether $E|_{s\to\infty}$ is greater than or less than $E(0)$. Since the large s behaviour has the most significant change in energy, the energy calculation agrees with the asymptotics. In the other cases, the small s behaviour had the most significant change in energy and so the predictions disagreed.

Recall that we earlier discussed a critical line separating the two different regions of behaviour for impurities with $c < 0$. For impurities on this line, the difference in energy between a coincident vortex and impurity and a well-separated vortex and impurity was zero. However this does not mean the vortex and impurity can be placed anywhere without affecting the energy. There is still a region where, using the example of $\lambda > 1$, for small s the energy increases with increasing s, and for larger s the energy decreases with increasing s until settling on a constant value $E|_{s\to\infty}$. The energy calculation gives zero in this case because $E(0) = E|_{s\to\infty}$, but $E(s)$ is not a constant function.

5.2 Vortex dynamics with magnetic impurities

To study vortex dynamics in the presence of magnetic impurities, we return to the action (5.1). The corresponding equations of motion are

$$\begin{aligned} D_\mu D^\mu \phi - \frac{\lambda}{2}\left(1+\sigma-|\phi|^2\right)\phi &= 0, \\ \partial_\mu f^{\mu 0} + \frac{i}{2}\left(\overline{\phi} D^0 \phi - \phi \overline{D^0 \phi}\right) &= 0, \\ \partial_\mu f^{\mu 1} + \frac{1}{2}\partial_2 \sigma + \frac{i}{2}\left(\overline{\phi} D^1 \phi - \phi \overline{D^1 \phi}\right) &= 0, \\ \partial_\mu f^{\mu 2} - \frac{1}{2}\partial_1 \sigma + \frac{i}{2}\left(\overline{\phi} D^2 \phi - \phi \overline{D^2 \phi}\right) &= 0. \end{aligned} \tag{5.28}$$

We solve these equations using a leapfrog method, with derivatives that are second order accurate in time and fourth order in space. The timestep used is $\Delta t = 0.01$, with grid spacing $\Delta x = \Delta y = 0.1$ over grids that are typically of size 401×401 or 801×801. We work in the temporal gauge $a_0 = 0$ and generate initial conditions by boosting an ordinary vortex solution at a given initial position with velocity v and using the Abrikosov ansatz to combine this with a static vacuum solution for the chosen magnetic impurity.

Two quantities of interest in the study of vortex scattering are the scattering angle Θ and impact parameter b. Fig. 5.10 indicates how each of these quantities are defined within our vortex and impurity scattering simulations. The scattering angle Θ is the the angle between the trajectory of the vortex after scattering and its initial trajectory. The impact parameter b is the vertical distance between the initial trajectory of the vortex and the impurity.

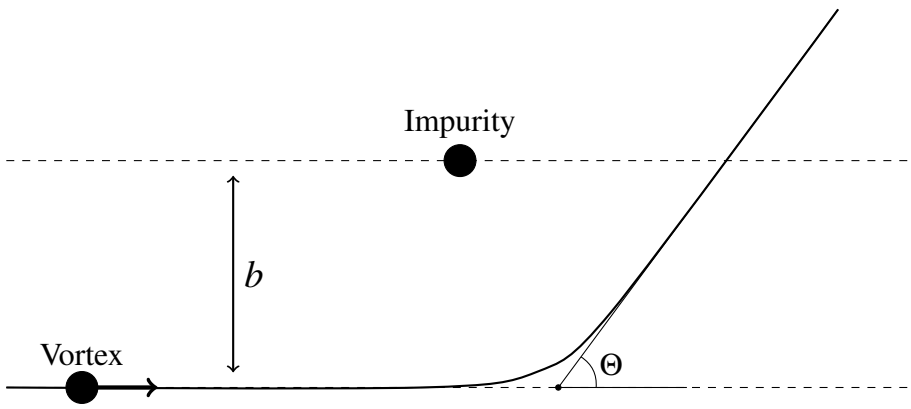

Figure 5.10: Diagram to illustrate the definition of the scattering angle Θ and impact parameter b in our simulations.

We first consider the scattering of a single vortex at critical coupling with an impurity of the form $\sigma(r) = ce^{-r^2}$. It has already been noted in Ref. [86] that an impurity of this

form with $c > 0$ will attract a slow moving vortex, and with $c < 0$ will repel the vortex. In the figures presented below, we take two different impurities $\sigma(r) = e^{-r^2}$ and $\sigma(r) = -e^{-r^2}$, but we have verified that the general behaviour is the same for other impurities also. In our simulations, the initial vortex position is $(x, y) = (-4, -b)$ for a range of $b \in [0, 8]$, and the impurity is fixed at the origin.

In Fig. 5.11, we plot the scattering angle Θ in radians as a function of the impact parameter b for a single vortex at critical coupling scattering with the magnetic impurities $\sigma(r) = e^{-r^2}$ and $\sigma(r) = -e^{-r^2}$. The initial velocity given to the vortex is $v = 0.3$. The sign of the scattering angle for $\sigma = -e^{-r^2}$ is reversed in (b) for easier comparison with the other impurity. For both impurities, when impact parameter $b = 0$, the scattering angle $\Theta = 0$: the vortex passes through the impurity in a head-on collision. As b increases, Θ also increases up to a maximum value occuring at $b \approx 1.5$. Then the scattering angle steadily decreases, returning to zero when the impurity is so far from the vortex as to no longer influence its trajectory. We note that the general shape of this plot is consistent with results obtained in Ref. [86] for vortices and impurities in hyperbolic space.

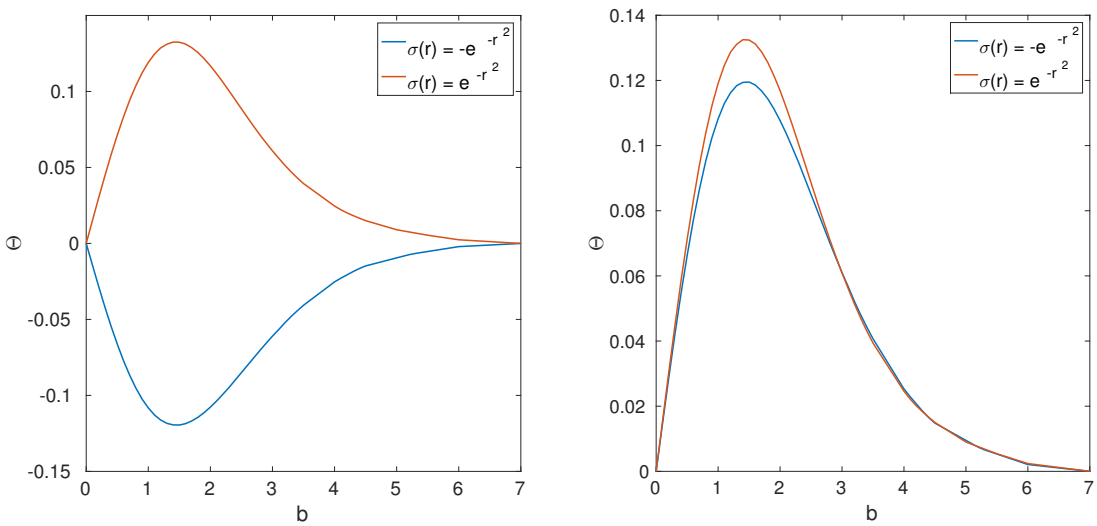

(a) (b)

Figure 5.11: (a) Scattering angle Θ in radians against impact parameter b for the scattering of a single vortex at critical coupling with impurities $\sigma(r) = e^{-r^2}$ (in red), and $\sigma(r) = -e^{-r^2}$ (in blue). The initial vortex speed is $v = 0.3$. (b) We display the same data, but for $\sigma(r) = -e^{-r^2}$ we plot $-\Theta$ for easier comparison with the scattering angle for $\sigma(r) = e^{-r^2}$.

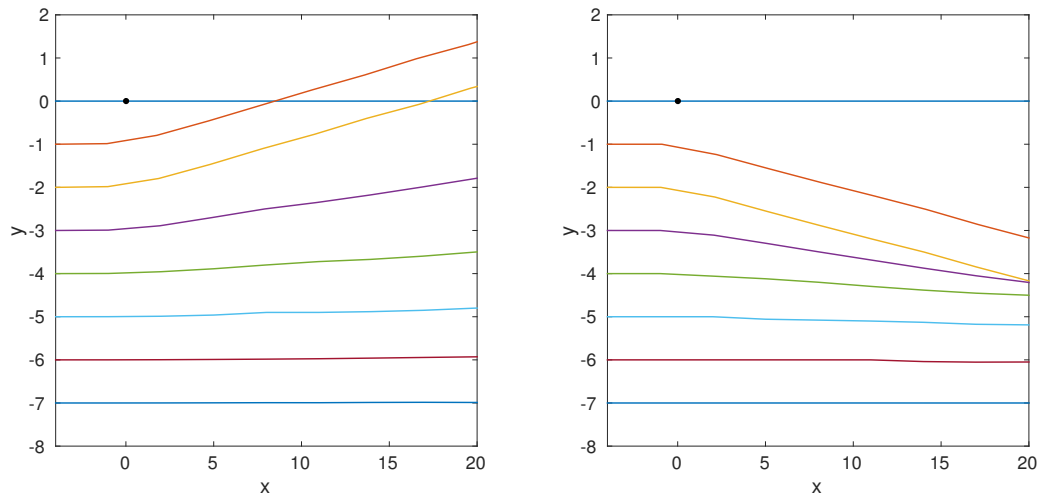

(a) $\sigma(r) = e^{-r^2}$ (b) $\sigma(r) = -e^{-r^2}$

Figure 5.12: Vortex trajectories during the scattering of a single vortex at critical coupling with impurities (a) $\sigma(r) = e^{-r^2}$ and (b) $\sigma(r) = -e^{-r^2}$ for the impact parameter values $b = 0, 1, 2, 3, 4, 5, 6, 7$ and initial velocity $v = 0.3$. The location of the impurity is indicated with a black dot.

The scattering angle plots can be compared with Fig. 5.12 which shows the corresponding vortex trajectories for a selection of impact parameter values. The location of the impurity is indicated with a black dot. We see that in a head-on collision with either impurity, the vortex will pass through the impurity and continue on its original trajectory. Similarly in both cases, for impact parameter $b = 7$, the vortex is far enough from the impurity that its trajectory is unaffected, and it continues to travel along the x-axis as though the impurity was not there. In between these values, the vortex trajectories are altered by the presence of the impurity, bending towards the impurity for $c > 0$ and away from it for $c < 0$. We saw in Fig. 5.11 that the maximum scattering angle is found when $b \approx 1.5$, after which the angle decreases with increasing impact parameter. In Fig. 5.12, we see that the most altered trajectories are those for $b = 1, 2$, and after this the trajectories start to flatten out.

Though we have seen that the vortex will travel through both impurities in a head-on collision without altering its initial trajectory, the details are different depending on the sign of c. Fig. 5.13 displays snapshots of the energy density of the configurations at different times during the head-on scattering of a single vortex at critical coupling with the impurities (a)-(c): $\sigma(r) = e^{-r^2}$, and (d)-(f): $\sigma(r) = -e^{-r^2}$. In both cases, we begin with the vortex and impurity well separated. The effect of the impurity on the energy density can be seen in the

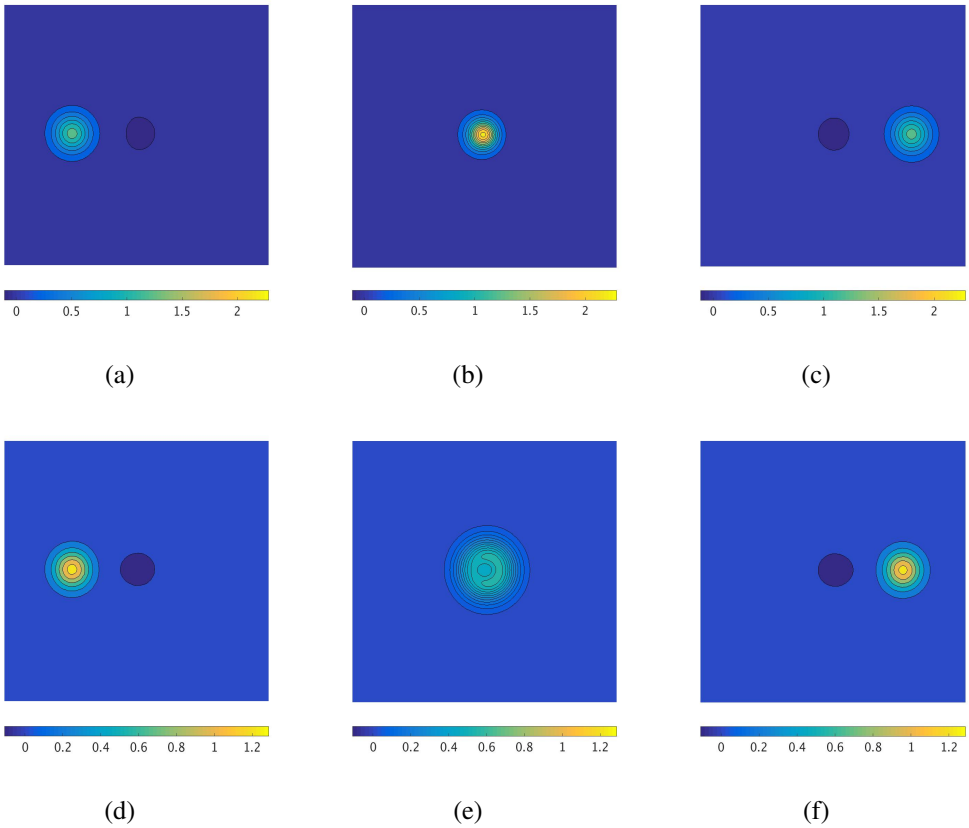

Figure 5.13: Snapshots of the energy density during the scattering of a single vortex at critical coupling with impurities (a)-(c): $\sigma(r) = e^{-r^2}$ and (d)-(f): $\sigma(r) = -e^{-r^2}$ for initial velocity $v = 0.3$.

contour plot as a region of negative energy density, and the vortex is a localised lump of energy. When the vortex crosses the impurity with $c > 0$, as seen in Fig. 5.13(b), there is a localised lump of energy at the origin which is taller than the energy of the vortex alone. By contrast, for $c < 0$, as seen in Fig. 5.13(e), the energy forms a less localised ring, resembling an $N = 2$ vortex, at the origin, which is smaller than the energy of the single vortex was originally. In both cases, after scattering the vortex and impurity appear unchanged by their interaction, and the vortex continues on its original path.

We now consider the scattering of a 2-vortex ring at critical coupling with the same two impurities. In Fig. 5.14 we display snapshots of the energy density at different times during the head-on scattering of a vortex ring with initial velocity $v = 0.3$ and impurities (a)-(c): $\sigma(r) = e^{-r^2}$ and (d)-(f): $\sigma(r) = -e^{-r^2}$. In both cases, we initially see the vortex as a ring of energy density and the impurity as a region of negative energy density at the origin. As the vortex passes through the impurity for $c > 0$, seen in Fig. 5.14(b), a lump of

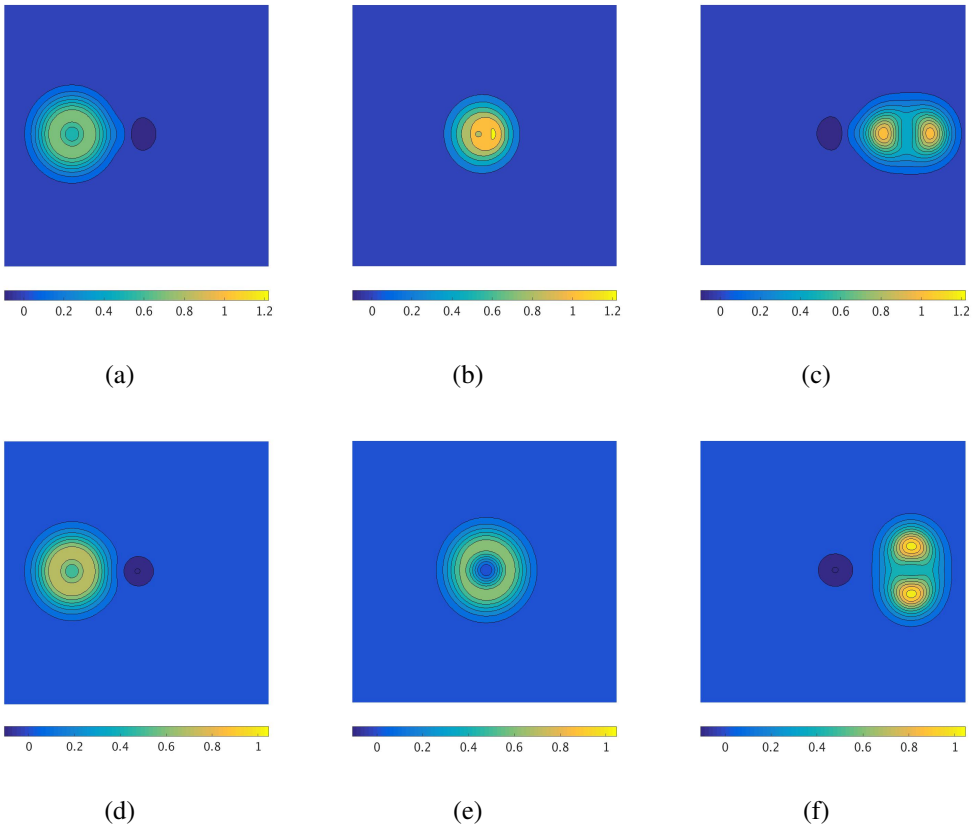

Figure 5.14: Snapshots of the energy density during the scattering of a 2-vortex ring at critical coupling with impurities (a)-(c): $\sigma(r) = e^{-r^2}$ and (d)-(f): $\sigma(r) = -e^{-r^2}$ for initial velocity $v = 0.3$.

energy taller than the vortex ring is formed at the origin. When the vortices emerge on the other side of the impurity in Fig. 5.14(c), we see the ring break up into two vortices along the x-axis. We observe a different behaviour for $c < 0$. Fig. 5.14(e) shows the vortex ring and impurity coincident. Here the energy forms a ring similar to an $N = 3$ vortex solution. When the vortices emerge on the other side of the impurity, the ring has broken up into two vortices along the y-axis. This is shown in Fig. 5.14(f). The vortices continue to move in the x-direction, but also separate to infinity in the y-direction.

Finally, we investigate the scattering of two $N = 1$ vortices at critical coupling in the presence of a magnetic impurity. In these simulations, we begin with a static impurity at the origin and two vortices located at $(\pm 4, \pm b)$, where b is the impact parameter between each vortex and the impurity, as illustrated in Fig. 5.10. The impact parameter between the two vortices is $2b$. We boost the vortices towards each other in the x-direction with initial velocity $v = 0.3$.

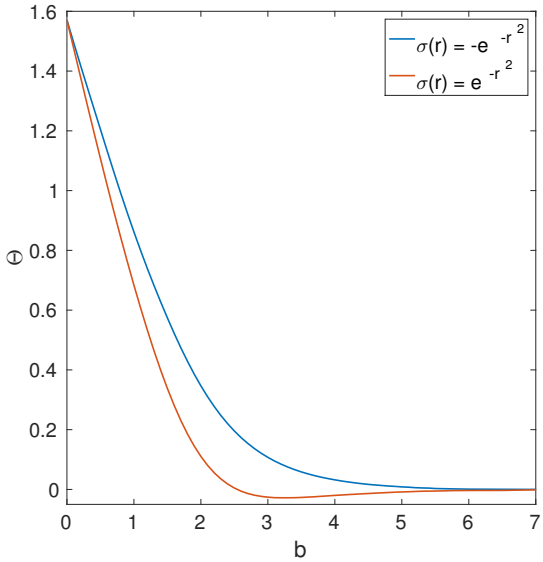

Figure 5.15: Scattering angle Θ in radians against impact parameter b for the scattering of two vortices at critical coupling in the presence of impurities $\sigma(r) = e^{-r^2}$ (in red) and $\sigma(r) = -e^{-r^2}$ (in blue).

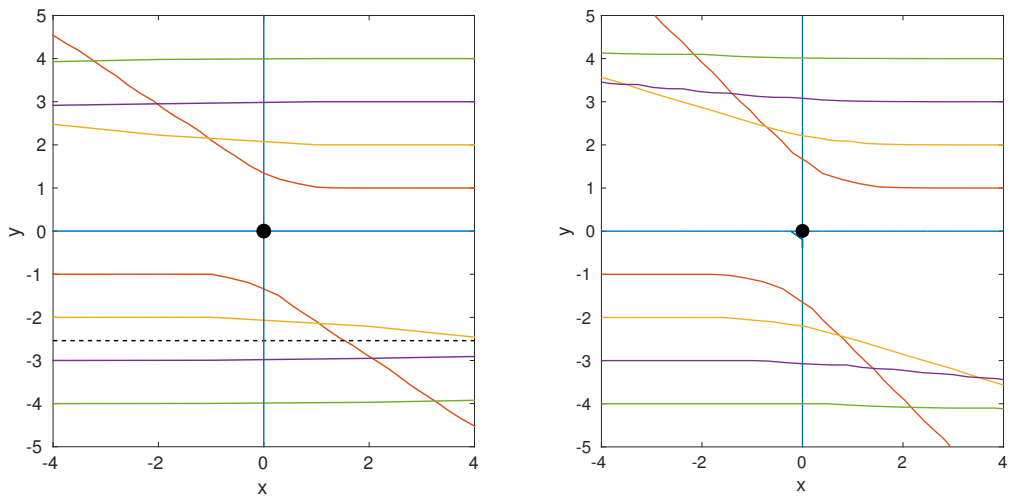

(a) $\sigma(r) = e^{-r^2}$ (b) $\sigma(r) = -e^{-r^2}$

Figure 5.16: Vortex trajectories during the scattering of two vortices at critical coupling in the presence of impurities (a) $\sigma(r) = e^{-r^2}$ and (b) $\sigma(r) = -e^{-r^2}$ for impact parameter values $b = 0, 1, 2, 3, 4$ and initial velocity $v = 0.3$. In (a), we also plot the trajectory for $b = 2.54$ (where the scattering angle changes sign) as a black dashed line. The location of the impurity is indicated with a black dot, and the vortices are initially located at $(\pm 4, \pm b)$.

In Fig. 5.15 we plot the scattering angle as a function of impact parameter for two vortices scattering in the presence of impurities $\sigma(r) = e^{-r^2}$ and $\sigma(r) = -e^{-r^2}$. For impact

parameter $b = 0$, the vortices scatter at right angles, as is the case in a head-on collision of two vortices in the absence of an impurity. As the impact parameter increases, the scattering angle decreases. For $\sigma(r) = -e^{-r^2}$, the vortex trajectories bend away from each other and the impurity. This can be seen in Fig. 5.16(b). For $\sigma(r) = e^{-r^2}$, the direction of the vortex trajectories changes after a certain value of the impact parameter. We see in Fig. 5.16(a) that the trajectories for $b = 1, 2$ bend away from the impurity, but for $b = 3, 4$ bend towards it. The critical value where the scattering angle crosses zero is $b = 2.54$, and we show this trajectory as a black dashed line. In Fig. 5.15(a), this change in direction corresponds to the change in sign of the scattering angle Θ. Initially the repulsion between the vortices is more significant than the attraction between each vortex and the impurity. Once the vortices are sufficiently separated, the attraction to the impurity becomes the strongest effect.

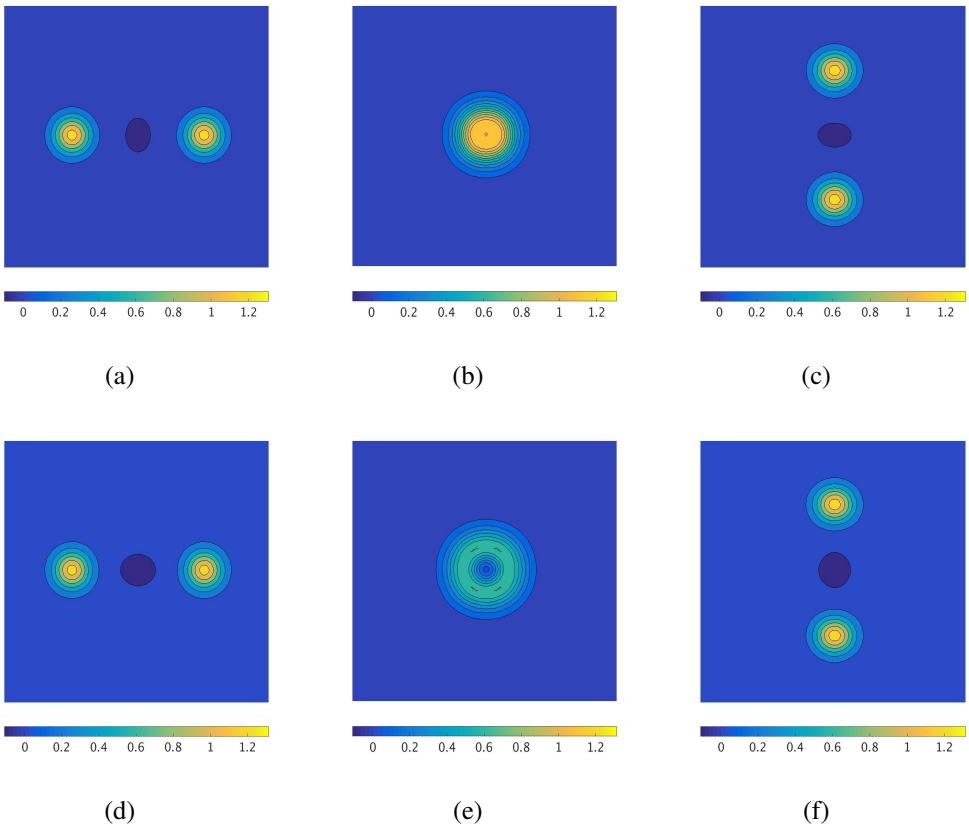

Figure 5.17: Snapshots of the energy density during the scattering of two $N = 1$ vortices at critical coupling through impurities (a)-(c): $\sigma(r) = e^{-r^2}$ and (d)-(f): $\sigma(r) = -e^{-r^2}$ for initial velocity $v = 0.3$.

Snapshots of the energy density during the head-on collision of two vortices through an impurity located at the origin are given in Fig. 5.17. The initial velocity given to the vortices

is $v = 0.3$, and the impurities considered are (a)-(c): $\sigma(r) = e^{-r^2}$ and (d)-(f): $\sigma(r) = -e^{-r^2}$. Figs. 5.17(a) and (d) show the initial configurations of two vortices on either side of an impurity located at the origin. For $c > 0$, we see in Fig. 5.17(b) that the vortices and impurity all meet at the origin, forming a large lump of energy density. The same situation for $c < 0$ is seen in Fig. 5.17(e). Here the energy forms a ring surrounding the impurity. For both impurities, the overall result is that the vortices scatter at right angles, and we see in Figs. 5.17(c) and (e) that the vortices emerge and travel to infinity along the y-axis.

5.3 Conclusions

In this chapter we have numerically investigated the dynamics of vortices in the presence of magnetic impurities of the form $\sigma(r) = ce^{-dr^2}$. We began by introducing the model and the Bogomolny bound satisfied by vortices at critical coupling. We reproduced some of the results for vortices at critical coupling obtained in Ref. [86] by a different method. Our method also allows us to solve for vortices away from critical coupling, and we presented vacuum solutions for $\lambda = 0.5$ and $\lambda = 1.5$. We discussed the conjecture that for $c < 0$ a delta function impurity behaves like another vortex and illustrated that this occurs regardless of the coupling constant λ by comparing vacuum profile functions for impurities approaching a delta function to ordinary $N = 1$ vortex profile functions.

We determined how the attraction or repulsion between a vortex and an impurity depends on the coupling constant λ and the impurity parameters c and d by considering the difference in energy between a well-separated vortex and impurity and a coincident vortex and impurity. We found that there are three different regimes: (i) $c > 0$ where an impurity will attract a vortex for $\lambda < 1$ and repel it for $\lambda > 1$; (ii) $c < 0$ with the impurity repelling a vortex for $\lambda < 1$ and attracting it for $\lambda > 1$; and (iii) $c < 0$ with the impurity attracting a vortex for $\lambda < 1$ and repelling it for $\lambda > 1$. We calculated the critical line separating the two different types of behaviour for $c < 0$ and compared this to the line $c = -4d$ along which impurities approach a delta function. We found that for sufficiently large d these impurities should fall into category (iii) and thus do behave like vortices. We also investigated the attraction or repulsion between an impurity and a vortex by using the vortex asymptotics at large r, but found that this only agreed with the predictions of the energy calculation for case (iii). We were able to understand the disagreement between the two predictions by considering the

energy as a function of the separation s between the vortex and impurity. This revealed that the behaviour was also dependent on s, which explained the discrepancies.

The final section of the chapter was concerned with the scattering of vortices with magnetic impurities at critical coupling. Our aim was to provide a numerical study of the scattering processes, similar to those already conducted for vortices in the absence of impurities [76, 77, 78, 81]. We first considered the scattering of a single vortex with an impurity for different impact parameters. In a head-on collision, the vortex will travel through the impurity and continue on its original trajectory, though the details differ depending on the sign of c. The scattering angle increases with impact parameter until it attains a maximum value (at impact parameter $b \approx 1.5$ for the two impurities we considered), after which it begins decreasing to zero. When $c > 0$, the vortex trajectory bends towards the impurity and when $c < 0$ it bends away. The general shape of the scattering angle plot was found to be similar to a scattering angle plot given in Ref. [86] for vortices and impurities in hyperbolic space. We also considered the head-on scattering of a 2-vortex ring with an impurity and found that the ring breaks up into two single vortices as it passes through the impurity. For $c > 0$, the ring breaks up along the x-axis, and for $c < 0$ it breaks up along the y-axis.

Finally, we considered the scattering of two vortices in the presence of an impurity. In a head-on collision, we found that the vortices pass through the impurity and scatter at right angles, as they would in the absence of an impurity, see for example Refs. [76, 77]. The details of the scattering process are slightly different depending on the sign of c. As the impact parameter increases, the scattering angle decreases. Initially the repulsion between two vortices has the strongest effect on the vortex trajectories, even in the presence of an impurity with $c > 0$. However we found that there is a certain value of the impact parameter ($b \approx 2.54$ for the impurity we considered) past which the relationship between the vortex and the impurity controls the direction of the vortex trajectories. So for an impurity which attracts a vortex, the trajectories will bend towards the impurity, and for an impurity which repels a vortex, the trajectories will continue to bend away from the vortex. For large enough b, the vortex trajectories are no longer affected by each other, and the scattering angles are identical to those for a single vortex scattering with the impurity.

There remain many possibilities for further work on this subject. Thus far, we have only simulated vortex dynamics at critical coupling, but it would be interesting to investigate the cases when $\lambda < 1$ and $\lambda > 1$ also. When a 2-vortex ring scatters with an impurity, it

breaks up into two vortices in a different way depending on the sign of c. The scattering of higher charge multi-vortex rings with an impurity should be investigated to see whether a similar behaviour is observed for them. Finally the scattering of vortices with different impurities should be studied. In particular, it would be interesting to consider impurities which approach a delta function, as we have observed that these should behave like vortices.

Chapter 6

Conclusions

We conclude by summarising the results of each chapter and reflecting upon opportunities for further work. This thesis presented the results of four research projects concerning three different types of soliton. We began in Chapter 1 with a general introduction to topological solitons, and used the examples of ϕ^4 and sine-Gordon kinks to illustrate important concepts such as Bogomolny bounds, Derrick's theorem, and the topological structure of solitons.

In Chapter 2, we numerically investigated the collisions of kinks interpolating between true and false vacua in a model first introduced in Ref. [16]. Due to the imbalance in the vacuum energies, such kinks will move in the direction that extends the region of true vacuum when evolved from rest. If the true vacuum lies in between two kinks then they will move apart and separate to infinity, and if it lies outside of the kinks they will move towards each other. We carried out numerical simulations of kink scattering over a range of initial velocities $0 \leq v \leq 0.9$ and found a rich variety of scattering outcomes depending on the initial velocity and the vacuum structure of the configuration.

We observed alternating windows of initial velocity in which different scattering behaviours occurred. For kink-kink type collisions with false vacuum outside the kinks, when $v > 0.476$ the kinks would either capture one another to form a false domain wall or bounce off each other and separate to infinity. Similar windows have been known to appear in other kink models such as the ϕ^4 model [12, 13, 17] and the ϕ^6 model [20, 21], and have been related to an energy exchange between translational and vibrational modes [13, 20].

For kink-antikink type collisions with true vacuum outside of the kinks, we found alternating windows of initial velocity in which the kinks would either capture each other and annihilate in their first collision, or reflect off one another and travel apart before returning to

collide again. The latter behaviour could repeat a number of times before the kinks eventally annihilated. The annihilation process involved the formation of an oscillon that would ultimately decay to the true vacuum. Oscillons have been observed as a result of kink-antikink collisions in many models, for example in Refs. [18, 19, 24, 25].

We also found windows of alternating behaviour for kink-antikink type collisions with true vacuum in between the two kinks. Here the kinks would either annihilate by forming an oscillon that decays to the false vacuum, or bounce off each other and separate to infinity. We found a fractal structure in which smaller windows would appear as we zoomed in at a boundary between annihilation and bounce windows. Windows with a fractal structure similar to this have been observed in other kink models, for example see Refs. [26, 27, 28].

There are still many opportunities for further work on this project. One could consider the effect of varying the model parameters on the scattering behaviours observed. It would affect the locations of the critical velocity and alternating windows, and might even allow new scattering behaviours. Already we have found one new behaviour for a choice of parameters resulting in more sine-Gordon like kinks. We simulated kink-antikink collisions and found a behaviour where the shepherd kinks formed an oscillon but the sheep kinks did not annihilate for the duration of the simulation. We could also consider taking individual parameters to extreme limits, for example making one of the fields very massive. This would be similar to the vortex scattering with static impurities discussed in Chapter 5.

It would also be interesting to study collisions of multi-kink solutions. For configurations with an odd number of kinks, there would be an additional challenge in dealing with the imbalance of having true vacuum at one boundary and false vacuum at the other. Finally we should investigate whether the appearance of windows of different scattering behaviours in our model can be explained by an energy exchange between translational and vibrational modes as has been argued for other models in the literature. At present the only attempt we have made to explain the behaviours observed in our model was using the point particle approximation given in Appendix A, which was successful at replicating the trajectories for the kink-kink configurations, but did not capture all of the kink-antikink behaviours.

In Chapter 3, we developed a one-parameter family of baby Skyrme models that do not require a potential term to admit topological solitons. We explained how an application of Derrick's theorem shows that the baby Skyrme model requires a potential term to have soliton solutions but the Skyrme model does not. By raising the sigma and Skyrme terms in

our models to some fractional powers α and β, we were able to evade Derrick's theorem.

Motivated by recent work on topological energy bounds [63, 60], we began with a general form for our models involving four parameters and fixed three of them by requiring that the models satisfy $E \geq 4\pi|B|$. Similarly to the Skyrme models described in [61], at one end of our parameter range there is a model in which this bound can be saturated. Our choice of parameters also ensured that our models satisfy the same virial theorem, $E_2 = E_4$, as the Skyrme model. At $\alpha = 0.5$, there is a model that scales exactly like the Skyrme model.

We obtained soliton solutions in these models numerically using a finite difference method. Solitons in the $\alpha = 0.5$ model were found to be compactons. Both our numerical results for this model and linearisation arguments support this conclusion. Previous examples of compactons in baby Skyrme models [71, 51, 72] depended on the potential term used and typically occurred for particular parameter values in a one-parameter family of potential functions. There are no potential terms in our family of models but the choice of parameter is also important for the existence of compactons here.

For $\alpha > 0.5$, the solitons are less localised. Their energy decreases as α increases and higher-charge solutions become more tightly bound as $\alpha \to 0.5$. The energy minimisers are axially symmetric solutions for all $B \leq 3$. However, we did observe other higher-charge configurations with greater energy, in particular $B = 3$ chain configurations. Chain solutions for $\alpha \in [0.6, 0.7]$ most closely resemble those observed in the old baby Skyrme model [44], whilst other chains have a very different appearance. In particular, as α increases our chain configurations begin to pull apart and become three almost separate solitons. These are more reminiscent of the isospinning chain solutions of Ref. [35].

As further work, we could investigate solitons of higher charges and see whether axially symmetric solutions would always be the minimal energy configurations. Another avenue for future research could be to include a potential term. Whilst the unique aspect of our models is that they do not require a potential term, it would be interesting to see what effect, if any, that different potentials would have on the solitons of the model. Following Ref. [63] and balancing the different terms with the potential would give rise to multi-parameter families of models which still obey a linear energy bound. Finally, the numerical study of compactons is a difficult challenge, and it would be interesting to investigate the use of other numerical methods in the $\alpha = 0.5$ model to develop effective methods that could be applied to compactons in various models.

In Chapter 4 we numerically simulated the scattering of multi-vortex rings at critical coupling in the Ginzburg-Landau model, also known as the Abelian-Higgs model. We particularly studied head-on collisions of two 2-vortex rings and two 3-vortex rings. Two different scattering outcomes were found in each case, depending on the initial velocity given to the vortex rings.

In collisions of two 2-vortex rings, there is always one pair of vortices which will scatter at right angles and escape along the y-axis. The remaining pair of vortices will either form a bound state at the origin in which the vortices repeatedly scatter through each other at right angles, or escape to infinity along one of the axes after a number of collisions. The formation of a bound state is the most common outcome, however for initial velocity $v > 0.64$ there are alternating windows of the bound state and escape behaviours. For windows of the escape behaviour, the number of collisions before the vortices escape along an axis is conserved in each window. These windows of alternating scattering behaviour have not been observed in vortex scattering before, but are a common feature of kink-antikink interactions, for example in the ϕ^4 model [12, 13, 17] and the ϕ^6 model [20, 21]. They were also a feature of the kink scattering in the presence of false vacua discussed in Chapter 2 of this thesis. The conserved number of collisions in each window of the escape behaviour for our vortices is similar to the conserved "bounce" number in windows of the reflection behaviour for kink scattering.

The scattering outcomes for two 3-vortex rings are similar. In both cases, one pair of vortices will scatter at right angles and escape along the y-axis. At a later time, the remaining four vortices also scatter, and two of them escape along the y-axis at a slower speed than the original pair. The final two vortices can either form a bound state at the origin, similar to that observed for 2-vortex rings, or escape along the x-axis. For $v > 0.6$ the escape behaviour is a possible outcome, whilst for lower initial velocities a bound state is always formed.

In the future, we plan to compare the results of our numerical simulations to the predictions of the moduli space approximation. There is a conjecture that the vortex rings should remain rings, yet our simulations so far contradict this. It would also be interesting to study the appearance of windows of different scattering behaviour further, as this is something unexpected. We could investigate collisions of N-vortex rings for larger N to see if the scattering outcomes continue to follow the pattern set by the 2-vortex and 3-vortex ring simulations. Another further development of the project could be to consider vortices away from critical coupling, as we have only considered critically coupled vortex rings thus far.

Finally, in Chapter 5 we studied the scattering of vortices with magnetic impurities of the form $\sigma(r) = ce^{-dr^2}$. Previous work on this topic, such as Ref. [86], has concentrated on vortices at critical coupling, but our simulations included the Type I and Type II regimes as well. We first considered static solutions and showed that an impurity can either attract or repel a vortex depending on the coupling constant λ, the impurity parameters c and d, and the separation s between the vortex and impurity.

We carried out numerical simulations scattering a single vortex at critical coupling with an impurity for a range of different impact parameters and the two impurities $\sigma = \pm e^{-r^2}$. In a head-on collision, the vortex travels through the impurity and continues on its original trajectory. As the impact parameter increases, so does the scattering angle, up until a maximum value (located at $b \approx 1.5$ for the impurities we considered) after which it decreases again. For $c > 0$ the moving vortex is attracted to the impurity, whilst for $c < 0$ it is repelled by the impurity. The general shape of the scattering angle as a function of impact parameter is similar to that given in Ref. [86] for a single vortex scattering with an impurity in hyperbolic space, although since we work in flat space they cannot be directly compared.

We also considered the scattering of two charge 1 vortices in the presence of an impurity. For impact parameter $b = 0$, the vortices scatter at right angles, as they would do in the absence of an impurity, see for example Refs. [76, 77]. As the impact parameter increases, the scattering angle decreases. Once the vortices are sufficiently well-separated from one another, the sign of the impurity parameter c controls the vortex trajectories. If $c > 0$ then the trajectories will bend towards the impurity and if $c < 0$ then they will bend away from it. Finally we simulated head-on collision of a 2-vortex ring with an impurity and found that the ring will break up upon hitting the impurity. For $c > 0$, the ring splits up into two single vortices along the x-axis, whilst for $c < 0$, it splits up along the y-axis.

To further develop this project, we intend to simulate vortex dynamics in the Type I and Type II regimes, as here we have only presented results at critical coupling. We also plan to better understand the relationship between the impurity parameters and the change in attraction or repulsion of a vortex and an impurity for $c < 0$. It would be especially interesting to study the scattering of a vortex with one of the impurities that approaches a delta function, as in this case the impurity should behave like a second vortex. We could also study the scattering of multi-vortex rings with impurities for higher charges and investigate whether the dependence on the sign of c that we observed for the break up of 2-vortex rings

is also evident there.

In this thesis we have presented four different projects concerning solitons and their dynamics, and now we explore the connections between them. The only chapter not to feature any soliton dynamics was Chapter 3, but it did involve the concepts of topological energy bounds and Bogomolny solutions which were present in both vortex chapters. Perhaps the most surprising relation between any two projects was the appearance of windows of different scattering behaviour in both Chapter 2 and Chapter 4. Whilst this is not unexpected in a kink model, we would not have predicted the appearance of such windows in the vortex scattering project. A clear link between Chapters 4 and 5 is that both concern vortex dynamics. In Chapter 2 we explored how the locations of the true and false vacua would lead to either an attractive or repulsive initial configuration and how this in turn would affect the possible scattering outcomes for the kinks. Similarly, in Chapter 5, we considered the various situations in which an impurity could either attract or repel a vortex and the corresponding scattering behaviour.

Overall, topological solitons form a rich area of study with widespread and exciting applications in such diverse areas as nuclear physics, superconductivity, and the design of revolutionary new data storage technologies. In this thesis we have aimed to contribute to the understanding of topological solitons and their dynamics, and in turn hope that this will lead to advances for the wider scientific community.

Appendix A

Kinks: a point particle approximation

In this appendix, we discuss a toy model which mimics some of the features of the scattering of our kinks. Let m be the reduced mass of A and B kinks, and let $r(t)$ be their relative position at time t. We try to model the sheep scattering using a point particle approximation with equation of motion

$$m\ddot{r} = 2mg\left(\tanh^2(r) - f\right) + \frac{2a}{r}e^{-br} - d\dot{r}e^{-cr}, \tag{A.1}$$

where $m,\ g,\ a,\ b,\ c,\ d,\ f$ are constants. Here, the first term in (A.1) allows for the existence of a metastable bound state, while the second term acts as a contact interaction term preventing A and B kinks from passing through each other. To allow for radiation, we add a friction term of the form $d\dot{r}e^{-cr}$. We solve (A.1) subject to the conditions

$$r(0) = 2, \quad \dot{r}(0) = v_0, \tag{A.2}$$

so that the points start at positions ± 1, and v_0 is used to specify the initial velocity. The signs of a and g are used to determine which type of configuration we study.

By choosing $a > 0$ and $g > 0$, we can replicate the three scattering outcomes of the AB configuration. For example, set the parameters to be

$$m = 1, \quad g = 1, \quad a = 0.1, \quad b = 5, \quad c = 3, \quad d = 1, \quad f = \tfrac{1}{2}. \tag{A.3}$$

The corresponding potential $V(r)$ is displayed in Fig. A.1(a). It has one minimum, which is located near the origin. For different values of the initial velocity v_0, we observe different scattering outcomes. In Fig A.1(b), we show the solutions $x_1(t)$ and $x_2(t)$ for $v_0 = 0$, where these are related to the solution of (A.1) by $r(t) = x_1(t) - x_2(t)$. This mimics the behaviour

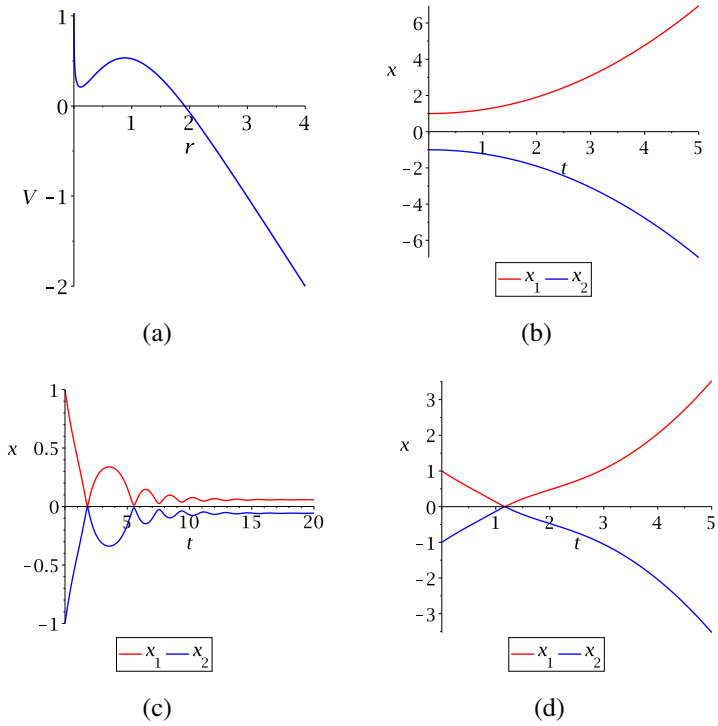

Figure A.1: (a) The potential $V(r)$ used to mimic AB scattering. (b) Solutions $x_1(t)$ in red and $x_2(t)$ in blue for initial velocity $v_0 = 0$. (c) Solutions $x_1(t)$ and $x_2(t)$ for $v_0 = -1.5$. (d) Solutions $x_1(t)$ and $x_2(t)$ for $v_0 = -2$.

of the AB kinks for low initial velocities, where they cannot overcome their repulsion and separate to infinity. Fig A.1(c) displays the solutions for initial velocity $v_0 = -1.5$. Here we see the formation of a metastable bound state, akin to the formation of a false domain wall in the AB "sticking" behaviour. Finally, in Fig. A.1(d), we take initial velocity $v_0 = -2$ and observe the points reflect off each other and separate to infinity.

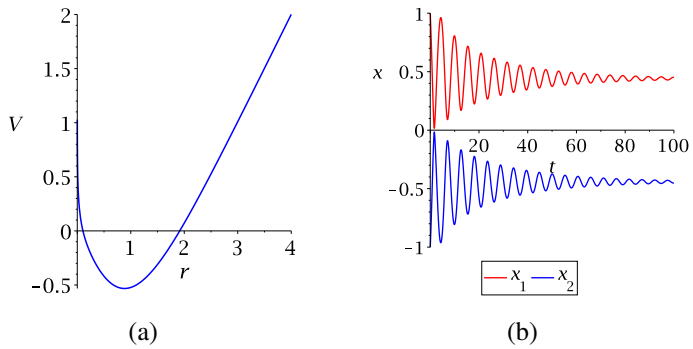

Figure A.2: (a) The potential $V(r)$ used to mimic BA scattering. (b) Solutions $x_1(t)$ in red and $x_2(t)$ in blue for $v_0 = -1$.

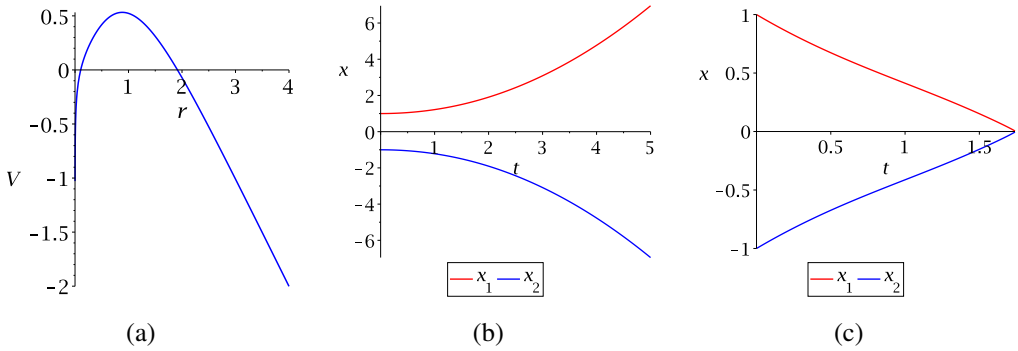

Figure A.3: (a) The potential $V(r)$ used to mimic $A\overline{B}$ scattering. (b) Solutions $x_1(t)$ in red and $x_2(t)$ in blue for $v_0 = 0$. (c) Solutions $x_1(t)$ and $x_2(t)$ for $v_0 = -1.5$.

To model the BA configuration, we take $a > 0$ and $g < 0$. For example,

$$m = 1, \quad g = -1, \quad a = 0.1, \quad b = 5, \quad c = 3, \quad d = 1, \quad f = \tfrac{1}{2}. \tag{A.4}$$

We display the corresponding potential $V(r)$ in Fig. A.2(a). It has one minimum, located near $r = 1$. When solving the equation of motion (A.1), the result is always the formation of a bound state. This is also true of the BA configurations, which will ultimately form a true domain wall regardless of the initial velocity. Fig. A.2(b) shows the solutions $x_1(t)$ and $x_2(t)$ obtained from the initial velocity $v_0 = -1$, which form a bound state over time.

To try and model $A\bar{B}$ scattering, we choose $a < 0$ and $g > 0$. For example, we fix the parameters to be

$$m = 1, \quad g = 1, \quad a = -0.1, \quad b = 5, \quad c = 3, \quad d = 1, \quad f = \tfrac{1}{2}. \tag{A.5}$$

The corresponding potential $V(r)$ is displayed in Fig. A.3(a). It has one maximum, located near $r = 1$. There are two different types of behaviour. Firstly, the points can repel and separate to infinity, as shown in Fig. A.3(b) for initial velocity $v_0 = 0$. They can also hit the singularity at $r = 0$, at which point we cannot evaluate the solution any further. We take this to correspond to the annihilation behaviour of the $A\overline{B}$ kinks, and an example of this type of solution for initial velocity $v_0 = -1.5$ is given in Fig. A.3(c). Note that there is one behaviour type that we cannot recapture with this model. The $A\overline{B}$ kinks can reflect off each other and then separate to infinity, but we do not see this in the point particle model.

Finally, when we take $a < 0$ and $g < 0$, we mimic the $B\overline{A}$ scattering. We choose the parameters

$$m = 1, \quad g = -1, \quad a = -4, \quad b = 5, \quad c = 3, \quad d = 1, \quad f = \tfrac{1}{2}. \tag{A.6}$$

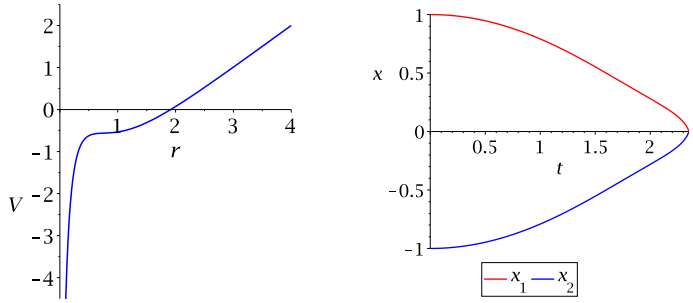

(a) (b)

Figure A.4: (a) The potential $V(r)$ used to mimic $B\overline{A}$ scattering. (b) Solutions $x_1(t)$ in red and $x_2(t)$ in blue for $v_0 = 0$.

Fig. A.4(a) displays the corresponding potential $V(r)$. Note that if the parameters are chosen differently, an extra minimum may appear in the potential. We deliberately avoid this as it would allow for bound state solutions, and this is not an outcome for the $B\overline{A}$ configuration. In the point particle approximation with these parameter values, the only outcome is that the solutions hit the singularity at $r = 0$, beyond which we cannot evaluate them any further. As an example, Fig. A.4(b) presents the solutions for initial velocity $v_0 = 0$. The $B\overline{A}$ kinks do all eventually annihilate, however for certain choices of initial velocity, they can reflect off each other one or two times before annihilating. We are unable to see this behaviour in the toy model.

To summarise, for the AB and BA configurations, we are able to successfully replicate all of the kink trajectories in this toy model. However, for the $A\overline{B}$ and $B\overline{A}$ configurations, we are unable to see the reflection behaviour in the point particle approximation and can only replicate the repulsion and annihilation behaviours. In a point particle model, we are also unable to capture phenomena such as the oscillon, and the bounces in the shepherd field. Possible adjustments to the toy model could include implementing a different friction term. For example, using a friction term such as $-\frac{d\dot{r}e^{-cr}}{r^2}$, we can force solutions in the $A\overline{B}$ and $B\overline{A}$ cases to grind to a halt before hitting the singularity.

Appendix B

Baby Skyrmion linearisation

B.1 Linearising as $r \to \infty$

In this appendix, we linearise the equation of motion for an axially symmetric charge B soliton in the baby Skyrme model (3.16) for large r. As discussed in Secs. 3.2.1 and 3.2.2, we set $\beta = 1 - \frac{\alpha}{2}$, and the constants c_1 and c_2 are fixed in (3.35).

The equation of motion for the profile function $f(r)$ is given by

$$\begin{aligned}
&f''\left(\frac{4\alpha(\alpha-1)c_1 f'^2}{f'^2+\frac{B^2}{r^2}\sin^2 f}+\frac{2\beta(2\beta-1)c_2\left(2f'^2\frac{B^2}{r^2}\sin^2 f\right)^{\beta}\left(f'^2+\frac{B^2}{r^2}\sin^2 f\right)^{1-\alpha}}{f'^2}+2\alpha c_1\right)\\
&+f'\left(\frac{2\alpha c_1}{r}+\frac{2\alpha(\alpha-1)c_1\left(-2\frac{B^2}{r^3}\sin^2 f+\frac{B^2}{r^2}f'\sin 2f\right)}{f'^2+\frac{B^2}{r^2}\sin^2 f}\right)\\
&+\frac{c_2\beta(2\beta-1)\left(2f'^2\frac{B^2}{r^2}\sin^2 f\right)^{\beta}\left(f'^2+\frac{B^2}{r^2}\sin^2 f\right)^{1-\alpha}\left(-\frac{2}{r}\sin^2 f+f'\sin 2f\right)}{f'\sin^2 f}\\
&-\alpha c_1\frac{B^2}{r^2}\sin 2f=0.
\end{aligned} \tag{B.1}$$

To linearise the symmetric equation of motion (B.1) as $r \to \infty$, we substitute $f(r) = r^{\lambda}$ into (B.1) and consider only the leading-order terms. For $\alpha \leq 1$, this leads to the equation

$$\frac{(2\alpha-1)\lambda^4-2(\alpha-1)\lambda^3+2B^2(\alpha-1)\lambda^2-2B^2(\alpha-1)\lambda-B^4}{\lambda^2+B^2}=0, \tag{B.2}$$

which simplifies to the quadratic

$$(2\alpha-1)\lambda^2-2(\alpha-1)\lambda-B^2=0. \tag{B.3}$$

For $\alpha \neq \frac{1}{2}$ this can be solved for λ, to find

$$\lambda_{\pm}=\frac{\alpha-1\pm\sqrt{\alpha^2+2(B^2-1)\alpha-B^2+1}}{2\alpha-1}. \tag{B.4}$$

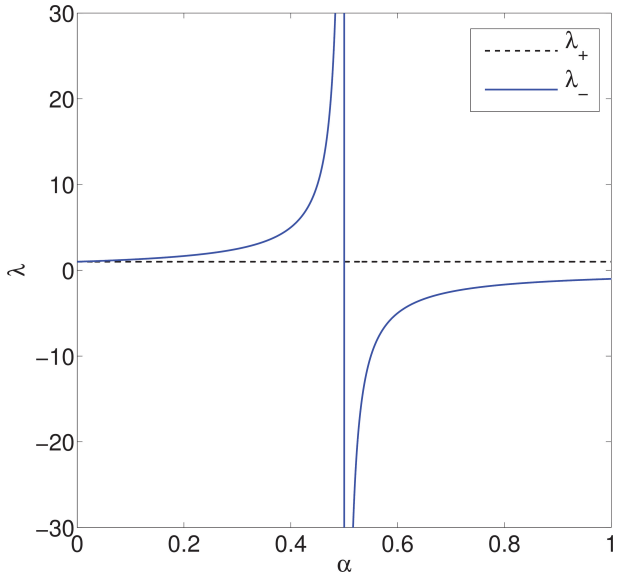

Figure B.1: Real solutions λ_+, λ_- of Eq. (B.2) as functions of α for $0 < \alpha < 1$ and $B = 1$.

For parameter value $\alpha = 1$, most of the terms cancel and the solutions are

$$\lambda = \pm B. \tag{B.5}$$

At the other extreme, where $\alpha = 0.5$, the quadratic term in (B.3) cancels. The solution λ_- becomes singular and $\lambda_+ = B^2$. In Fig. B.1 we plot the two solutions λ_+, λ_- of Eq. (B.3) as a function of the model parameter α for $0 < \alpha < 1$ and topological charge $B = 1$. The root λ_+ is always positive and therefore we discard it. The root λ_- has an asymptote at $\alpha = 0.5$ where Eq. (B.2) is singular. For $0 < \alpha < 0.5$, the values of λ_- are positive and therefore solutions for this range of α are either compact or do not have finite energy. The interesting parameter range is $0.5 < \alpha \leq 1$ in which $\lambda_- \leq -1$ and solutions have finite energy.

For $\alpha > 1$, the leading-order terms in (B.1) after substituting $f(r) = r^\lambda$ are different, so that a different linearised equation is found in this parameter range. Here the equation becomes

$$\frac{2(2-\alpha)(1-\alpha)c_2}{\lambda}(\lambda - 1)\left(2\lambda^2 B^2\right)^{1-\alpha/2}\left(\lambda^2 + B^2\right)^{1-\alpha} = 0 \tag{B.6}$$

The only solutions are $\lambda = 1$ and $\lambda = \pm iB$. Thus for $\alpha > 1$, solutions to the equation of motion would either have infinite energy or be compact.

B.2 Linearising near $r = 0$

We also linearise the equation near $r = 0$ to gain a greater understanding of the behaviour of solutions in relation to their topological charge. Set

$$f(r) = \pi - ar^{\gamma}, \tag{B.7}$$

in (B.1), where a is constant, and assume that $\gamma \geq 1$. For small r^{γ}, we can use the small angle approximation to replace trigonometric terms. By our assumption on γ and the constraint $0.5 \leq \alpha \leq 1$, we find the leading-order equation

$$2\alpha a c_1 \left(2\gamma^3(\alpha - 1)\frac{1-\gamma}{B^2+\gamma^2} + \gamma(1-\gamma) - 2\gamma(\alpha-1)B^2\frac{\gamma-1}{B^2+\gamma^2} + B^2 - \gamma \right) = 0, \tag{B.8}$$

which simplifies to the quadratic

$$B^2 + 2(\alpha - 1)\gamma - (2\alpha - 1)\gamma^2 = 0. \tag{B.9}$$

For $\alpha > 0.5$, we can solve this to find the positive root

$$\gamma = \frac{-1 + \alpha + \sqrt{\alpha^2 + 2(B^2 - 1)\alpha + 1 - B^2}}{2\alpha - 1}. \tag{B.10}$$

Note that once again the $\alpha = 0.5$ case must be considered separately. Here we obtain the leading-order equation

$$B^2 - \gamma = 0, \tag{B.11}$$

so we find $\gamma = B^2$ when $\alpha = 0.5$. This is also the limit of (B.10) as $\alpha \to 0.5$.

At the other end of our allowed range of α values, where $\alpha = 1$, we observe that the expression (B.10) simplifies to

$$\gamma = |B|. \tag{B.12}$$

Notice that for $B = 1$ and any choice of $\alpha \geq 0.5$, we find $\gamma = 1$. So for all of our models, the charge one profile function has a linear behaviour near the origin. For $B > 1$ we confirm that $\gamma(\alpha)$ as given by (B.10) does not have any turning points in the interval $0.5 < \alpha < 1$, with $\gamma(0.5) = B^2$ and $\gamma(1) = |B|$. Hence $\gamma \geq 1$ for any choice of $B \geq 1$. This justifies our earlier assumption on γ.

Bibliography

[1] J. Ashcroft, M. Eto, M. Haberichter, M. Nitta and M. B. Paranjape, *Head butting sheep: Kink collisions in the presence of false vacua*, J. Phys. A: Math. Theor. **49**: 365203 (**2016**).

[2] J. Ashcroft, M. Haberichter and S. Krusch, *Baby Skyrme models without a potential term*, Phys. Rev. **D91**: 105032 (**2015**).

[3] N. S. Manton and P. M. Sutcliffe, *Topological solitons*, Cambridge University Press (**2004**).

[4] A. A. Abrikosov, *On the Magnetic properties of superconductors of the second group*, Sov. Phys. JETP **5**: 1174 (**1957**).

[5] B. M. A. G. Piette, B. J. Schroers and W. J. Zakrzewski, *Multi - solitons in a two-dimensional Skyrme model*, Z. Phys. **C65**: 165 (**1995**).

[6] B. M. A. G. Piette, B. J. Schroers and W. J. Zakrzewski, *Dynamics of baby Skyrmions*, Nucl. Phys. **B439**: 205 (**1995**).

[7] T. H. R. Skyrme, *A nonlinear field theory*, Proc. Roy. Soc. Lond. **A260**: 127 (**1961**).

[8] J. S. Russell, *Report on Waves*, Report of the fourteenth meeting of the British Association for the Advancement of Science page 311 (**1844**).

[9] A. T. Filippov, *The Great Solitary Wave of John Scott Russell*, Birkhäuser Boston, Boston (**2010**).

[10] E. B. Bogomolny, *Stability of Classical Solutions*, Sov. J. Nucl. Phys. **24**: 449 (**1976**).

[11] G. H. Derrick, *Comments on nonlinear wave equations as models for elementary particles*, J. Math. Phys. **5**: 1252 (**1964**).

[12] M. Moshir, *Soliton - anti-soliton scattering and capture in $\lambda\phi^4$ Theory*, Nucl. Phys. **B185**: 318 (**1981**).

[13] D. K. Campbell, J. F. Schonfeld and C. A. Wingate, *Resonance structure in kink - antikink interactions in ϕ^4 theory*, Physica **9D**: 1 (**1983**).

[14] T. H. R. Skyrme, *Particle states of a quantized meson field*, Proc. Roy. Soc. Lond. **A262**: 237 (**1961**).

[15] J. K. Perring and T. H. R. Skyrme, *A Model unified field equation*, Nucl. Phys. **31**: 550 (**1962**).

[16] M. Haberichter, R. MacKenzie, M. B. Paranjape and Y. Ung, *Tunneling decay of false domain walls: the silence of the lambs*, J. Math. Phys. **57**: 042303 (**2016**).

[17] T. I. Belova and A. E. Kudryavtsev, *Quasiperiodical orbits in the scalar classical $\lambda\ \phi^4$ field theory*, Physica **D32**: 18 (**1988**).

[18] P. Anninos, S. Oliveira and R. A. Matzner, *Fractal structure in the scalar $\lambda(\phi^2 - 1)^2$ theory*, Phys. Rev. **D44**: 1147 (**1991**).

[19] A. Halavanau, T. Romanczukiewicz and Ya. Shnir, *Resonance structures in coupled two-component ϕ^4 model*, Phys. Rev. **D86**: 085027 (**2012**).

[20] P. Dorey, K. Mersh, T. Romanczukiewicz and Ya. Shnir, *Kink-antikink collisions in the ϕ^6 model*, Phys. Rev. Lett. **107**: 091602 (**2011**).

[21] H. Weigel, *Kink-antikink scattering in φ^4 and ϕ^6 models*, J. Phys. Conf. Ser. **482**: 012045 (**2014**).

[22] S. P. Yukon and B. A. Malomed, *Fluxons in a triangular set of coupled long Josephson junctions*, J. Math. Phys. **56**: 091509 (**2015**).

[23] E. Dupuis, Y. Gobeil, R. MacKenzie, L. Marleau, M. B. Paranjape and Y. Ung, *Tunneling decay of false kinks*, Phys. Rev. **D92**: 025031 (**2015**).

[24] J. Braden, J. R. Bond and L. Mersini-Houghton, *Cosmic bubble and domain wall instabilities I: parametric amplification of linear fluctuations*, JCAP **1503**: 007 (**2015**).

[25] V. A. Gani, V. Lensky and M. A. Lizunova, *Kink excitation spectra in the (1+1)-dimensional φ^8 model*, JHEP **08**: 147 (**2015**).

[26] M. Peyrard and D. K. Campbell, *Kink antikink interactions in a modified sine-Gordon model*, Physica **9D**: 33 (**1983**).

[27] R. H. Goodman and R. Haberman, *Kink-antikink collisions in the ϕ^4 equation: The n-bounce resonance and the separatrix Map*, SIAM J. Appl. Dyn. Sys. **4**: 1195 (**2005**).

[28] R. H. Goodman and R. Haberman, *Chaotic scattering and the n-bounce resonance in solitary-wave interactions*, Phys. Rev. Lett. **98**: 104103 (**2007**).

[29] S. L. Sondhi, A. Karlhede, S. A. Kivelson and E. H. Rezayi, *Skyrmions and the crossover from the integer to fractional quantum Hall effect at small Zeeman energies*, Phys. Rev. **B47**: 16419 (**1993**).

[30] N. R. Walet and T. Weidig, *Full 2-D numerical study of the quantum Hall Skyrme crystal* (**2001**).

[31] X. Z. Yu, Y. Onose, N. Kanazawa, J. H. Park, J. H. Han, Y. Matsui, N. Nagaosa and Y. Tokura, *Real-space observation of a two-dimensional skyrmion crystal*, Nature **465**: 901 (**2010**).

[32] M. Peyrard, B. Piette and W. J. Zakrzewski, *Soliton scattering in the Skyrme model in (2+1)-dimensions. 1. Soliton-soliton case*, Nonlinearity **5**: 563 (**1992**).

[33] T. Gisiger and M. B. Paranjape, *Recent mathematical developments in the Skyrme model*, Phys. Rept. **306**: 109 (**1998**).

[34] D. Foster and S. Krusch, *Scattering of Skyrmions*, Nucl. Phys. **B897**: 697 (**2015**).

[35] R. A. Battye and M. Haberichter, *Isospinning baby Skyrmion solutions*, Phys. Rev. **D88**: 125016 (**2013**).

[36] A. Halavanau and Y. Shnir, *Isorotating baby Skyrmions*, Phys. Rev. **D88(8)**: 085028 (**2013**).

[37] R. A. Battye, M. Haberichter and S. Krusch, *Classically isospinning Skyrmion solutions*, Phys. Rev. **D90**: 125035 (**2014**).

[38] T. Ioannidou and O. Lechtenfeld, *Noncommutative baby Skyrmions*, Phys. Lett. **B678**: 508 (**2009**).

[39] A. Domrin, O. Lechtenfeld, R. Linares and M. Maceda, *Exact BPS bound for noncommutative baby Skyrmions*, Phys. Lett. **B727**: 303 (**2013**).

[40] P. Eslami, W. J. Zakrzewski and M. Sarbishaei, *Baby Skyrme models for a class of potentials*, Nonlinearity **13**: 1867 (**2000**).

[41] T. Weidig, *The baby Skyrme models and their multiskyrmions*, Nonlinearity **12**: 1489 (**1999**).

[42] J. Jäykkä and J. M. Speight, *Easy plane baby Skyrmions*, Phys. Rev. **D82**: 125030 (**2010**).

[43] I. Hen and M. Karliner, *Rotational symmetry breaking in baby Skyrme models*, Nonlinearity **21**: 399 (**2008**).

[44] D. Foster, *Baby Skyrmion chains*, Nonlinearity **23**: 465 (**2010**).

[45] R. A. Leese, M. Peyrard and W. J. Zakrzewski, *Soliton scatterings in some relativistic models in (2+1)-dimensions*, Nonlinearity **3**: 773 (**1990**).

[46] P. M. Sutcliffe, *The interaction of Skyrme-like lumps in (2+1) dimensions*, Nonlinearity **4**: 1109 (**1991**).

[47] R. S. Ward, *Planar Skyrmions at high and low density*, Nonlinearity **17**: 1033 (**2004**).

[48] J. Jäykkä, J. M. Speight and P. M. Sutcliffe, *Broken baby Skyrmions*, Proc. Roy. Soc. Lond. **A468**: 1085 (**2012**).

[49] P. Jennings and T. Winyard, *Broken planar Skyrmions - statics and dynamics*, JHEP **01**: 122 (**2014**).

[50] T. Gisiger and M. B. Paranjape, *Solitons in a baby Skyrme model with invariance under volume / area preserving diffeomorphisms*, Phys. Rev. **D55**: 7731 (**1997**).

[51] C. Adam, T. Romanczukiewicz, J. Sanchez-Guillen and A. Wereszczynski, *Investigation of restricted baby Skyrme models*, Phys. Rev. **D81**: 085007 (**2010**).

[52] C. Adam, C. Naya, J. Sanchez-Guillen and A. Wereszczynski, *The vector BPS baby Skyrme model*, Phys. Rev. **D86**: 045015 (**2012**).

[53] S. Bolognesi and W. Zakrzewski, *Baby Skyrme model, near-BPS approximations and supersymmetric extensions*, Phys. Rev. **D91**: 045034 (**2015**).

[54] C. Adam, J. Sanchez-Guillen and A. Wereszczynski, *A Skyrme-type proposal for baryonic matter*, Phys. Lett. **B691**: 105 (**2010**).

[55] C. Adam, C. Naya, J. Sanchez-Guillen, J. M. Speight, R. Vazquez et al., *A unified approach to nuclei: The BPS Skyrme model* (**2014**).

[56] C. Adam, C. Naya, J. Sanchez-Guillen and A. Wereszczynski, *The vector BPS Skyrme model*, Phys. Rev. **D86**: 085001 (**2012**).

[57] P. M. Sutcliffe, *Multi-Skyrmions with vector mesons*, Phys. Rev. **D79**: 085014 (**2009**).

[58] D. Foster and P. M. Sutcliffe, *Baby Skyrmions stabilized by vector mesons*, Phys. Rev. **D79**: 125026 (**2009**).

[59] N. S. Manton and P. J. Ruback, *Skyrmions in flat space and curved space*, Phys. Lett. **B181**: 137 (**1986**).

[60] D. Harland, *Topological energy bounds for the Skyrme and Faddeev models with massive pions*, Phys. Lett. **B728**: 518 (**2014**).

[61] M. Gillard, D. Harland and J. M. Speight, *Skyrmions with low binding energies*, Nucl. Phys. **B895**: 272 (**2015**).

[62] P. Salmi and P. M. Sutcliffe, *Aloof baby Skyrmions*, J. Phys. **A48**: 035401 (**2015**).

[63] C. Adam and A. Wereszczynski, *Topological energy bounds in generalized Skyrme models*, Phys. Rev. **D89**: 065010 (**2014**).

[64] D. A. Nicole, *Solitons with nonvanishing Hopf index*, J. Phys. **G4**: 1363 (**1978**).

[65] H. Aratyn, L. A. Ferreira and A. H. Zimerman, *Toroidal solitons in (3+1)-dimensional integrable theories*, Phys. Lett. **B456**: 162 (**1999**).

[66] H. Aratyn, L. A. Ferreira and A. H. Zimerman, *Exact static soliton solutions of (3+1)-dimensional integrable theory with nonzero Hopf numbers*, Phys. Rev. Lett. **83**: 1723 (**1999**).

[67] M. Gillard and P. M. Sutcliffe, *Hopf solitons in the Nicole model*, J. Math. Phys. **51**: 122305 (**2010**).

[68] M. Gillard, *Hopf solitons in the AFZ model*, Nonlinearity **24**: 2729 (**2011**).

[69] N. S. Manton, *Geometry of Skyrmions*, Commun. Math. Phys. **111**: 469 (**1987**).

[70] D. Foster, *Massive Hopfions*, Phys. Rev. **D83**: 085026 (**2011**).

[71] C. Adam, P. Klimas, J. Sanchez-Guillen and A. Wereszczynski, *Compact baby Skyrmions*, Phys. Rev. **D80**: 105013 (**2009**).

[72] J. M. Speight, *Compactons and semi-compactons in the extreme baby Skyrme model*, J. Phys. **A43**: 405201 (**2010**).

[73] W. H. Press, S. A. Teukolsky, W. T. Vetterling and B. P. Flannery, *Numerical Recipes 3rd Edition: The Art of Scientific Computing*, Cambridge University Press (**2007**).

[74] V. L. Ginzburg and L. D. Landau, *On the theory of superconductivity*, Zh. Eksp. Teor. Fiz. **20**: 1064 (**1950**).

[75] L. Jacobs and C. Rebbi, *Interaction Energy of Superconducting Vortices*, Phys. Rev. **B19**: 4486 (**1979**).

[76] E. P. S. Shellard and P. J. Ruback, *Vortex scattering in two-dimensions*, Phys. Lett. **B209**: 262 (**1988**).

[77] C. Rebbi, R. Strilka and E. Myers, *Vortex scattering in the Abelian Higgs model*, Nucl. Phys. Proc. Suppl. **26**: 240 (**1992**).

[78] E. Myers, C. Rebbi and R. Strilka, *A Study of the interaction and scattering of vortices in the Abelian Higgs (or Ginzburg-Landau) model*, Phys. Rev. **D45**: 1355 (**1992**).

[79] E. P. S. Shellard, *The numerical study of topological defects*, in *Approaches to numerical relativity: International workshop: Papers*, pages 308–334, Cambridge University Press (**1992**).

[80] D. Stuart, *Dynamics of Abelian Higgs vortices in the near Bogomolny regime*, Commun. Math. Phys. **159**: 51 (**1994**).

[81] M. J. Thatcher and M. J. Morgan, *Vortex scattering in the Abelian Higgs model*, Class. Quant. Grav. **14**: 3161 (**1997**).

[82] Private communication with S. Krusch (**2017**).

[83] D. Tong and K. Wong, *Vortices and Impurities*, JHEP **01**: 090 (**2014**).

[84] X. Han and Y. Yang, *Topologically Stratified Energy Minimizers in a Product Abelian Field Theory*, Nucl. Phys. **B898**: 605 (**2015**).

[85] X. Han and Y. Yang, *Magnetic Impurity Inspired Abelian Higgs Vortices*, JHEP **02**: 046 (**2016**).

[86] A. Cockburn, S. Krusch and A. A. Muhamed, *Dynamics of vortices with magnetic impurities*, J. Math. Phys. **58**: 063509 (**2017**).

[87] J. M. Speight, *Static intervortex forces*, Phys. Rev. **D55**: 3830 (**1997**).

[88] H. J. de Vega and F. A. Schaposnik, *A classical vortex solution of the Abelian Higgs model*, Phys. Rev. **D14**: 1100 (**1976**).